UNIVERSIDADE DE LISBOA
FACULDADE DE CIÊNCIAS
DEPARTAMENTO DE ENGENHARIA GEOGRÁFICA, GEOFÍSICA E ENERGIA

Energy yield of CPV modules with different cell technologies

Sara Regina Teixeira Freitas

Dissertação de Mestrado Integrado em Engenharia da Energia e do Ambiente

Orientadores:

Miguel Centeno Brito (University of Lisbon)

José Mário da Costa Pó (University of Lisbon)

2013

UNIVERSIDADE DE LISBOA
FACULDADE DE CIÊNCIAS
DEPARTAMENTO DE ENGENHARIA GEOGRÁFICA, GEOFÍSICA E ENERGIA

Energy yield of CPV modules with different cell technologies

Sara Regina Teixeira Freitas

Mestrado Integrado em Engenharia da Energia e do Ambiente

2013

Abstract

The Circadian Solar research tracker at the Solar Campus at the Faculty of Sciences of the University of Lisbon was used for a case study of comparative assessment of HCPV modules performance. The research platform includes a complete set of instruments for weather and irradiation characterization and a set of fully instrumented identical CPV prototype modules, in an early stage of development, with triple-junction solar cells from different manufacturers. Spectral irradiance data were compared with simulated spectra produced by the SMARTS model using local atmospheric data and AOD collected from nearby observation stations. Once validated, the simulated spectra were used to model I_{sc} of the module prototypes. Actual power and energy yield during a 12 month period were analysed and showed that module A1, optimized for the reference AM1.5d spectrum yielded the best results. However, an identical module with solar cells provided by the same manufacturer generated less 7% energy in the same period highlighting an order of variability among components/assemblies that is expected for early stage prototype modules. Modules B1 and B2 are optimized for winter spectral conditions at the test site, produced less 4% energy during the same period. Module C has underperformed due to a malfunction that became apparent after October 2012.
Power rating according to the ASTM statistical regression method was also determined. Results showed that the effects of wind speed and ambient temperature introduce noise in the analysis and should be disregarded. This may be understood by noticing that the solar cells are encased and therefore less sensitive to wind speed and ambient temperature. Of course, the effect of the ambient temperature is already included indirectly via DNI, with which is strongly correlated to. Average deviations below 10% were determined suggesting that a second-order DNI only regression is the appropriate method for CPV systems power rating.

Keywords: CPV performance, triple-junction, spectral irradiance, SMARTS, energy yield.

Resumo

A plataforma de pesquisa pertencente à empresa Circadian Solar, instalada no Campus Solar da Faculdade de Ciências da Universidade de Lisboa, foi alvo de um estudo comparativo incidente no desempenho de módulos HCPV. A plataforma de pesquisa inclui um conjunto de instrumentos para caracterização a nível do tempo e da irradiância e um conjunto de protótipos de módulos CPV idênticos, numa fase inicial de desenvolvimento, contendo células solares de tripla-junção de diferentes fabricantes. A irradiância espectral monitorizada foi comparada com simulações realizadas a partir do modelo SMARTS usando dados atmosféricos locais e AOD medido em estações de observação próximas. Uma vez validada, a irradiância espectral simulada foi usada para modelar a corrente de curto-circuito dos protótipos. A potência e energia geradas durante um período de doze meses foram analisadas e mostram que o módulo A1, optimizado para o espectro de referência AM1.5d, alcançou os melhores resultados. No entanto, o módulo idêntico contendo células solares provenientes do mesmo fabricante gerou menos 7% de energia durante o mesmo período, destacando uma ordem de variabilidade ente componentes/montagem de acordo com a fase inicial em que os módulos se encontram. Os módulos B1 e B2 estão optimizados para as condições espectrais de inverno no local, tendo obtido uma produção energética inferior em 4% durante o mesmo período. O módulo C revelou um desempenho inferior desvio a falhas que se tornaram aparentes desde o mês de Outubro de 2012.
A avaliação de desempenho de acordo com a regressão estatística da ASTM foi igualmente determinada. Os resultados mostram que efeitos da velocidade do vento e da temperatura ambiente introduzem ruido na análise e devem ser desvalorizados. Este facto é explicado tendo em conta que as células solares estão encapsuladas e, deste modo, menos sensíveis a esses dois parâmetros. Por outro lado, o efeito da temperatura ambiente já se encontra indirectamente incluído a partir de DNI, com o qual está altamente correlacionada. Desvios médios abaixo de 10% foram determinados, sugerindo que uma regressão de segunda ordem de DNI é o método apropriado para avaliar o desempenho de módulos CPV.

Palavras-chave: Desempenho de CPV, junção-tripla, irradiância espectral, SMARTS, produção energética.

Index

List of Tables

List of Figures

Acknowledgements

On this page, written in last place, but that is still one of the most important, I take the opportunity to show my gratitude to all those whose support was essential to the accomplishment of this work.

Firstly, I have the obligation to get to the roots, so important to me. My heartfelt thanks to my parents, without whom I would not be who I am and where I am, and to my little brother, for asking me what a photon is.

Next, I express my enormous gratitude to my supervisor Professor Miguel Centeno Brito, who, besides having been my teacher in various disciplines over the past five years, became, since the first class I attended, an academic reference to me. Thank you for the crucial interventions at times when I felt more discouraged, and for believing that I am capable of going further.

Another great deal of gratitude belongs to my second supervisor José Mário Pó, without whom I could have never completed this work. My thanks for your time, patience and good mood during "fieldwork".

Martin Palmer and Jonathan Parsons of Circadian Solar, thank you very much for your support over more than 800 miles away.

I must also thank my master's program coordinator, Professor Jorge Maia Alves, who, despite not having been involved in this work, is the "responsible" for my interest in photovoltaics. My gratitude for the faith you have placed in your students.

As other passions go hand in hand with work, I leave here my gratitude to three very special groups, Ares Novos and Stravaganzza, whose kindness and dedication is unmatched, and to Monolith Moon, where everything progressively merges together. My thanks to everyone individually.

To Claudia Oliveira, with whom I went through a panoply of situations along the course, Rita Almeida and Isaac Carrêlo, my thanks for your partnership and friendship.

To Daniela Fonte and Isac Graça, for making these great friendships endure and enrich my life, my thanks to both.

Finally, my thanks to Carlos, the heart that complements everything. Hopefully now you can explain the photovoltaic effect in life ☺.

Abbreviation

η_{op}	Module optics' efficiency (%)
λ	Wavelength (nm)
ϕ_{inc}	Incident photon flux (photon/m^2/s)
AERONET	AErosol RObotic NETwork
A_f	Area of light focused on the cell (m^2)
A_{indoor}	Cell's area (m^2), test conditions in datasheet
AM	Air mass
AOD	Aerosol optical depth
APE	Average Photon Energy (eV)
ASTM	American Society for Testing Materials
c	Speed of light in vacuum = $3*10^8$ m/s
C_g	Geometric concentration ratio
CPV	Concentrated photovoltaic
CSOC	Concentrator Standard Operating Conditions
CSR	Circumsolar radiation
DNI	Direct normal irradiance (W/m^2)
DNI_{indoor}	Direct normal irradiance (W/m^2) , test conditions in datasheet
DNI_{model}	Modelled direct normal irradiance (W/m^2)
$E_{AM1.5D}$	Spectral irradiance (W/m^2/nm) for the reference spectrum AM1.5D
EL	Electroluminescence
E_{mod}	Modelled spectral irradiance (W/m^2/nm)
EQE	External quantum efficiency (%)
FF	Fill factor (%)
GNI	Global normal irradiance (W/m^2)
h	Planck's constant = $6.626*10^{-34}$ J.s
HCPV	High concentrated photovoltaic
IEC	International Electronic Comission
IMM	Inverted metamorphic multi-junction cell
I_{mid}	Middle sub-cell's short-circuit current (A)
I_{sc}	Short-circuit current (A)
$I_{sc,indoor}$	Cell's short-circuit current (A), test conditions in datasheet
I_{top}	Top sub-cell's short-circuit current (A)
I-V	Current-voltage characteristic
J_{sc}	Short-circuit current density (A/m^2)
LCPV	Low concentrated photovoltaic
LM	Lattice matched multi-junction cell
MM	Metamorphic multi-junction cell
MPP	Maximum power point
NREL	National Renewable Energy Laboratory

P_{meas}	Measured maximum power (W)
P_{mp}	Power at maximum power point (W)
P_{pred}	Predicted maximum power (W)
PW	Precipitable water (cm)
q	Elemental charge constant = $1.602*10^{-19}$ C
QD	Quantum dot
QualAr	Base de Dados On-line sobre Qualidade do Ar
SMARTS	Simple Model of the Atmospheric Radiative Transfer of Sunshine
SMR	Spectral mismatch ratio
SR	Spectral response (A/W)
SR_{mid}	Middle sub-cell's spectral response (A/W)
SR_{top}	Top sub-cell's spectral response (A/W)
SZA	Solar zenith angle (Degrees º)
T_1	First optics's transmittance (%)
T_2	Secondary optics's transmittance (%)
$T_{ambient}$	Ambient temperature (ºC)
TJ	Triple-junction solar cell
V_{oc}	Open-circuit voltage (V)
Wind	Wind speed (m/s)
Z	A spectral parameter to describe the current mismatch

1. Introduction

On the past few decades, electricity generated from solar technologies has shown humankind that a substantial portion of the demand for energy can be achieved without burning fossil fuels or creating nuclear reactions. Although unable to provide base-load, photovoltaics can generate electricity for a wide range of applications, scales and climates. Furthermore, the urge for technologies that made photovoltaics cost-effective, as well as breakthroughs in fundamental understanding, have been enabling progress in methods and materials, having enriched the photovoltaic market with other areas of knowledge. This led to the development of more sophisticated solar cells and assemblies that make a better use of the sunlight than the conventional ones.

The light that comes from the sun and hits the surface of the Earth, known as solar irradiance, is a flux of particles called photons, which can be decomposed into its spectral distribution as a function of the wavelength. The energy of a photon decreases with wavelength. Since the conventional solar cells, made out of a single layer of Silicon, an abundant element in the Earth, are responsive to a relatively small wavelength range of the solar spectrum, other materials and arrangements were created in order to cover diverse and wider ranges more efficiently. An example of such devices consists in the combination of more than one layer of different responsive materials in a single cell, becoming a multi-junction solar cell. The great potential of multi-junction solar cells can also be enhanced if, considering the low density of the solar irradiance, the sunlight is concentrated onto a small area of solar cell, through the addition of optical components. The arrangement of both elements in a photovoltaic module led to the appearance of concentrated photovoltaic (CPV) systems.
CPV technologies commonly employ triple-junction (TJ) solar cells, thus requiring a detailed understanding of the spectral sensitivity and behaviour of each of the three responsive layers. The commission of a CPV system or power plant at a certain location must firstly concern the weather and irradiance characteristics, so that electrical generation and reliability may be estimated and evaluated. The short-circuit current (I_{sc}) is an important parameter that allows the analysis of the sensitivity of CPV cells and modules to spectral irradiance distribution variations, while the maximum instantaneous power (P_{mp}) relates to the electricity that can be delivered into a matched load. Both can be extracted from a current-voltage characteristic curve.

The aim of this dissertation is to compare the energy yield of different CPV Circadian Solar module prototypes with TJ solar cells from different cell manufacturers, relating the performance of each one to the environmental conditions and the spectrum of the sunlight. For this purpose, the research tracker installed in the Solar Campus of the Faculty of Science of the University of Lisbon was used. The tracker platform included not only the evaluated module prototypes, but also a set of instruments for weather and irradiance sensing, as well as I-V curve sampling, in order to study the reliability of the modules under field conditions, in the period from June of 2012 to July of 2013.

1.1. III-V triple junction solar cells – state of the art

Multi-junction solar cells have been studied since 1960 [1]. The first multi-junction device was demonstrated in the early 1980s, and it converted 16% of the solar energy into electricity [2]. In 1994, US National Renewable Energy Laboratory (NREL) broke the 30% efficiency barrier, when dual-junction devices were formed from AlGaAs grown on top of GaAs. Later in the 1990's, triple-junction (TJ) solar cells, with GaInP and GaAs both grown on the top of an active Ge bottom cell substrate, led to record efficiencies.
The high-efficiency structure of multi-junction solar cells makes them highly attractive for cost-effective terrestrial concentrator systems, if designed for the terrestrial solar spectrum and the high current densities under radiation concentration. Concentration is achieved by using lenses or mirrors to focus sunlight onto the small multi-junction solar cell. In the vast majority of tracking concentrator systems, focal optics are employed and, as a result, a CPV module must be accurately aligned with the sun at all time, since only the direct component of solar radiation can be used [3].
Still, multi-junction solar cells offer a low-cost viable technology for electricity generation, as costly semiconductor material usage is minimized, reducing the size of system parts and costs. Making CPV

systems is attractive for both on and off-grid power generation, but the BOS (Balance Of Systems) adds non-negligible cost elements to the overall system, since metals, glasses and composites give little margin for further cost reduction [4]. Therefore, increasing cell efficiency and lowering cell costs are great levers to mitigate system costs.

Modern crystalline III-V multi-junction solar cells begin as raw wafers, from which individual layers of crystalline semiconductor are formed on a substrate, in a process known as epitaxial growth. A typical TJ cell structure comprises three p-n junctions made from GaInP (top junction, generally responsive in the range of 350-700 nm), GaInAs (middle junction, responsive from 500- 1000 nm) and Ge (bottom junction, covering from 800-1800 nm) monolithically stacked on top of each other. They must be assembled in this exact order, so that the top junction, with the highest band-gap, can collect light from the shortest wavelengths in the solar spectrum, which means that photons with energy lower than that band gap will pass to the lower junction, and photons with energy lowest than this threshold traverse to the lowest junction in the stack. In order to avoid significant voltage drops, low resistive tunnel junctions must be used to connect these junctions.
The ability of a solar cell to absorb light at each wavelength within a specific spectral band and, consequently, generating electric current can be described by its spectral response (SR) curve. On the other hand, the external quantum efficiency (EQE) refers to the percentage of absorbed photons that may produce electron-hole pairs, i.e. it is a measure of how many photons in the spectral band produce minority charge carriers which are subsequently collected by the device to form useful current [4], hence already including the effect of optical losses such as transmission and reflection. EQE relates to SR by:

$$\boldsymbol{EQE_{sub-cell}(\lambda) = \frac{hc}{q\lambda} SR_{sub-cell}(\lambda)} \quad (1)$$

where $\boldsymbol{h}$ is the Planck constant, $\boldsymbol{c}$ the speed of light in vacuum, $\boldsymbol{q}$ the elementary charge and $\boldsymbol{\lambda}$ the wavelength.
The EQE is intrinsic to the light absorbing material and not the cell as a whole. An example of EQE of a TJ solar cell is shown in Figure 1, where the individual cell efficiencies, chosen for a different range of the spectrum, can be seen and the total efficiency of the junction is largely increased when they are added up together [5].

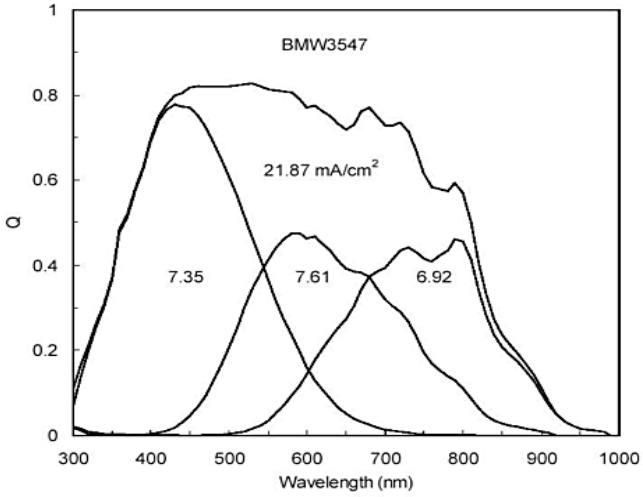

Figure 1 – Example of EQE of a TJ solar cell [5]: individual cell efficiencies (lower lines) and total efficiency of the junction (highest curve).

Alloys of groups III and V of the periodic table are good candidates for fabricating multi-junction cells: their band-gaps span a wide spectral range, most of them have a direct electronic gap, implying a high absorption coefficient, and their complex structures can be grown with extremely high crystalline and optoelectronic quality [6]. Currently, the most preferred III-V alloy configuration is the

AlGaInP/GaInAs/Ge system (Figure 2, a), since material and conditions availability enable layers with high quality, surface passivation and wide ranges in doping levels to be attainable.

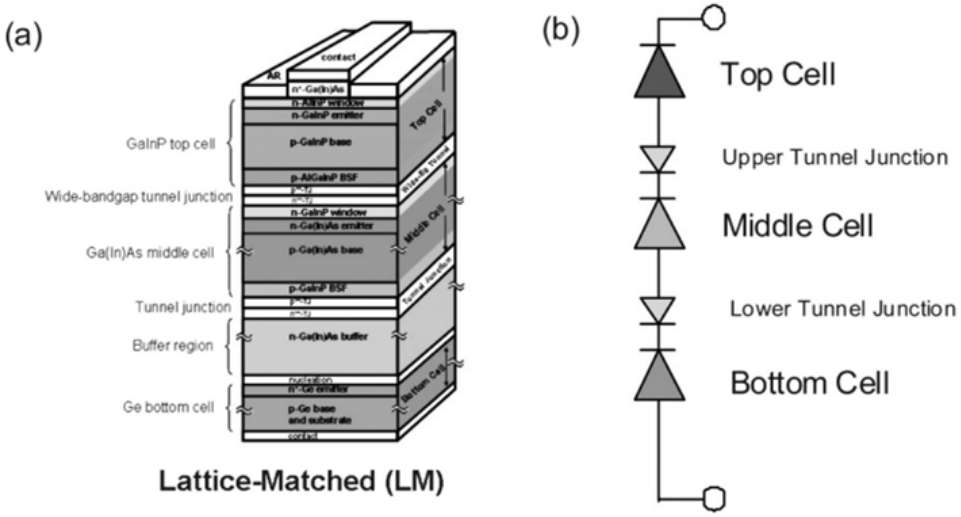

Figure 2 – Physical schematic of a monolithic TJ solar cell (a) and the electrical circuit equivalent (b) [4].

As series-connected devices, the voltages of the diodes add up; however, it is imperative that the tunnel junctions voltage drops are minimized, as they are assembled in inverse polarity (Figure 2, b). On the other hand, the current is limited by the sub-cell that produces the lowest current in the string, thus the current balance between sub-cells represents an additional challenge.
The short-circuit current density (J_{sc}) of each sub-cell is determined by the quantum efficiency of the sub-cell, QE(λ), and by the spectrum of light incident on that cell $\Phi_{inc}(\lambda)$ [7]:

$$\boldsymbol{J_{sc} = q \int_{\lambda_i}^{\lambda_f} QE(\lambda)_{sub-cell} . \Phi inc(\lambda) . d\lambda} \quad (2)$$

Short-circuit current density, or only short-circuit current (I_{sc}) when the area of the cell is considered, is one of the most important parameters for photovoltaic evaluation in general, but specially for CPV, since studying I_{sc} provides a means to avoid the voltage temperature dependence. Besides, as the current balance among sub-cells is essential, due to its great sensitivity to spectral changes, I_{sc} can be taken as a measure of the spectral variations and can provide an insight into cell technology optimization. Manufactures typically design cells such that the top and middle junctions alternate in the role of limiting current, while the bottom junction always has surplus current. The top and middle junctions are generally grown to be current matched for the AM1.5d reference spectrum [8].

Important parameters, besides I_{sc}, can be extracted from the I-V characteristic of the solar cell (Figure 3) for a cell under illumination. The open-circuit voltage (V_{oc}) denotes the point in the I-V curve where the internally generated dark current equals the illumination current. At biases bellow V_{oc}, the solar cell produces power that can be transferred to an electronic load and utilized. The maximum power point (MPP) is the point at which the I-V product is maximized. Many systems are designed to operate close to this point, at which the devices are cooler since there is a maximum transfer of energy from the transfers to the output current and hence less heat generated at the solar cell.

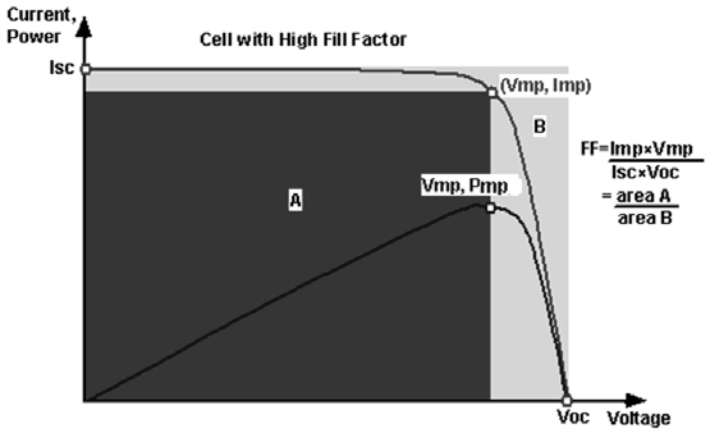

Figure 3 – Typical I-V characteristic for a solar cell, with relevant parameters assigned.

Another parameter that can be extracted from an I-V curve is the fill factor (FF), a measure of the "squareness" of the I-V curve, which gives an insight into the cell quality. Most high quality III-V multi-junction concentrator cells have FF in the mid to high 80% range [4]. If the intensity of the incident spectrum is known, the efficiency of the solar cell can also be determined through I-V curve analysis. I_{sc} and V_{oc} increase with concentration, as well as FF and efficiency, but suffer a drop when certain levels are reached (approximately 300 suns), at which series resistance becomes dominant [9] and recombination processes differ [10].

One possible configuration of TJ solar cells are known as metamorphic (MM) where the top two sub-cells are grown on a metamorphic buffer so that they are lattice-matched (LM) to each other, but lattice-mismatched to the Ge sub-cell. This allows lower band-gaps for the top and middle junctions, enabling a more advantageous band-gap combination for conversion of the solar spectrum, whereas some of the current that would be wasted in the Ge bottom cell to be captured by the top two sub-cells. Another type of metamorphic TJ cell, the inverted metamorphic (IMM), replaces the bottom sub-cell with a metamorphic GaInAs layer, enabling the growth of the other sub-cells with smaller lattice-constant and higher band-gaps, resulting in a higher voltage compared to LM cells [4].
In recent years, it has been proposed and experimentally verified that the use of nanostructures, such as quantum dots (QD), offer the potential for high photovoltaic efficiency, since the quantized energy states of QD can function as intermediate bands for efficient absorption of photons in the solar cell structure, providing additional spectral response and stronger light absorption at long wavelength [3]. A system with an infinite number of sizes of QD has the same theoretical efficiency as an infinite number of band gaps or 86.8% [2].

Significant progress at cell level has been achieved every year. A recent efficiency of 43.5% is reported for a 0.167cm^2 IMM TJ cell (InGaP/GaAs/ InGaAs), fabricated by Sharp and measured at the Fraunhofer Institute for Solar Energy Systems at an intensity of 306 suns [11]. Nevertheless, more technical advances are still needed to trigger the feasibility of low-cost CPV.

1.2. The solar spectrum

Radiation from the sun sustains life on earth and determines climate. The energy flow within the sun results in a surface temperature of around 5500 ºC, so the spectrum of the radiation from the sun outside the earth's atmosphere (extraterrestrial spectrum) is similar to that of a blackbody at such temperature.
The spectrum of the solar radiation at the earth's surface has several components: direct radiation that comes straight from the sun (collimated with an angle of approximately 0.53°), diffuse radiation that is incident from the hemispheric sky and, ground reflections and scatter, and global irradiation, the sum of the direct and diffuse components. Unlike the direct irradiation measurement, which is always

measured in a surface perpendicular to the incoming solar radiation, a measurement of global irradiation has to state the direction of the global irradiation target surface.
All the radiation that reaches the ground passes through the atmosphere, which modifies the spectrum by absorption and scattering (Figure 4). Many studies have been made with the purpose of understanding how atmospheric content can impact spectral irradiance [12][13][14][15][16] and, thus, the performance of different solar applications.

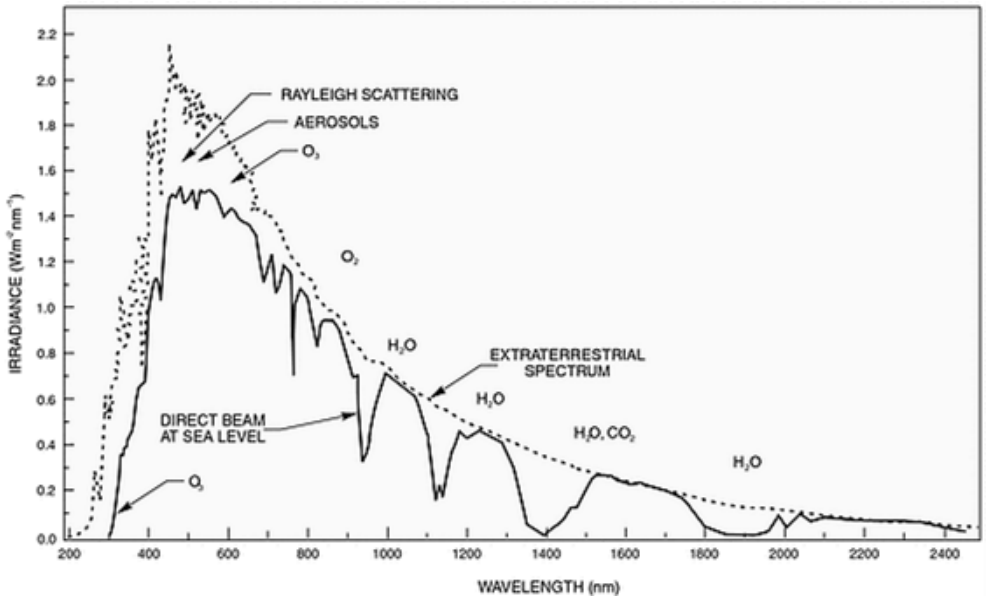

Figure 4 – Normally incident solar spectrum at sea level on a clear day (solid line) and extraterrestrial spectrum (dashed line), with respective absorptive bands [17].

Air mass

The ground level spectrum firstly depends on how far the sun's radiation must pass through the atmosphere. Elevation is one factor, but the most significant changes are due to the earth's rotation, which varies the length of the path the radiation must take to reach ground level. Air mass (AM) refers to the relative path length of the solar beam through the atmosphere (Figure 5, a) and depends on the angle of the sun from the horizontal (solar zenith angle, SZA) or from the horizon (solar elevation). AM 0 is defined as solar radiation that has not passed through the atmosphere, but AM takes the value 1.0 when the sun is directly overhead (SZA=0º and typical path length ~100km), 1.5 when at 48.2 º from the vertical, which is the case for the ASTM AM1.5 reference spectra, and 2.0 when the sun is at 60º [13]. Due to the tilt of the Earth, this parameter is greatly dependent on latitude and season.

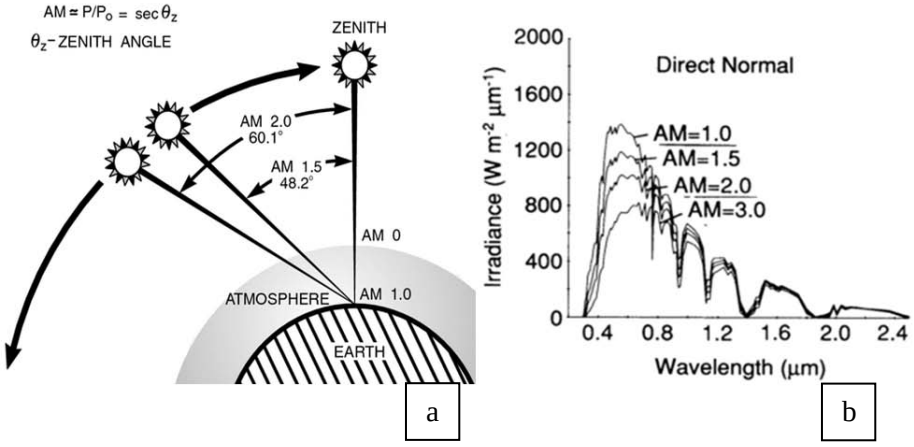

Figure 5 – a) Air mass variation with solar zenith angle, b) Variation of a simulated spectrum [13] with increasing AM, with other variables held constant.

High efficiency multi-junction solar cells are quite sensitive to fluctuations in AM in particular, which is due to the fact that as AM assumes higher values, i.e. longer path the solar radiation has to cover to reach the ground, there will be a higher chance for scattering and absorption of solar radiation by atmospheric constituents, resulting in strong attenuation of short wavelength light (Figure 5, b). It is when such AM values are met that a cell becomes badly current mismatched, once the top junction predominantly loses current, resulting in a dramatic drop in module efficiency [18], as will later be discussed. Fortunately, efficiency at high air mass is relatively unimportant because the net power output is small under these conditions, which occurs in the earlier and later hours of the day, hence with low light intensity [7].

Atmospheric aerosol optical depth

Rayleigh scattering, wavelength dependent, and scattering from aerosols and other particulates, including water droplets, also change the spectrum of the radiation that reaches the ground; however, the level of absorption and scattering change with the constituents of the atmosphere. Atmospheric aerosol optical depth (AOD) is a dimensionless quantity, usually specified at a single wavelength, typically 500 nm, although AOD values at other wavelengths can also be measured [19]. A value of 0.1 indicates a relatively clear atmosphere and a value of 0.4 indicates a relatively turbid atmosphere, providing a measure of aerosol loading at 500nm (see Figure 6).

The spectral effects of aerosol attenuation depend on the size of particles relative to the wavelength of solar irradiance, but are generally enhanced with decreasing wavelength and for direct irradiance. For instance, large aerosol particles are usually associated with sea salt and mineral dust, particularly relevant along coastlines and in deserts, whereas small aerosol particles are indicative of urban pollutants and biomass combustion. Though, a strain with AOD regards to its rapid variation over both time and space, difficult to predict [20]. This makes aerosol optical properties subject of great variability on a day-to-day basis, and consequently spectral irradiance becomes less predictable, since different wavelength ranges are affected by different kinds of particles [21].

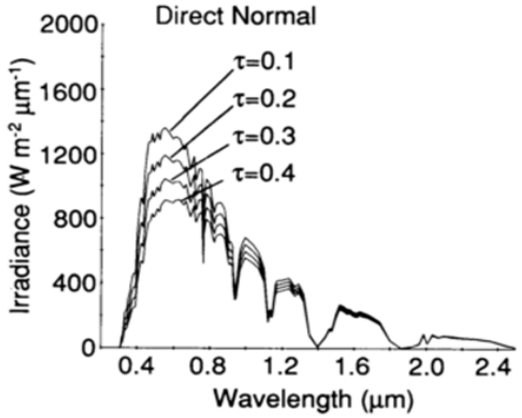

Figure 6 – Variation of a simulated spectrum [13] with increasing AOD at 500nm (the same as τ), with other variables held constant.

The aerosol loading of the atmosphere leads to a considerable scattered radiation appearing to come from an aureole around the solar disk, which is called circumsolar radiation.

Furthermore, oxygen, either atomic or molecular, and nitrogen also absorb radiation, mainly in wavelengths <190 nm. Ozone strongly absorbs longer wavelength ultraviolet radiation in the region from 200 to 300 nm, weakly absorbing visible radiation, and shaping the UV edge of the terrestrial solar spectrum. Carbon dioxide, and to a lesser extent, oxygen, selectively absorb radiation in the near infrared as well. The concentration of pollutants in the atmosphere is highly variable on a day-to-day basis; however, their effects on spectral irradiance are somehow negligible for CPV. For instance, the effect of NO_2, which plays a key role in the complex ozone cycle, is only significant, or more important than ozone, in polluted atmospheres [22].

Still, in the case of water vapour, it has absorption bands in both the visible and near-infrared parts of the solar spectrum, relevant to multi-junction solar cell performance. In fact, AM and AOD effects on the consistency of low-bandgap devices performance, such as the Ge bottom junction, are smaller than precipitable water [13]. Absorption bands corresponding to the bottom junction are the strongest, but because this junction is not expected to limit the current on a TJ cell, precipitable water has little effect on cell performance. Precipitable Water (PW) is the measure used for calculating atmospheric absorption caused by water vapour (Figure 7), so a value of about 1 cm is representative of a relatively dry atmosphere and a value of about 5 cm stands for a relatively wet atmosphere.

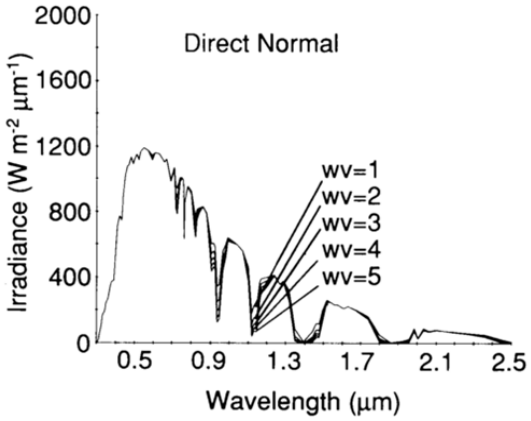

Figure 7 – Variation of a simulated spectrum [13] with increasing PW (the same as WV), with other variables held constant.

Since the solar spectra depend on many variables, standard spectra have been developed to provide a basis for theoretical evaluation of the effects of solar radiation and as a basis for simulator design. These standard spectra start from a simplified version of the extraterrestrial spectra and employ sophisticated radiative transfer models for the effects of the atmosphere to calculate terrestrial spectra. ASTM publish three spectra - the AM 0, AM 1.5 Global for a 37° tilted surface and AM 1.5 Direct, a reference for concentrator modules [9].

1.3. CPV in Portugal

CPV systems are ideally suited for high irradiation regions around the globe, mainly in sunbelt regions with high direct sunlight. This type of technology produces a very high energy yield, even in locations affected by high temperatures and, despite the additional cost of continuous accurate tracking of the sun, CPV can offer a cost advantage over conventional silicon based PV technology. The regional knowledge of direct normal irradiation is then extremely important for the deployment of CPV systems.

Portugal experiences air masses very close to 1 in the summer and greater than 2 in winter. This country represents a good candidate for CPV development, especially in the South (in regions like Algarve and, at a certain extent, Alentejo), as these locations meet high number of sun hours (Figure 8), corresponding to 68% of a year. On the other hand, a typical mediterranean climate is felt, with annual average ambient temperatures around 17ºC [23].

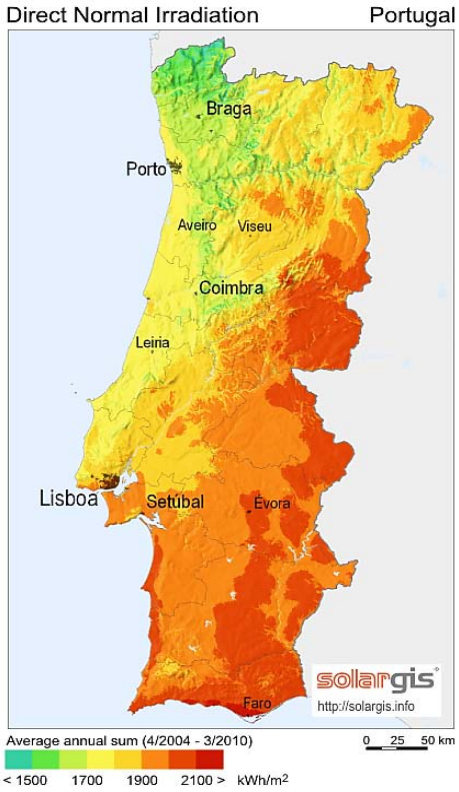

Figure 8 – Map of direct normal irradiation in Portugal [24].

Some Portuguese companies have developed concentrator systems over the past decade. WS Energia, for instance, is a pioneer in Low Concentrated Photovoltaics (LCPV) and the first Portuguese company in Photovoltaic Standard Committees in IEC. Moreover, several other companies started researching and installing High Concentrated Photovoltaic (HCPV) technologies, as well, such as Magpower, existing since 2002 and based near Lisbon. This company is one of the world's largest manufacturers of CPV solar modules and trackers, having accomplished high reliability worldwide. A 12MW CPV power plant was installed by Magpower in the south of the country, as well as a 0.5 MW, installed in north of Lisbon and a 3 MW, in Estoi, south of Portugal. Another HCPV project of 1MW to be installed in Alqueva (Alentejo, near the border with Spain), by the Portuguese company Tecneira, is still in development.

On the other hand, many corporations worldwide have also implemented CPV technologies in Portugal, either for electrical generation or for research purposes. This is the case of Circadian Solar that have been testing the reliability of their modules and assessing cells from different manufacturers, in other to compare the performance and energy yield of different cells technologies under field conditions. Throughout this assessment, the process of a HCPV performance evaluation and selection of a proper cell technology is presented.

2. Methodology

As TJ cells are designed so that each junction collects photons from different parts of the solar spectrum, having knowledge on the spectral variations on a seasonal and day-to-day basis is crucial to make a good judgement on which cell technology will perform better under certain conditions. However, accessing the solar spectrum distribution on-site can be not just very costly but also inaccurate, depending on the instrument that is employed. To overcome such issues, numerical models to simulate the solar spectrum distribution have been created and perfected throughout the years. One of those models will be employed in this assessment, the Simple Model of the Atmospheric Radiative Transfer of Sunshine (SMARTS) [25][26].
This dissertation deals with the assessment of a CPV system outdoor performance prediction and evaluation. For this purpose, the methodology outlined in Figure 9 is proposed.

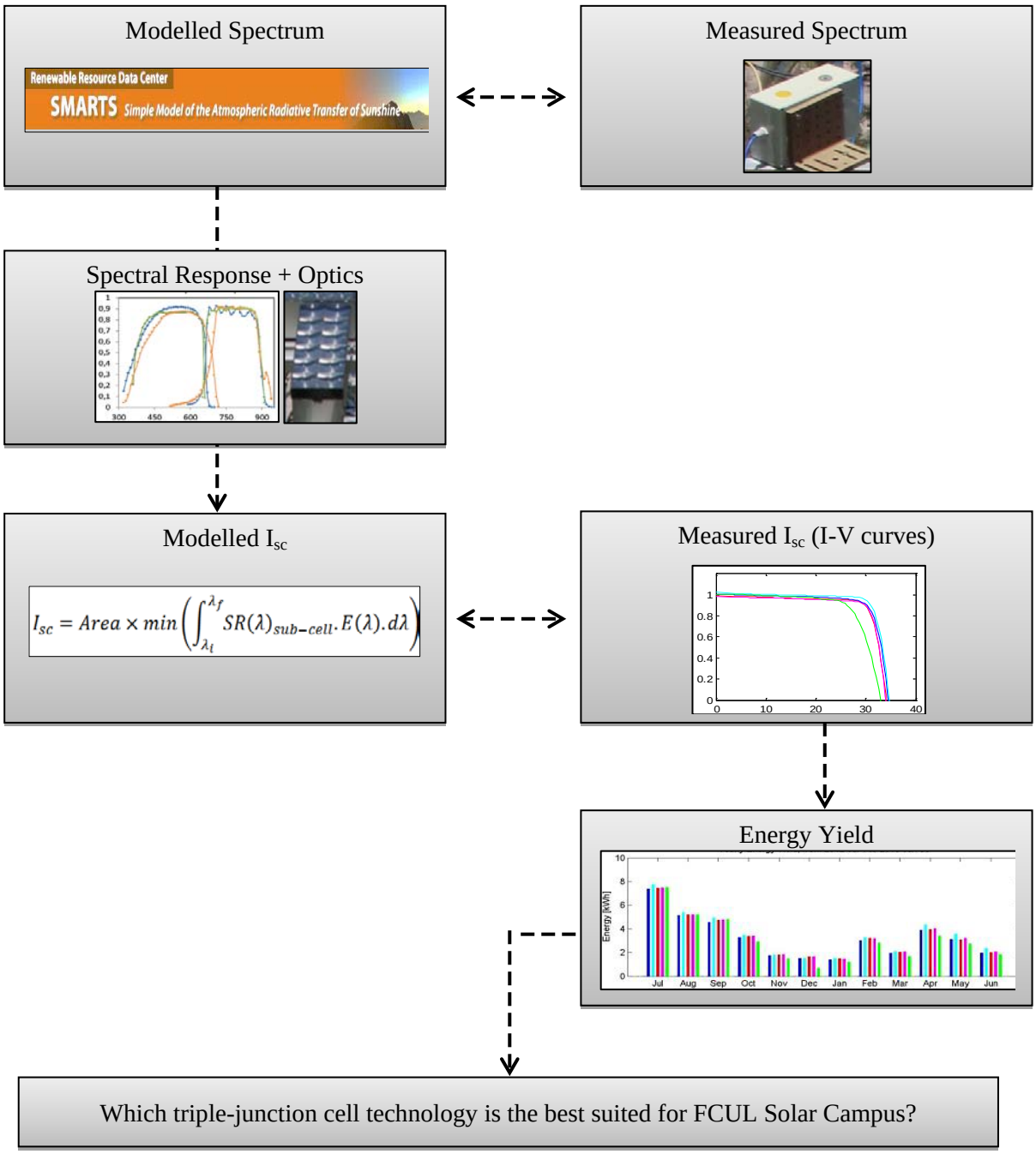

Figure 9 – Schematic presentation of the approach taken on this assessment.

Spectral irradiance measurements are performed by a device mounted on the research CPV tracker and compared with modelled spectral irradiance distribution determined from measured and assumed atmospheric parameters.
The spectral distribution data is then used to determine the performance of the solar cells. For this purpose, one has to take into consideration system parameters such as the intensity and spectral transfer functions of the optics and the quantum efficiency of the solar cells. It is important to notice that some relevant parameters such as the cell or module temperature, have not been measured on-site and therefore there is no straightforward way to come up with a theoretical estimate for V_{oc}. Fortunately, as TJ cells are connected in series and, in the case of the evaluated modules, assembled in small and compact structures, it is not expected that ambient temperature will have great impact on this parameter. Thus, the main concern will regard I_{sc}, a parameter that is very sensitive to spectral conditions, regardless of temperature. In fact, different from crystalline silicon solar cells, CPV using III-V multi-junction cells are much more sensitive to the solar spectrum distribution than the operating temperature [12].
The estimation of I_{sc} can be validated against on-site I-V curve measurements. It may then be used to make predictions that may be useful to estimate production in different locations, where different weather conditions may be expected.
Finally, integrating the P_{mp} extracted from the I-V curves, on a daily, monthly or yearly basis, and applying a power rating methodology, enables to point out which TJ cell is the best suited for production, either for reference conditions or for the site weather and spectra

The details of each step of the methodology are described below. In this work, we compare the output of three sets of solar cells, from different manufacturers. For commercial reasons they are simply named A, B, C and are colour coded according to the manufacturer. Whenever there is more than one module with solar cells from the same manufacturer, different tones are used (e.g. light and dark blue, red and pink). Finally, this analysis is referred to 12 months of data collection, from July 1012 to June 2013. For different parts of the analysis, four clear sky days were selected as study cases: an autumn day, the 12th of November of 2012, a winter day, the 4th of January of 2013, a spring day, the 17th of April of 2013, and a summer day, the 15th of June of 2013.

2.1. Radiative Transfer Model

The variables that have the largest impacts on spectral irradiance variations and, thus, on direct normal irradiance (Figure 10) at the surface, are cloud cover, air mass, atmospheric aerosol loading, precipitable water vapour and, to a lesser extent, surface pressure, ground reflectance and amount of ozone [13].

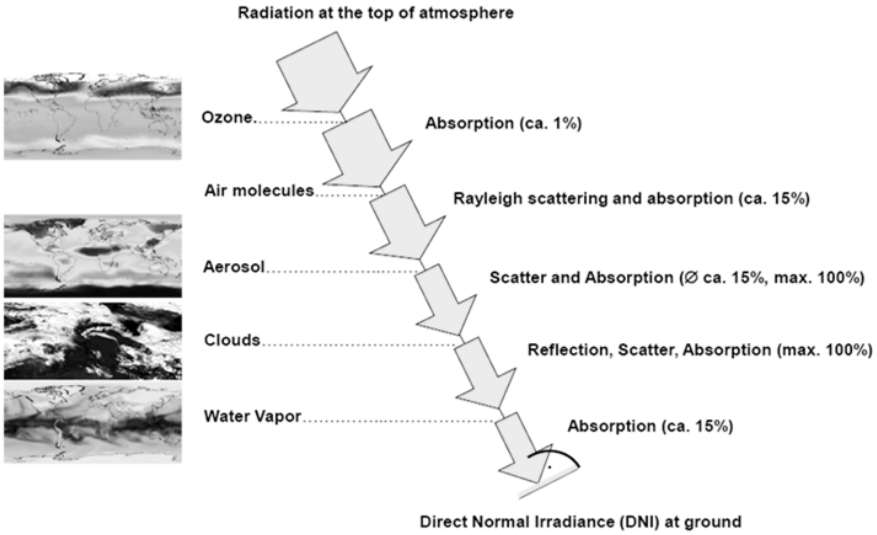

Figure 10 – Path of solar radiation through the atmosphere [27].

When predicting the output current of devices such as CPV modules with TJ cells it is of extreme importance to use the most accurate data available so that the solar spectrum can be as close as possible to the operating conditions. Spectroradiometers measure spectral irradiance, but they are expensive instruments and due to their typically uncertainty of 5-10% [28] they are not commonly employed. Besides, their use is not trivial, especially when outdoor solar spectra are to be measured continuously and reliable over several months [14].
In order to qualitatively estimate the solar radiation spectrum at a given location it is appropriate to use available numerical models. These models have been developed to provide the community with predictions of solar radiation when or where it is not measured appropriately or at all [29] and commonly take many of the parameters mentioned above into account. For this assessment, we have used the SMARTS radiative transfer model. The following sessions describe the atmospheric data used as input and the model implementation.

2.1.1. Atmospheric data

In this assessment, a sun position algorithm [30] was used to calculate the AM (air mass) from the SZA (solar zenith angle) for the considered period (Figure 11). As expected, as the site of this study is located on the northern hemisphere, lower values of AM are seen during the summer time.

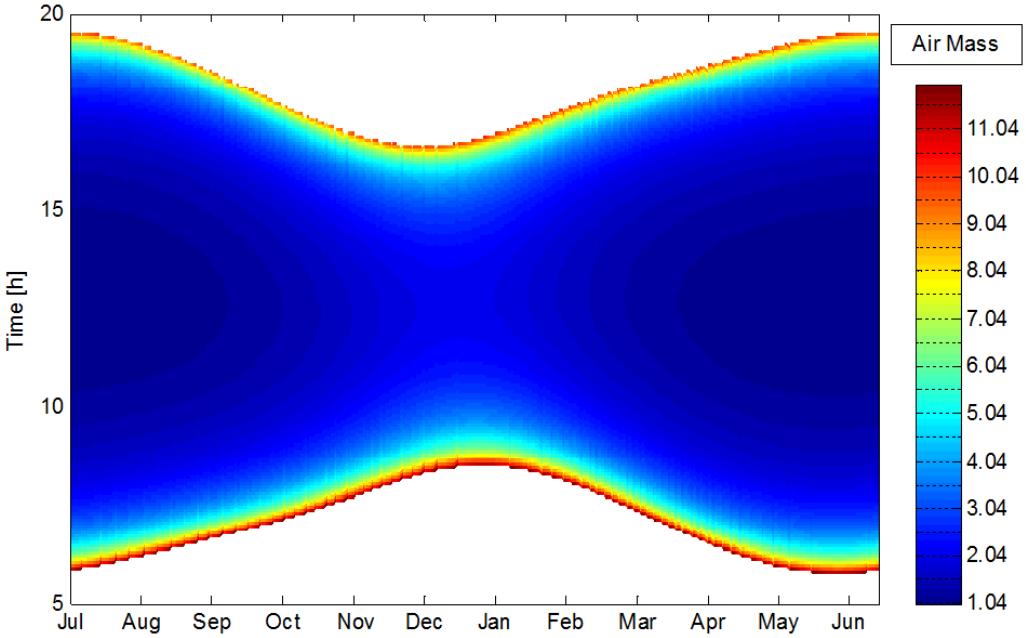

Figure 11 – Air mass variation in the site from the 1st of July 2012 to the 31th of June 2013.

It can be noted that the condition AM=1.5 is never met during the period from the middle of October to the end of February. Besides, in December AM is always greater than 2 and, as expected, June has the lower air masses, with AM=1.04 as the lowest value.

If the air mass is calculated easily and with high accuracy as a function of the solar geometry, other variables such as turbidity and precipitable water are difficult to model and seldom measured [25].
For the purposes of radiative transfer calculations, the AOD is specified at 500 nm. AOD values at other wavelengths are calculated inside SMARTS using pre-computed aerosol models. Fortunately, there are many databases from locations all over the world containing some of the required parameters. Although, this data may not allow the output of a model to be as precise as it would be if measured on-site, so, depending on the desired level of accuracy, the results can be quite reliable.
As on-site AOD measurements were not available, data from the AErosol RObotic NETwork (AERONET) was used. AERONET [31] is a federation of ground-based remote sensing aerosol networks that provides a long-term, continuous and readily accessible public domain database of aerosol optical, microphysical and radiative properties for aerosol research and characterization [32].

Data from the two Portuguese AERONET sites were considered, which are both run by the Observatory of Physics of Atmosphere of the Centre for Geophysics: Cabo da Roca (30.46 N, 9.30 W), 30km northeast of Lisbon in the installations of Cabo da Roca lighthouse, and Évora (30.34 N, 9.54 W), Colégio Luis Verney, Universidade de Évora.
AOD data is presented for three data quality levels: Level 1.0 (unscreened), Level 1.5 (cloud-screened) and Level 2.0 (cloud screened and quality-assured). Since there was no Level 2.0 data available at the time, level 1.5 data was used, which provides a reasonable method of characterizing CPV performance, as these systems only accept the direct component of total solar irradiance.

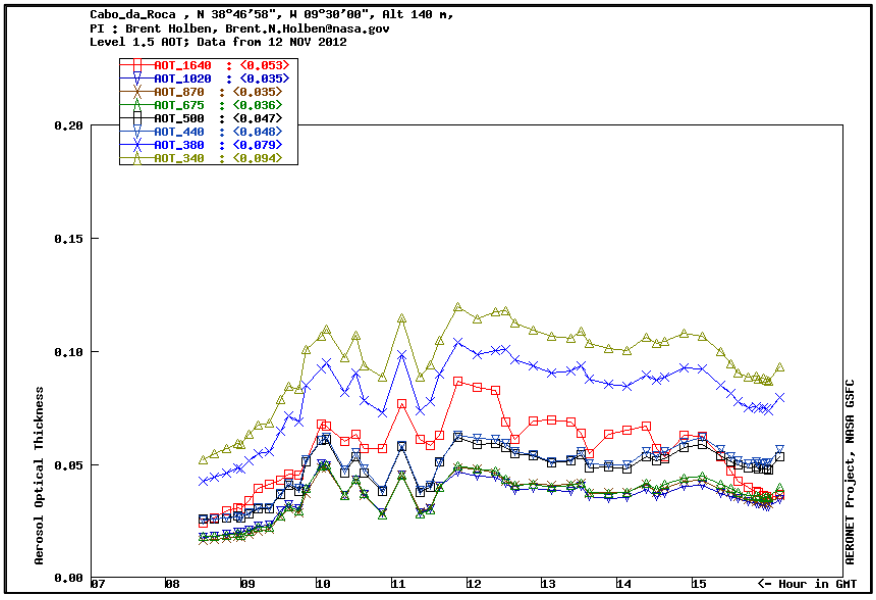

Figure 12 – Example of AOT (the same as AOD) measurements taken at Cabo da Roca AERONET site, for 12th November 2012.

As an input for the radiative transfer model, only AOD at 500nm was employed (black line on Figure 12). In spite of Cabo da Roca being 5 times closer to Lisbon than Évora, data from both locations were considered as input, since there is a clear positive relationship between them (Figure 13), suggesting that both sites show similar temporal variability in aerosol loading, with slightly higher values tending to be prevalent at Évora.

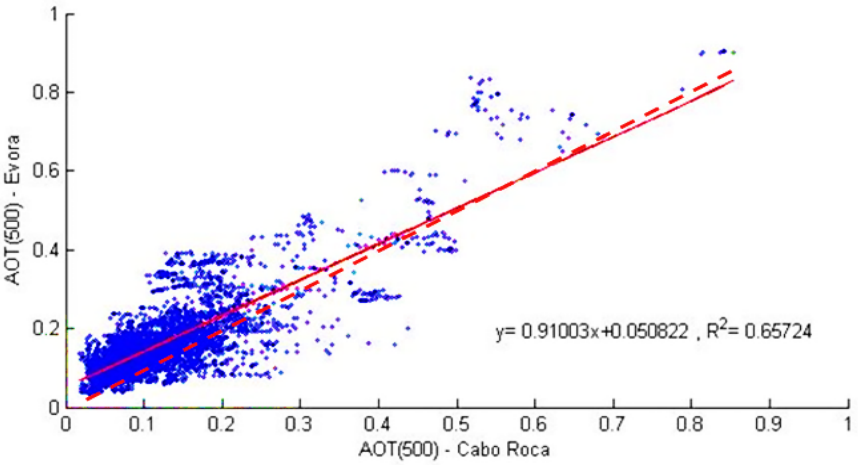

Figure 13 – Linear correlation between AOT (the same as AOD) from Évora and Cabo da Roca for the available months of 2012. Dashed line represents a 1:1 relationship, dashed line is a least-squares fit to data points with a gradient of 0.91.

Only the average of daily AOD at the two sites was considered as a rough approximation for the true AOD at the site, following the approach used elsewhere [18]. This allows an easier input preparation for the model, since conflicts due to too many hourly missing values either due to equipment downtime or cloudy conditions are avoided. With this approach, seasonal behaviour is still being captured without the noise of short term variations.

On-site measurements of relative humidity and ambient temperature were made using proper devices, described below in section 2.5.2. These values can be employed to perform a calculation of the PW internally in the radiative transfer model, using standard equations [33]. The result will be only approximate, but reasonable capturing the daily behaviour of PW.

As the site is located fairly close to intensive road traffic, it is also of interest analysing data from any air-quality station near this road. The closest one is found at Praça de Entrecampos, Lisbon (38.44N, 9.08 W) and its data, since 1992, can be accessed on the on-line QualAr database of Agência Portuguesa do Ambiente (APA) [34].
An example of the concentration of tropospheric NO_2 for the 17th of April of 2011 can be seen in Figure 14. The measurements are available on-line only on October of the following year, so data for 2012 was not available at the time of this analysis.

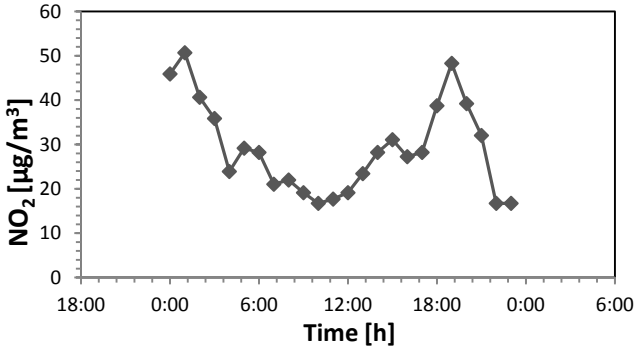

Figure 14 – NO_2 concentration for the 17th of April of 2011, at Entrecampos QualAr station.

For this analysis, more recent values could have been used, although, as the concentration of pollutants is not only seasonal but dependent on weather parameters, such as wind speed and temperature, and socioeconomic aspects, such as the amount of car circulation and industrial production, the level of pollution at the site was evaluated taking data from the 17th of April of 2011 into account. However, on the other hand, no further importance was given to these gaseous concentrations, since ozone, nitrogen dioxide or site pressure have only a second-order impact on DNI. Consequently, their accuracy is of much less concern [20] and has negligible impact on CPV efficiency [18].

2.1.2. SMARTS2

SMARTS2 is a radiative transfer model able to calculate the solar shortwave direct beam irradiance from spectral transmittance functions for the main extinction processes in the cloudless atmosphere: Rayleigh scattering, aerosol extinction, and absorption by ozone, uniformly mixed gases, water vapour, and nitrogen dioxide [35]. Therefore, SMARTS2 also represents a readily available tool that can be used to predict the effects of changing optical AM, PW, and AOD on triple junction cell performance. This model plays an important role on this assessment, since it has not just successfully served the CPV industry for many years, but has also been known for its excellent accuracy, being able to even replace measurements [36].
In order to run the spectral model, the construction of an input file is needed. This text file must contain 17 parameters, called Card #, additionally some optional cards can be defined, denoted Card #a. One can define as many cards as the complexity of the analysis requires.

Table 1 presents an example of modelling the direct solar spectrum for the 17th of April of 2013, at the site location. For this purpose, an IDL routine was written for the input of site weather data and aerosol data for the model, whenever available.

Table 1 – List of input variables required for modelling daily spectra in the site. In this example, spectra for the 17th of April 2013 are modelled. Table adapted from [37].

Card #	Value	Description
1	'FCUL spectrum'	Text string as title for this run.
2	1	Site's pressure options, 1 to input surface pressure, altitude, and height in the optional card 2a.
2a	1013.25 0.084 0.002	Pressure = 1013.25mb, altitude = 0,084km, height = 0.002km.
3	0	Selection of the proper default atmosphere, 0 is used to define a realistic atmosphere in card 3a.
3a	rh_meas tair_meas tday_meas 'SUMMER'	Relative humidity, atmospheric and average daily temperature at site level from weather data, season='summer'.
4	2	Water vapour data, 2 means that it will be calculated by the program from values given of card 3a, using a Gueymard empirical model.
5	1	Select the appropriate ozone abundance, 1 to use a default value according to card 3.
6	0	Define the correct conditions for gaseous absorption and atmospheric pollution, 0 initiates extra calculations in card 6a.
6a	2	Defaults the tropospheric concentration of 10 pollutants according to the selected level of tropospheric pollution, 2 represents Light Pollution, according to QualAr data.
7	398.35	Carbon dioxide columnar volumetric concentration = 398.35 ppmv, in April 2013 [38].
7a	1	Selection of the proper extra-terrestrial spectrum, 1 is for a Gueymard unpublished synthetic spectrum, with a Solar Constant value of 1367.00W/m^2.
8	'S&F_URBAN'	Selects the aerosol model, 'S&R_RURAL' refer to urban ambient aerosol model.
9	0	Selects the correct turbidity data input, 0 is used to define aerosol optical depth at 500 nm on card 9a.
9a	tau_meas	Turbidity coefficient from AERONET data.
10	12	Selects the correct zonal albedo, 12 is for the Green grass option, with a non-lambertian reflectance type on the spectral range of 300-1190nm.
10b	0	Option for tilted surfaces, 0 means that this calculation will not be considered, since it's a sun-tracking surface.
11	280 4000 1.0 1367.0	Defines the spectral range, correction factor and solar constant, respectively 280-4000nm, 1.0 for no such correction and 1367 W/m^2 the solar constant.
12	3	Selects the results to be printed in the output file. Option 3 is for output both broadband and spectral results in a spreadsheet-like format.
12a	280 4000 1.0	Defines the spectral range between which results will be printed and the interval for printing.

12b	1	Total number of output variables to print.
12c	2	Defines the code number to select the spectral variables to print. Code 2 is Direct normal irradiance.
13	1	Option for controlling the calculation of circumsolar radiation, 1 is for simulate a typical radiometer.
13a	0 0.5 0	Slope angle = 0°, aperture of the simulated radiometer = 0.5°, limit angle = 0°.
14	0	Option for using a smoothing virtual filter in the output results.
15	0	Option for illuminance calculations, 0 to bypass this step.
16	0	Option for special broadband UV calculations, 0 to bypass this step.
17	3	Option for solar position and air mass calculations, 3 is used to input date and geographic location on card 17a.
17a	2013 4 17 hour_inp 38.757660 -9.156311 0	For a daily calculation: Year_inp=2013, Month_inp=4, Day_inp=17, Hour_inp=input, Latit=38.757660, Longit=-9.156311, Zone=0.

Through the SMARTS batch file, it is possible to make several runs varying the inputs of interest, which are, in this case, the hours of the considered day and the atmospheric data. Each run consists on the construction of an input text file containing the parameters for the transmittance and absorption functions used for the computation of the spectral irradiance distribution, taking the extra-terrestrial spectrum as reference. The results are then written to an output text file. Data from the several files makes it possible, for example, to plot the spectral irradiance distribution for specific moments (Figure 15) or throughout the day (Figure 16).

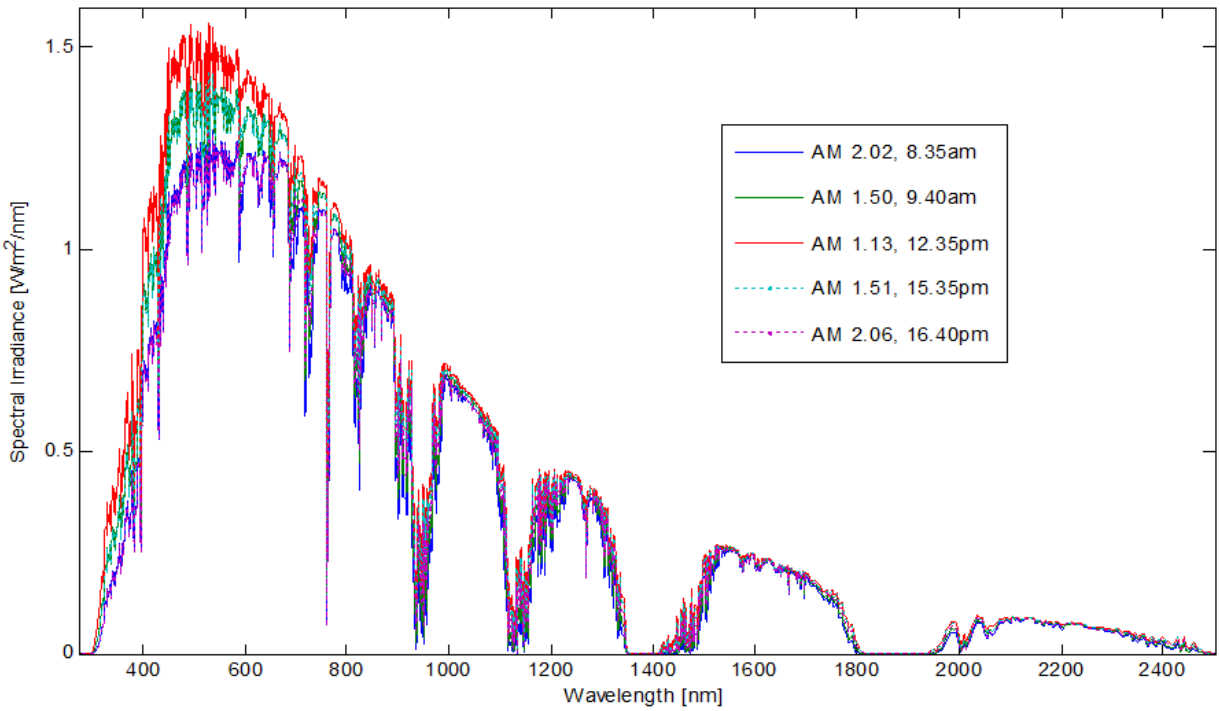

Figure 15 – Plot from 280 to 2500nm of the modelled spectral irradiance for several air masses and solar noon on the 17th of April 2013.

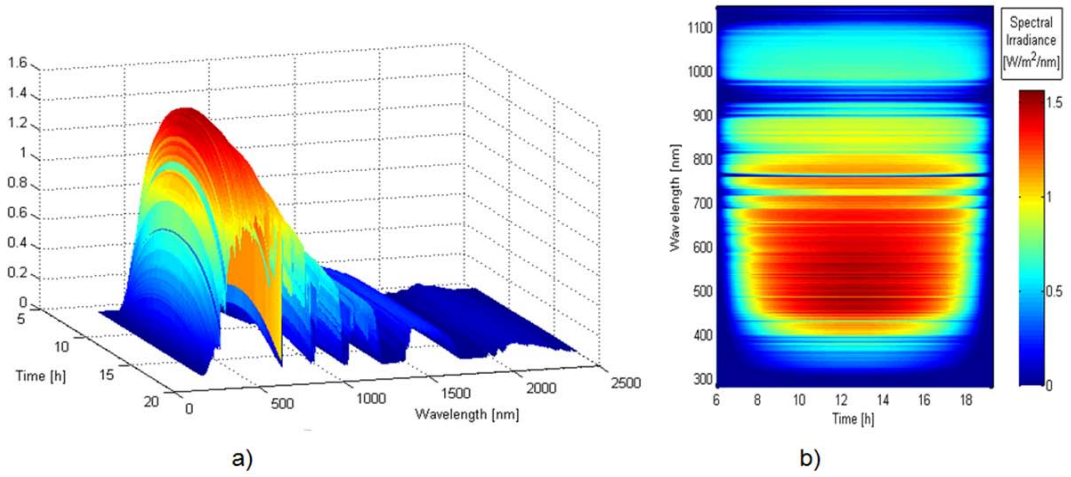

Figure 16 – Modelled spectral irradiance for the 17th of April 2013: a) 3D plot, b) surface plot.

The spectral irradiance distribution changes throughout the day, similarly before and after solar noon in a clear sky day. Redder spectra are found during the first and the last hours, when the sun is lower on the horizon and higher AM values are met, whereas bluer spectra are expected in the instants around solar noon.

2.2. Short-circuit current, I_{sc}

In order to determine the output of the solar cells from the spectral distribution of the incoming radiation it is necessary to consider the spectral response of the solar cells and the transfer function of the optics of the solar module. These are discussed in the next sections.

2.2.1. Spectral Response

As a first approach, the EQE data was taken from the datasheets given by the manufacturers (Figure 17, a). Nevertheless, as Circadian Solar has another test facility at the University of Cyprus in Nicosia where EQE measurements could be performed, some cells were sent there to be measured (Figure 17, b), so that they could be compared to the curves on the datasheets.

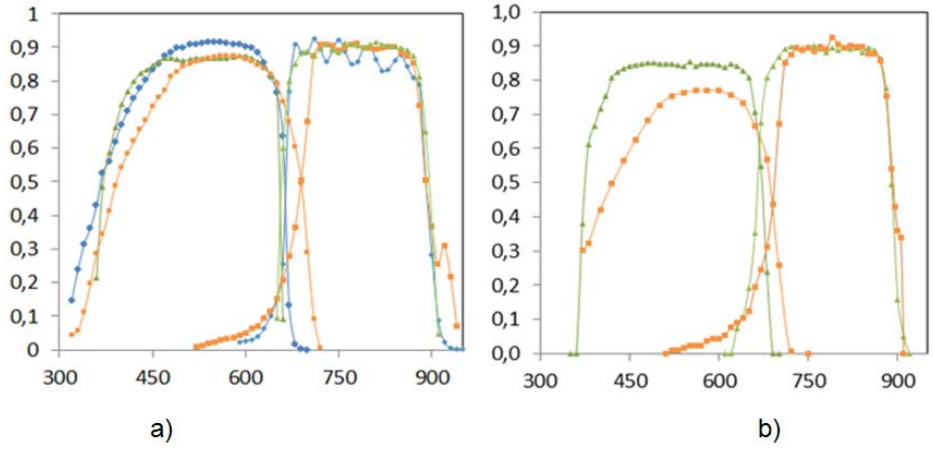

Figure 17 – External Quantum Efficiency: a) datasheet curves for cells A (blue), cells B (orange) and cells C (green), b) measured in Cyprus for cells B (orange) and cells C (green).

Unfortunately, the EQE data from Cyprus revealed to be improper for the assessment due to discrepancies on the top sub-cell of B type cells, for instance, which resulted in I_{sc} values that were too

far from the expected. For this reason, the calculations were performed using EQE from the manufacturers' datasheets.
Applying equation (1) to the EQE curves of Figure 17, a), the SR curves are obtained and plotted in Figure 18. Observing these curves, it is expected that cells B perform better for red-rich spectra than the other two cells, since their spectral response covers a wider part of the red and near-IV wavelengths. Cells A and C spectral responses are quite similar, so it is expected that they will produce similar I_{sc} under the same spectrum, regardless of temperature effects.

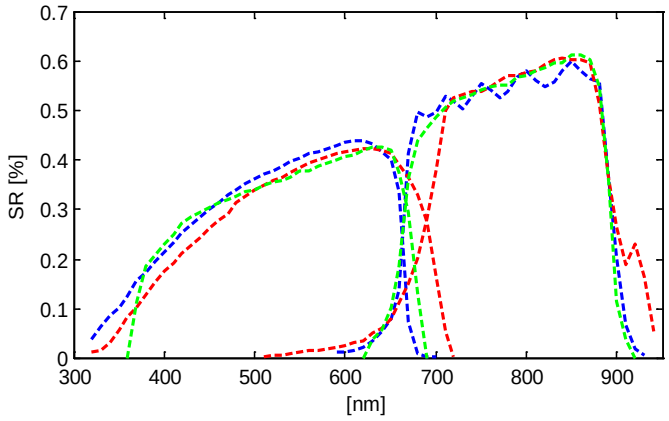

Figure 18 – Spectral response of the three cells, from 300 to 950 nm: cells A (blue), cells B (red) and cells C (green).

It is also important to clarify that the spectral response of bottom Ge junctions is not being considered, due to the fact that, in the case of a triple junction cell, the short-circuit current will only depend on the top two junctions, as mentioned earlier. Moreover, due to horizon shading at the test site, the DNI does not reach the modules in the earlier and later hours of the day, so it is guaranteed that the Ge junction will never limit the current. However, this junction plays an important role on maintaining a high fill factor [39], which guarantees an output power as high as possible.

2.2.2. Primary and Secondary optics

Most optical designs include both primary and secondary optics to increase tracking and alignment tolerance, which is the case for the evaluated modules. The majority of first optics uses lenses rather than mirrors. This simplifies the optical design and facilitates passive cooling, reducing design and maintenance complexity. However, several factors are still a challenge when designing the optics. For instance, water dew on optics [40], soiling[1] [41], imperfect optical interfaces, manufacturing imperfections, misalignment and thermal expansion [9] may cause crucial optical losses. Variability of the optical transmission is also unpredictable and the yellowing or pitting of plastic lenses and the need for washing, among other aspects, are also concerns.
For the secondary optics, which is exposed to great intensities, any absorption can cause large increases in temperature. Even if the secondary optic is 100% transparent, it may run hot because of being attached to the cell, which may operate +40°C or more above ambient temperature [42]. Therefore, the secondary optics must be able to withstand both high temperatures and the potential stress from differential expansion if the temperature distribution is non-uniform. Soling in the secondary optic and the associated heating can lead to catastrophic failure.
Concentrating optics tend to have lower optical transmission in the wavelength range of the top sub-cell, as shown in Figure 19, delivering a spectrum consistent with a higher effective air mass [39], so the advantage of re-optimization of the cell structure for higher effective air masses is reasonable. Furthermore, consideration must also be given to the current that should be available in the Ge sub-cell, the junction with lowest band-gap, so that it does not limit the overall current in the multi-

[1] Analysis of soiling rates for other Circadian modules, during the summer of 2012, showed a monthly 4% loss from modules that were cleaned every week to uncleaned modules.

junction cell when in the presence of high absorbing optics [4], high water vapour content in the atmosphere or red-rich spectra.

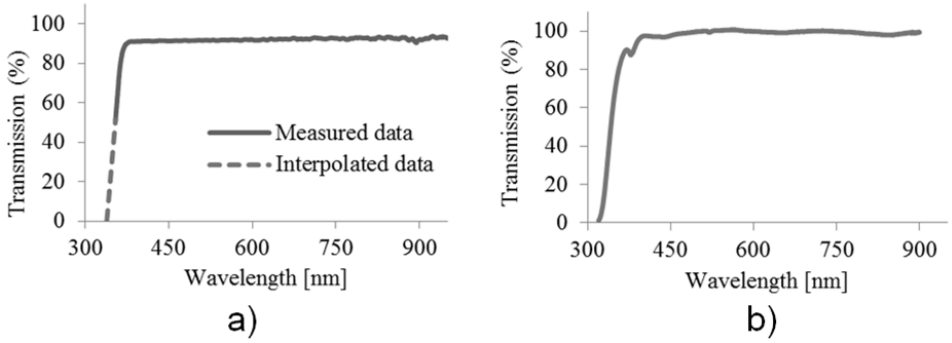

Figure 19 – Optical transmission functions for: a) primary and b) secondary (neglecting reflection from surfaces) on the evaluated modules.

For the system under analysis, the module primary optics is made of polymethylmethacrylate (PMMA), which is 3mm thick, and the secondary is glass, which is approximately 10mm thick, bonded to the cell with optically matched silicone. The efficiency of the PMMA lenses is generally around 83 – 86 % and should be around 94 – 96% for the secondary. This gives an overall 78 - 82% efficiency for the optical system; considering the issues mentioned above, the lower figure of 78% is preferred.

The geometric concentration is defined as the ratio of concentrator aperture area to solar cell area. Considering the aperture area of the cells (30.25mm^2 and 30.74mm^2) and the primary lenses area (0.01m^2/cell, 12 cells) gives a ratio of 325-330. Although, as the secondary with good alignment focuses the light into a 16mm^2 square, the concentration ratio becomes 625, which allows some misalignment of the tracker or manufacturing error in the module while still receiving most of the sunlight.
Finally, implementing adequate changes to Eq. (3) the expression used for the estimation of I_{sc} is:

$$\boldsymbol{I_{sc} = A_f \times min\left(\int_{\lambda_i}^{\lambda_f} SR(\lambda)_{sub-cell} . E_{mod}(\lambda) . T_1(\lambda) . T_2(\lambda) . d\lambda\right) \times C_g \times \eta_{op}} \quad (3)$$

where $\boldsymbol{I_{sc}}$ is the short-circuit current in A, $\boldsymbol{A_f}$ the area of light focused on the cells, in m^2, $\boldsymbol{SR(\lambda)_{sub-cell}}$ the spectral response of each sub-cell, in A/W, $\boldsymbol{E_{mod}(\lambda)}$ is the spectral irradiance modelled by SMARTS, in W/m^2/nm, $\boldsymbol{T_1(\lambda)}$ and $\boldsymbol{T_2(\lambda)}$ are the optical transmission functions respectively for the primary and secondary optics, $\boldsymbol{C_g}$ is the geometric concentration ratio, $\boldsymbol{\eta_{op}}$ the efficiency of the optics and $\boldsymbol{\lambda_{i-f}}$ the wavelength range of the spectral response.

2.3. Power Rating

More than determining the energy yield of a module through the simple integration of the generated power over time, it is of interest to understand how this power output varies under clear-sky conditions, which means performing a power rating analysis, so that knowledge on the behaviour of the modules is acquired and further prediction is allowed. However, it is challenging to rate module power under outdoor conditions and achieve consistent results. Flat-plate PV uses indoor simulators specifically to avoid this problem, but the unique designs of CPV present a need to use on-sun measurements [43]. Efforts have been made towards predicting the power generated by both flat-plate and CPV systems as a function of relevant measurements, though, the challenge with an outdoor rating is that conditions that impact the measurement, such as the spectrum, temperature, wind speed, etc.,

are constantly varying; actually, there is still disagreement among the CPV community when it comes to the standards for the power rating methodologies [40].
As a performance testing method needs to solve the trade-off between precision and easiness, the safest way is to conduct one or several years of field test [40]. Here the Concentrator Standard Operating Conditions (CSOC) are introduced, analogous to PV standard reference environment for NOCT measurement, can be found on the IEC 62670 [44]. This conditions are mainly DNI=900Wm^{-2}, Ambient Temperature=20ºC and Wind Speed=2ms^{-1}. A schematic on the various procedures related to the Concentrator Standard Conditions is shown in Figure 20.

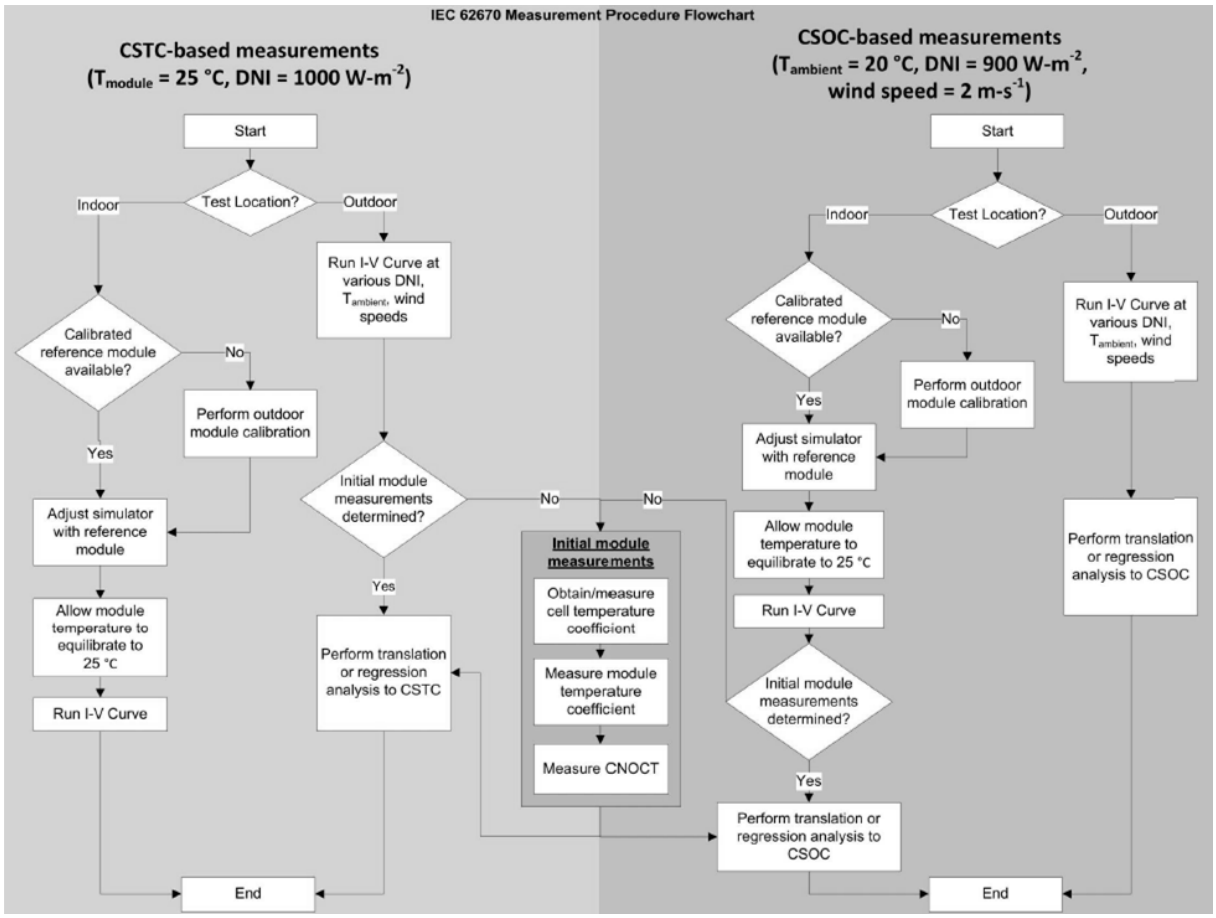

Figure 20 – IEC62670 procedures chart [44]. The CSOC outdoor branch was accessed in this work.

In this assessment, a procedure similar to the one used in [43] was followed. The method is based on collecting solar, meteorological and power output data over a sufficiently long observation period and applying the statistical regression (4) as specified in ASTM E 2527-06.

$$\boldsymbol{P_{max} = DNI(a_1 + a_2 DNI + a_3 T_{ambient} + a_4 Wind)} \quad (4)$$

In order to restrict data to clear-sky CSOC conditions, a baseline filter was also applied to the data that was collected on-site:

- DNI ≥ 750 W/m^{-2};
- DNI / GNI ≥ 0.75;
- 10Cº ≤ Ambient Temperature ≤ 30Cº;
- 5 minute DNI deviation ≤ 2%;
- Instantaneous Wind Speed ≤ 5ms^{-1}.

The above criteria were adapted from [43], with the added DNI / GNI ratio from [14]. This ratio has been included to lessen the possible impact of the circumsolar radiation (CSR) on the current of the modules. The CSR is visible as an enlargement of the solar disc, due to scattering of light, and has great impact when modules have a smaller acceptance angle than that of the pyrheliometer, which

under hazy sky conditions, with a relatively high CSR, will measure a significantly higher DNI than that can be utilized by the modules. Consequently, the current of the modules will be lower than under low CSR conditions [14].
Moreover, in order to have an estimate on the inaccuracy for both approaches, the average error was calculated for every month through Eq.(5).

$$e_{meas-pred} = \frac{\sum|P_{meas} - P_{pred}|}{\sum P_{meas}} \quad (5)$$

where P_{meas} and P_{pred} are the power measured for each module and the power predicted for each module, respectively.
Applying (4) is rather simple, but the coefficients a_1, a_2, a_3 and a_4 often fail to accurately gauge the actual relationship between power and meteorological conditions and are noted to vary substantially between locations with different atmospheric conditions [16]. This issue will be addressed in section 3.4.3.

2.4. Spectral indexes

For CPV power plants with multi-junction solar cells, a common method is to use component cells to study the influence of the spectral conditions on the output current of the module [45]. These monitor cells allow the measurement of direct spectral irradiance [28], by using three cells (or single-junction cells that have the same spectral response as each of the three component cells in the multi-junction stack) with ideally the same spectral responses as the sub-cells in the investigated multi-junction solar cell, one can know which sub-cell is limiting the current whatever the spectral distribution is. However, as monitor cells are not always accessible, to analyse the effect of the spectral irradiance distribution on the outdoor performance of CPV modules, indexes for the spectral distribution are used.
There are a few spectral indexes in the literature, each of them related to certain characteristics of the spectral irradiance and the cells, such as the colour of the spectrum, the spectral dependent interaction of the sub-cells with atmospheric parameters and the values that optimize that interaction. In this section, the most relevant spectral indexes are described.

Average Photon Energy
Firstly, one of the most cited indexes is the Average Photon Energy (APE), which proves to be a useful device-independent environmental parameter for quantifying the average hue of incident spectra [46]. APE is calculated by dividing the integrated irradiance with the integrated photon flux density, as shown in Eq. (6), where $\phi(\lambda)$ is the number of photons per unit area and time and q the elementary charge.

$$APE = \frac{\int_0^{\lambda} E_{mod}(\lambda).d\lambda}{q\int_0^{\lambda} \phi_{inc}(\lambda).d\lambda} \quad (6)$$

Hence, APE relates to the colour of the spectrum (high APE values indicate a spectrum shifted toward the blue, while lower values are correlated to a redder spectrum) and can represent the extent to which a spectrum can shift toward the red or the blue. Its calculation is straightforward since it is a device independent indicator and its uniqueness for the spectra measured in a particular location and climate has been demonstrated [47].
However, special care has to be taken when comparing APE values with different spectral ranges. For instance, the APE for the global reference spectrum is 1.88eV in the range 350 – 1050 nm, while for a spectral range of 350 – 1700 nm is 1.6eV [48]. The values for the direct spectrum are approximately at 1.85eV and 1.56eV, for the spectral ranges quoted above, respectively.

Spectral Mismatch Ratio

An alternative and important index that allows comparison among different spectral distributions is the Spectral Mismatch Ratio (SMR). Following the procedure adopted in [49], SMR can be calculated for the three cells. This ratio is also intended as an instantaneous energy mismatch factor, more appropriate for HCPV [36], which provides a way of describing the relative current mismatch for the reference spectrum. Eq. (7) describes the method for SMR calculation.

$$SMR = \frac{\left(\frac{\int E_{mod}(\lambda).T_1(\lambda).T_2(\lambda).SR_{mid}(\lambda).d\lambda}{\int E_{AM1.5D}(\lambda).T_1(\lambda).T_2(\lambda).SR_{mid}(\lambda).d\lambda}\right)}{\left(\frac{\int E_{mod}(\lambda).T_1(\lambda).T_2(\lambda).SR_{top}(\lambda).d\lambda}{\int E_{AM1.5D}(\lambda).T_1(\lambda).T_2(\lambda).SR_{top}(\lambda).d\lambda}\right)} \quad (7)$$

where $E_{AM1.5D}(\lambda)$ is the direct spectral irradiance of the reference spectrum. The numerator refers to the middle sub-cell current mismatch to the reference spectra and the denominator to the top sub-cell mismatch.

If SMR is greater than 1 then the spectrum at the cell surface is rich for the middle sub-cell (red rich spectrum) in comparison with the reference spectrum. Inversely, if SMR is less than 1 then the spectrum is rich for the top sub-cell (blue rich spectrum) in comparison with the reference spectrum.

As no indoor measurements were performed, $I_{sc,indoor}$, DNI_{indoor} (1000W/m^2) and A_{indoor} refer to the datasheet values for each cell, while I_{sc}, DNI and A_f (16mm^2 light focus on the cell) refer to the simulation. Then, in order to consider the effect of irradiance intensity and slight different cell aperture areas, measured I_{sc} is normalized as it follows:

$$Normalized\ I_{sc} = \frac{I_{sc,model}}{I_{sc}} . \frac{DNI_{indoor}}{DNI} . \frac{A_{indoor}}{A_f} \quad (8)$$

Spectral parameter Z

Since sub-cells of monolithic multi-junction cells are not separately accessible, which presents a challenge to measurement systems and procedures, a different spectral parameter, Z, has been proposed, enabling the spectral mismatch correction for these cells whilst reducing the time required for calibration. [50]. Z describes the current mismatch relative to the current mismatch for a reference spectrum and is a method more robust than the application of spectroradiometers.

The successful application of the method is possible if two main pre-requisites are satisfied. The first requires a set of monitor cells which absolute spectral responses are, in the case of TJ cells, equal to the spectral response of the corresponding sub-cell in the TJ cells contained on the modules under evaluation. In this particular case, two monitor cells are sufficient, because, as mentioned before, only the top and middle sub cells are expected to limit the current. The second pre-requisite relates to the selection of a reference spectrum, for instance the standard AM1.5d (850W/m^2), which is often used as reference for concentrator modules. The monitor cells, then, must be calibrated to this reference spectrum. After the calibration, the monitor cells must be mounted onto the considered outdoor stand and their I_{sc}, as well as the modules' I_{sc}, must be recorded over a sufficiently long period of time, assuring that red and blue-richer spectra than the reference will illuminate the cells.

A spectrometric method is then applied to quantify the spectral impact (see Figure 21). The ratio of measured and calibrated I_{sc} is determined for both monitor cells (R_1, for the monitor cell associated with the top sub-cell, and R_2, associated with the middle one) and plotted in the spectrometric plane with two independent axes, r_1 and r_2.

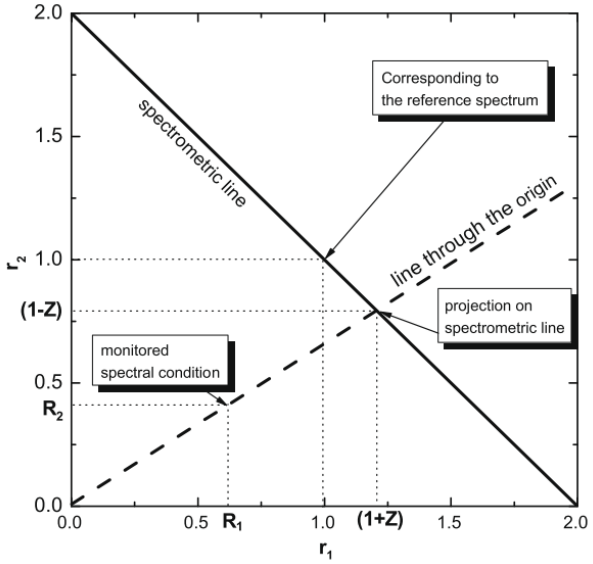

Figure 21 – Spectrometric plane [14]. R_1 and R_2 are the ratio of the current of both monitor cells under the monitored spectrum and the reference spectrum. A $R_1/R_2=1$ line through the origin means spectral distributions that cause the same current mismatch as the reference and the spectrometric line mean $r_1+r_2=2$, allowing the projection of every point into this reference.

Here, a pair of R_1 and R_2 can be generated by an infinite number of spectra. For instance, the point (1;1) in the spectrometric plane, as well as the respective line through the origin, corresponds to spectral conditions that generate the same current mismatch as the reference spectrum. Moreover, below the line $r_1=r_2$ lie the spectra that generate more current in the monitor cell associated with the top sub-cell than in the one associated with the middle sub-cell. The inverse is true for spectra laying above the $r_1=r_2$ line.

The current mismatch of every data point on the spectrometric line ($r_1+r_2=2$, which is of interest because allows direct comparison with the reference spectrum) can be defined by a spectral parameter Z. The calculation of Z involves a projection of every data point into the spectrometric line, in order to normalize the absolute current mismatch of the monitor cells to the reference, see Eq. (9) and (10).

$$\boldsymbol{Z = R_1^y - 1 = \frac{2 \times R_1^x}{R_1^x + R_2^x} - 1} \tag{9}$$

$$\boldsymbol{Z = 1 - R_2^y = 1 - \frac{2 \times R_2^x}{R_1^x + R_2^x}} \tag{10}$$

where $\boldsymbol{x}$ indicates the initial values and $\boldsymbol{y}$ the projected values.

A Z equal to 0 corresponds to the reference AM1.5D, negative values indicate a redder spectrum and positive values a bluer spectrum. The indicator Z, when plotted against I_{sc} recorded for the modules (linearly normalized to 850W/m^2 and filtered to the clear sky conditions formerly described), allow linear correlations between these variables and, furthermore, translations equations can be derived, enabling a module's I_{sc} to be derived for any spectral conditions [14], which was not the aim of the present evaluation.

The presented index is recommended for long-term outdoor investigations of CPV modules and systems, since, usually, many uncontrolled factors influence the data points measured outdoors and, thus, it is advantageous to apply the more robust and simpler method and accept the lower accuracy.

2.5. Experimental Setup

In this section, the system that is explored in this study is described: the two-axis tracking platform, the instruments for I-V curve tracing, the devices for radiation and weather parameters sensing, as well as the mounted modules and respective solar cells. Some considerations regarding the limitations imposed by the instruments and data logging procedures will also be explained along this section. It is to be noted that all procedures related to the operation of the instruments, mainly the spectrometer, were implemented before the beginning of this work and no changes were applied.

2.5.1. Tracker

The site is assembled at the Solar Campus of the Faculty of Science of the University of Lisbon, in Portugal, since June of 2010, at the coordinates: N 38.757660, W 9.156311.
The research tracker (Figure 22) is a 5 m^2 sub-structure of Circadian Solar's 30 m^2 system (CS30) that is at the heart of its product line, allowing easy access to the chassis for rapid changes of development modules, but providing the high tracking accuracy (<0.1°) of the standard product [51].
CPV, like all PV technologies, is most cost effective for sunny regions with clear skies. Although the diffuse light is not effectively captured by CPV, DNI resources are greater than resources available to fixed flat-plate panels in some environments because of the value of tracking [42]. Despite the additional cost of continuous tracking of the sun, CPV can offer a cost advantage over conventional silicon based PC technology in sunbelts regions with high direct sunlight [3].

Figure 22 – Overview of the two-axis tracking platform with several mounted modules. The PC cabinet is also visible further on the back.

The tracking is done by open-loop astronomical calculation; therefore there is no feedback from a sun sensor. The tracker uses rotary encoders to measure its position and, through references on each axis, the tracker finds its position each evening just before it goes to horizontal. These reference positions are used to reset the encoder counts and remove any small errors that have occurred during the day. There is a teaching mode where it is possible to manually line the tracker up to the sun, from which the tracker learns what the positions of the reference sensors are. There is only need to do this teaching once; either using a visual reference or using the power output from one of the modules, which means that the tracker can be taught remotely.
It is to be noted that occasionally other correction for the tilt of the post, which may not be perfectly vertical, has to be done. However, as the tracker has a post that is very close to vertical (less than 0.1°) there was no need to apply such correction.

The tracker moves by induction motors driving a two-axis gearbox (Figure 23, a) controlled by motor inverters and Programmable Logic Controller (PLC) running custom software. It is important that this software knows an accurate time, so that it can get this over Ethernet from the PC in the cabin by Network Time Protocol (NTP).

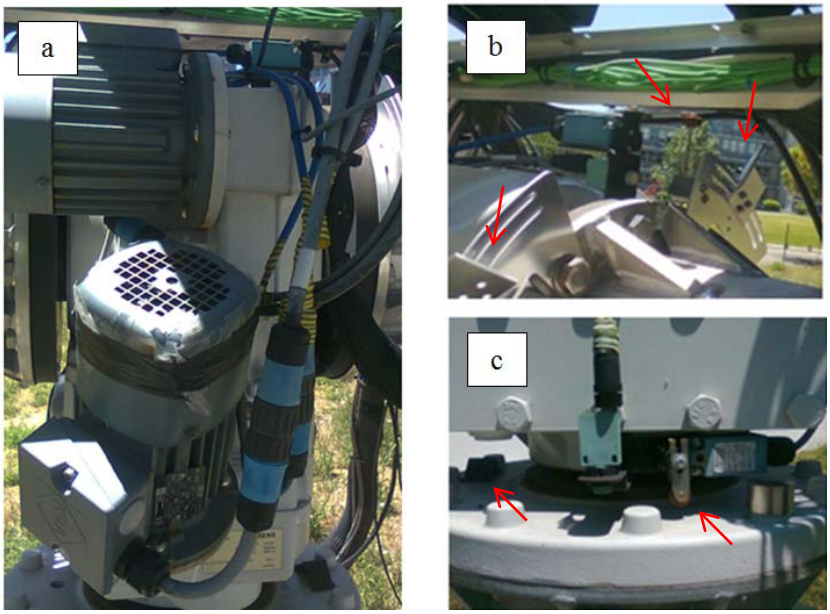

Figure 23 – Chassis detail: a) gearbox, b) vertical axis mechanical switch, c) horizontal axis mechanical switch.

There are also two mechanical switches, one on each axis, in order to prevent the tracker from going too far in case there is a software problem. The vertical (elevation) axis switch (Figure 23, b) is on the top of the gearbox and the horizontal (azimuth) axis switch (Figure 23, c) is located on the top of the main post, where the gearbox attaches to it.

2.5.2. Weather station

Meteorological data is of the greatest importance, not just as input for the radiative transfer model, but also for the performance evaluation. The set of sensors to perform those measurements is composed by: an absolute pressure sensor, an ambient temperature sensor and a relative humidity sensor (Figure 24, a), which are all mounted on the tracker post, and an anemometer on the top of the chassis (Figure 24, b).

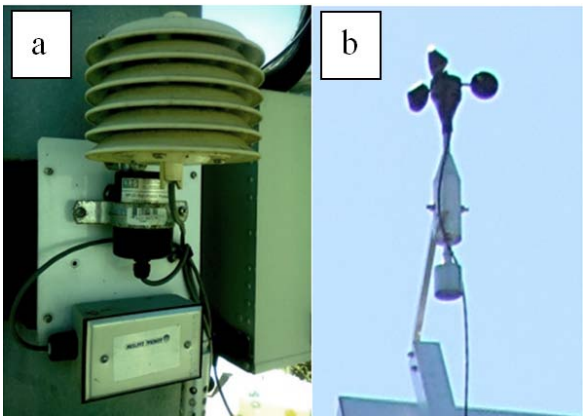

Figure 24 – Sensors for: a) relative humidity (bottom), absolute pressure (middle) and ambient temperature with protection shield (top), b) anemometer. All instruments, but the anemometer, are shaded by the post.

The barometer is an NRG Systems #BP20, the thermometer a NRG #110S with radiation shield, the hygrometer is a NRG Systems RH-5 instrument and the anemometer is a NRG #40C. The relevant specifications of the sensors are listed in Table 2. Measurements for these parameters are performed every minute during day time and every 10 minutes at night time.

Table 2 – Relevant specifications for the sensing devices on the weather station.

Instrument	Parameter	Value and applicable range
Anemometer	Wind speed	1m/s to 96m/s
	Accuracy	± 0.14m/s at 10m/s, Class A ± 0.45m/s at 10m/s, Class B
Barometer	Absolute pressure	15 kPa to 115kPa
	Accuracy	± 1.5kPa
Thermometer	Ambient temperature	-40ºC to 52.5°C
	Accuracy	total error ± 1.1°C
Hygrometer	Relative humidity	0% to 100%
	Accuracy	± 2%, from 10% to 90%, at 25°C ± 3%, from 5% to 10%, at 25°C

2.5.3. Solar Radiation Sensors

Solar radiation sensing has been essential to characterize the resource available for solar applications in general and to validate predictions. After a system is installed, they can be used to supervise its performance. Global normal broadband irradiance is monitored by a pyranometer (Figure 25, a), and the measurement of direct normal broadband irradiance, of the upmost importance for CPV systems, by a pyrheliometer (Figure 25, b); the direct spectral irradiance is monitored by a spectrometer (Figure 25, c).

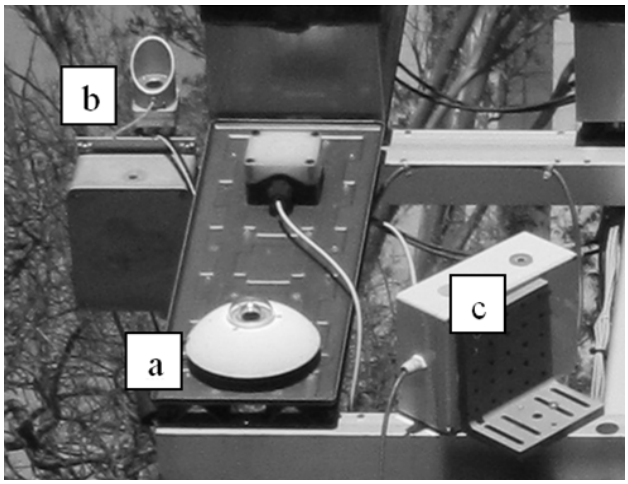

Figure 25 – Pyranometer (a), pyrheliometer (b) and box with spectrometer fibre and filter (c).

Global Normal Irradiance

A SR11 first class pyranometer from Hulseflux is installed to measure the Global Normal Irradiance (GNI), which is the solar radiation flux that is incident on a plane surface from an 180º field of view. Using a thermopile sensor which has an almost flat spectral response in the wavelength range of the solar spectrum [52], the pyranometer generates a small output voltage proportional to the radiation flux. Employing two glass domes, certain measurement errors are reduced, in particular thermal offsets, so that high measurement accuracy is attained. Although GNI is not totally used by CPV modules, but only its direct component, a small part of diffuse radiation may reach the primary lenses. Nevertheless, this would represent a residual portion of the total energy yield. This parameter is

relevant for module efficiency calculation and CSR filtering, as discussed above. GNI measurements are performed every minute at day time and every 10 minutes at night time.

Table 3 - Relevant specifications for the SR11 Hulseflux pyranometer.

Instrument	Parameter	Value and applicable range
Pyranometer	Spectral range	305 to 2800 nm
	Irradiance range	0 to 2000 W/m^2

Direct Normal Irradiance

CPV systems, not effectively capturing diffuse light [42], use the sunlight direct beam, which is often referred to as direct normal irradiance (DNI). Proper design and output prediction of CPV power plants implies that the resource in DNI has to be accurately measured or modelled. High quality DNI measurements are always the preferred method for solar resource assessment and can be achieved with excellent accuracy (±5% or better) with thermopile pyrheliometers [20].

Thermopile pyrheliometers are known to be robust field instruments, of excellent accuracy if properly maintained and daily cleaned, ideal for high-end research and validation of DNI models, have no cosine error [53], but high soiling sensitivity is still a problem. Soiling is strongly dependent on the weather conditions due to factors like the amount of dust in the air (influenced by the nature of the ground around the station), air velocities at the location and humidity or dew on the sensors [54]. For instance, in a study for the establishment of a Concentrating Solar Power (CSP) plant in Namibia [27] within one month without cleaning a signal reduction due to soiling of -25% was registered. No such reduction would be expected to happen with the device mounted on the evaluated system, however, since the surroundings are mainly bush cover, the occasional cut may spread soiling agents through the air. Seasonal raining may also contribute to some soiling of the sensors, particularly of this type.

In the tracker, a first class DR01 Hulseflux pyrheliometer, with a quartz window/lens, for true spectral solar transmission ranging from 200 to 4000 nm is mounted. This device employs a passive thermopile-based sensing technology that generates a low level output voltage signal, proportional to the normal incident direct solar flux received at the detector surface. A feature on a thermally isolated low power window/lens heater in the foreoptic (the lightweight fibre optic cable) is also included, which makes it possible to effectively eliminate the formation of dew on the pyrheliometer window/lens, thus resulting in improved post sunrise early morning measurement accuracy. DNI measurements are performed every minute at day time and every 10 minutes at night time.

Table 4 - Relevant specifications for the DR01 Hulseflux pyrheliometer.

Instrument	Parameter	Value and applicable range
Pyrheliometer	Spectral range	200 to 4000 nm
	Full opening view angle	± 2.5º
	Irradiance range	0 to 2000 W/m^2

As the pyrheliometer covers the entirely wavelength range of sunlight, it will be possible to make direct comparison between measured DNI and the integration of the modelled spectral irradiance, that is computed between 280-2500nm, since only 3.7% of the irradiance lies in wavelengths outside this interval [17] [54].

Direct Spectral Irradiance

Over the last decades, the high sensitivity of multi-junction solar cell's performance to the spectral content of the sunlight, due to their current limiting behaviour, has been the focus of many studies, for example [12][13][14][15]. The assessment of spectral distribution over the wavelength is the most important step, not only to predict and characterize the performance of CPV modules, but, first of all, to know if a location is even worth of a pre-study for a certain cell technology. As mentioned earlier, in spite of few disadvantages, spectroradiometers are the proper instruments to perform this type of

measurement. There are fast single-grating spectroradiometers (also known as polychromators), with integration and spectrum acquisition times ranging from 10 to 600ms, and multi-grating single monochromator spectroradiometers, with a full spectrum acquisition time of approximately 4 min [55].
The available device for spectral irradiance measurement mounted on the tracker is, unfortunately, a spectrometer that only measures relative intensity, contrarily to spectroradiometers, that are calibrated to measure quantitative or absolute intensity at different wavelengths of the electromagnetic spectrum. This instrument is an Ocean Optics Jaz spectrometer (Figure 26), built on a platform that expands to include a light source. It can be controlled by a software interface from the manufacturer called SpectraSuite. However for measurement automation, a software in Microsoft Visual Studio, was developed and implemented by Circadian. Spectral measurements data acquisition was performed, whenever it was possible, every 5 minutes at day time.

Figure 26 – Jaz spectrometer inside the instruments cabinet on the chassis. The optical fiber (blue) that attaches to the device is also visible.

Table 5 - Relevant specifications for the Jaz Ocean Optics spectrometer.

Instrument	Parameter	Value and applicable range
Spectrometer	Spectral range	200 to 1100 nm
	Fibre aperture	400micron (diameter)
	Acceptance angle	± 0.5º (with circular collimator)
	Saturation	65000 counts

This instrument is very sensitive when it comes to the intensity of the incoming light (see Table 5) and temperature. Hence, to make it able to carry out measurements on the direct beam, a strong optical filter had to be added to the entrance of the optical fibre, which is attached to a circular collimator inside the box (see Figure 25, c). Outside the fibre box, a quartz window serves as protection for the reflective neutral density ND530B filter from Thorlabs (see Figure 27).

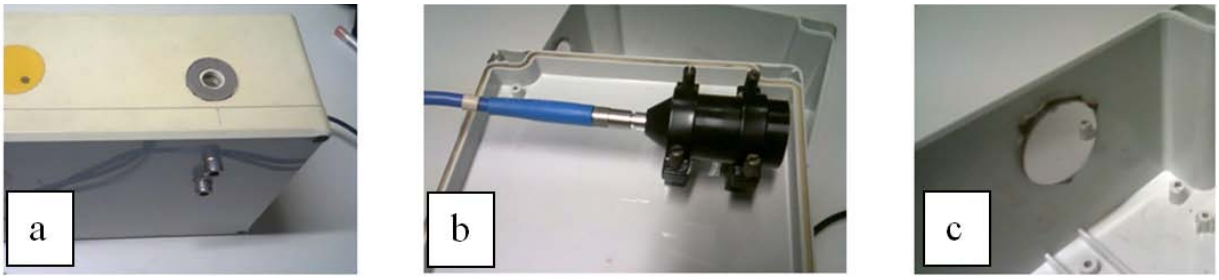

Figure 27 – Spectrometer fibre box detail: a) quartz window, b) optical fibre connected to the circular collimator and c) reflective neutral density filter.

The coating of the filter is made out of Inconel, a metal composite. According to the manufacturer, no remarkable changes in transmission are expected to at least 100°C, however, no data on the transmittance dependency on temperature is available. The only data available on the optical transmittance of the neutral density filter and quartz window is the one given by the manufacturer (see Figure 28).

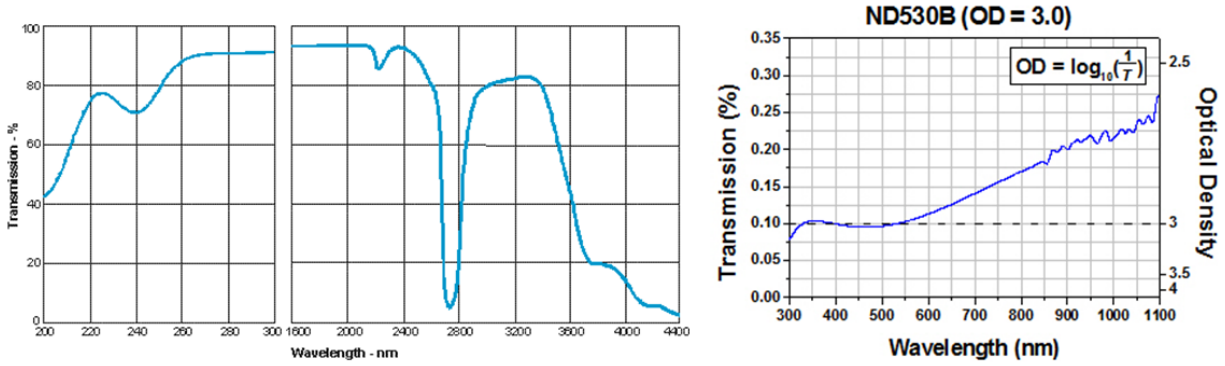

a) b)

Figure 28 – Optical transmission of fused quartz window (a) and reflective neutral density filter (b).

On the other hand, as the quartz window has been continuously exposed to weather agents and sunlight, as well as the filter, it may not still be correct to employ the typical transmittance information in further calculations. To verify this, the spectrometer was removed from the tracker and the transmission was measured in laboratory. Then the spectral data measured by the spectrometer was accessed using both typical and measured optical transmittance in effort to find any agreement with the shape and values of the modelled spectra. This will be further discussed in section 3.1.
The device was removed on a clear sky day, the 24th of May, at a time close to solar noon. With a thermocouple sensor, the temperatures of several parts of the spectrometer were measured to determine if thermal effects could be significant. In fact, the highest temperature of 45 ± 1 ºC was detected on the quartz window and the lowest temperature of 27 ± 1 ºC on the surface of the spectrometer itself and in the optical fibre. For this reason, one can expect that the on-field performance of the instrument has not been affected by temperature.
Once in the laboratory, the fibre box was placed so that the entrance for the fibre stayed close to the level of an halogen lamp, which has an emission spectrum similar to the solar spectrum. Using SpectraSuite software, the raw output of the spectrometer, i.e. the counts, were measured. First, with the filter and quartz window (Figure 29) and an integration time of 1000ms. Then, without quartz and filter, using only one side of the box, the one where the collimator attaches. As the fibre immediately saturates without the filter protection, the integration time had to be changed to 10ms.

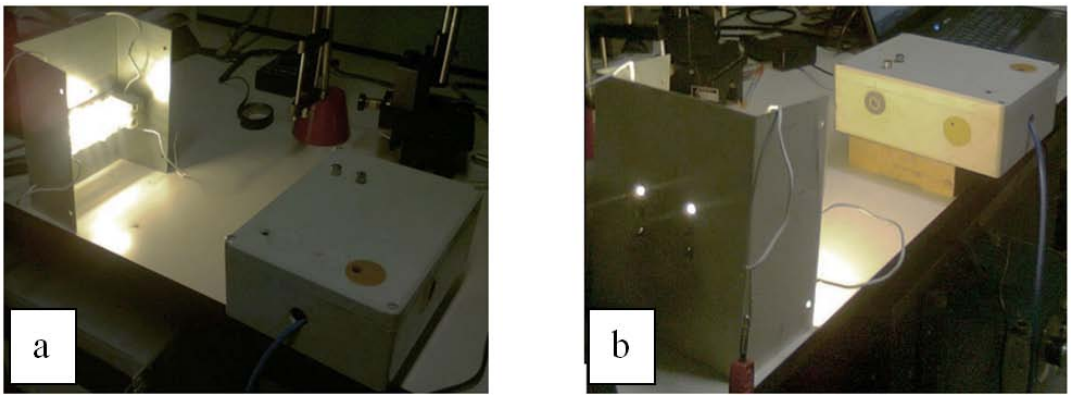

Figure 29 – Detail of the measurement of the optical transmittance for the quartz window and filter.

All lights but the halogen lamp were off during the measurements. The intensity of the lamp remained constant for both attempts. A major limitation of this procedure is the fact that it was not possible to

hold the position of the fibre between measurements. The counts registered for each situation are shown in Figure 30.

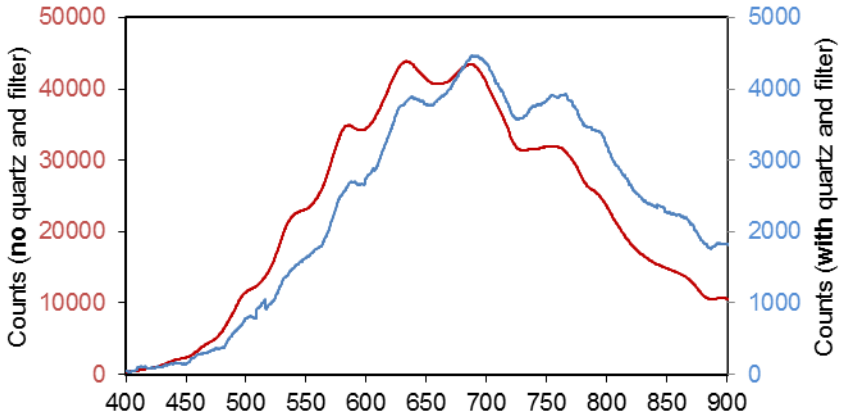

Figure 30 – Raw output of the spectrometer for both measurements with (blue) and without (red) fiber protection.

The transmittance of the protecting elements is then obtained through the ratio between the blue line and the red one, weighted by the corresponding integrating times. Results for this section will be presented and discussed in section 3.1.

2.5.4. Modules and Cells

Modules are monitored for various reasons, such as modelling/performance analysis, to improve their design, to test the reliability [56], etc., which is the case with the Circadian modules assembled on the site. These prototype modules were installed between March and April of 2011.
There are 5 modules of 12 cells each being monitored, which are the same apart from the cells they use. The cells are all lattice-matched with Ge substrate and practically the same size: cells C have an aperture area of 0.308 cm^2, while cells A and B have 0.3025 cm^2. Modules RD11-04 and RD11-05 have B type cells, RD11-06 and RD11-07 have A type cells and RD11-21 has C type cells (see Figure 31).

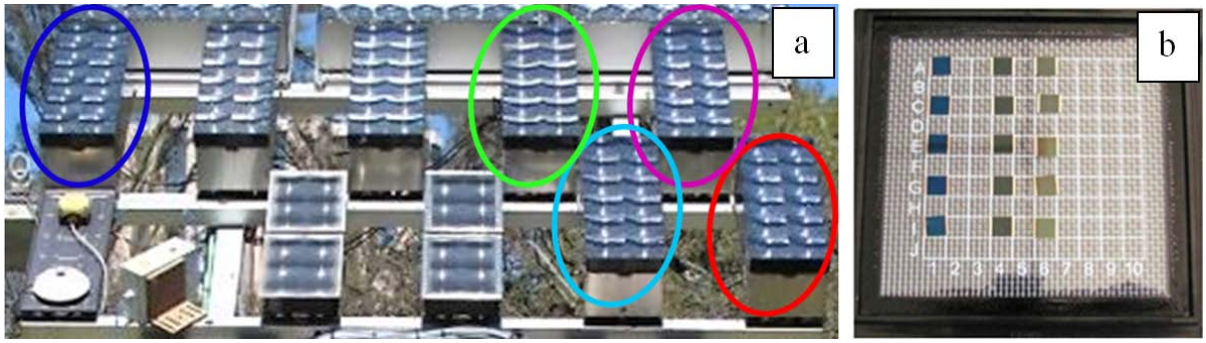

Figure 31 – a) Modules under analysis: RD11-04 (pink), RD11-05 (red), RD11-06 (dark blue), RD11-07 (light blue) and RD11-21 (green).
b) Cells B (column 1), cells A (column 4) and cells C (column 6).

The modules have 12 receivers in series with dome shaped optics, whose properties were described previously. The cells are bonded to a PCB (Printed Circuit Board) receiver, which is then bonded to an aluminium baseplate with heat sink fins (Figure 32) that act as passive cooling.
It is of interest to mention that in the same day that the spectrometer was removed, temperature measurements on some parts of the modules were also performed, having been registered up to 50 ± 1ºC on the heat sink fins and 32 ± 1ºC on the top of the primary lens. Thus, one expects the operating

temperature of the cell to be around 70ºC, i.e. approximately 20ºC above the heat sink temperature and 40ºC above ambient temperature, as determined in other assessments [57][58].

Figure 32 – Back view of the modules on the tracker chassis.

The quality of the cells is assured by Circadian through checking the IV curves visually to see if there is no evidence of a significant shunt or series resistance, which would cause a drop in efficiency. The series and shunt resistance of the cells are features that cannot be changed since these are standard parts from cell manufacturers who must already optimise to get high efficiency. Then, the interconnections within the module and outside the module are made as low series resistance and high shunt resistance as it is practical. On the other hand, before a module is built, all the receivers' dark I-V and flashed light I-V curves are measured, so that any problems with series or shunt resistance will cause a reject.

2.5.5. I-V Curve tracer

The I-V characteristic of the modules is traced by a Keithley Source-Measure Unit (SMU) and controlled by a PC running a Microsoft Visual Studio data acquisition program. The measurement also uses a Hoercherl-Hackl NL1V100C2 source-sink electronic load, with some extra custom electronics to switch the polarity and allow positive and negative voltages, to perform the I-V sweep.
Cells are more efficient at lower temperatures, as they generate higher voltages, hence, the software tries to keep the module at maximum power (P_{mp}) for some time and the measurement is taken at the end of this period. The software takes one measurement every minute and the I-V sweep happens first which takes about 15 seconds. Therefore, the P_{mp} tracking period is about 45 seconds. The purpose of this is to try to measure the module under the conditions that it would have if connected to an inverter.
Since some of the sun's energy is removed as electricity when at P_{mp} (which in this case goes to heating up the cabin), the cells will be maybe 11-12 °C cooler than when they are under open-circuit conditions, depending, of course, on weather parameters, and, therefore, they have a slightly higher V_{oc}, P_{mp} and efficiency. A period of 45 seconds is probably not enough for the modules to completely cool, due to thermal inertia of the aluminium of the baseplate. On the other hand, at 45 seconds, the cells are maybe 9-10 °C cooler, so are still a few degrees hotter than if left for a long time at P_{mp}. However, a compromise between the cooling and measuring the modules often enough had to be made, so this still gives good results.
Although this work only focuses on 5 modules, there are 13 modules on the tracker, so each one is measured every 13 minutes. A multiplexer (Figure 33) on the tracker switches which module is being measured using solid state relays. The system uses a four-wire measurement up to the module to eliminate voltage drops along the cables. But, due to how the electronic load works, in fact there are still residual resistances.

Figure 33 – Multiplexer and datalogger inside the instruments cabinet on the chassis.

2.5.6. Datalogging

The system generates one text file for each module measurement containing the current-voltage points for the sweep and the measured parameters of short circuit current, open circuit voltage, fill factor, maximum power for sweep and P_{mp} tracking, current and voltage at maximum power (for both sweep and P_{mp} tracking). Every few minutes these files are uploaded to Circadian's server to be entered in to an SQL database and then the files are deleted. Text files are also generated for weather measurements, temperature, humidity, pressure, wind speed, DNI and GNI every minute during the day and less frequently at night. Text files are also generated for spectrometer data, but those stay on the PC in Lisbon. The reference time is always winter time UTC/GMT.
Ethernet access is provided both for remote control of the tracker from Circadian's headquarters and for transmission of data for performance monitoring and immediate analysis. However, loss of communication with the PC in Lisbon may occur, as well as power going suddenly off due to overcharge in the cabin, which causes missing measurements and loss of data. When this happens, an email from UPS is sent to Circadian before it shuts the PC down. Then, either it turns on again by itself or needs to be turned on again manually.

3. Results and Discussion

In this chapter, the results from each step described in the methodology presented in chapter 2 will be analysed and discussed. A section on the characterization of the solar spectrum, based on several spectral indexes, is also presented.

3.1. Modelled Spectra Validation

Direct normal spectra were modelled with SMARTS2 for every day from the 1st of July of 2012 to 30th of June of 2013, except for days with either no aerosol data, from both Cabo da Roca and Évora, or no weather measurements. This solar spectrum simulation covers from 6am to 20pm, with a time step of 5 minutes, in attempt to match the spectra measured on-site and allow direct comparison. Such a relatively long time scale may not be a problem since only clear sky conditions are considered for the model and no rapid variations in the atmosphere are expected on such days.
On the other hand, as solar concentrating collectors have apertures that can be significantly less than the acceptance angles of pyrheliometers, especially for technologies with high concentration factors, methods for calculating DNI for small aperture are required [59]. In that case, DNI needs to be obtained by modelling, which brings the whole issue of evaluating the accuracy of DNI model predictions and validating them against reference measurements [20], the same filter for clear sky conditions described in Section 2.3 was employed to select both measured and modelled DNI and perform a comparison (see the example of Figure 34). Here the modelled DNI is obtained calculating the trapezoidal integral of the spectral irradiance simulated with SMARTS2.

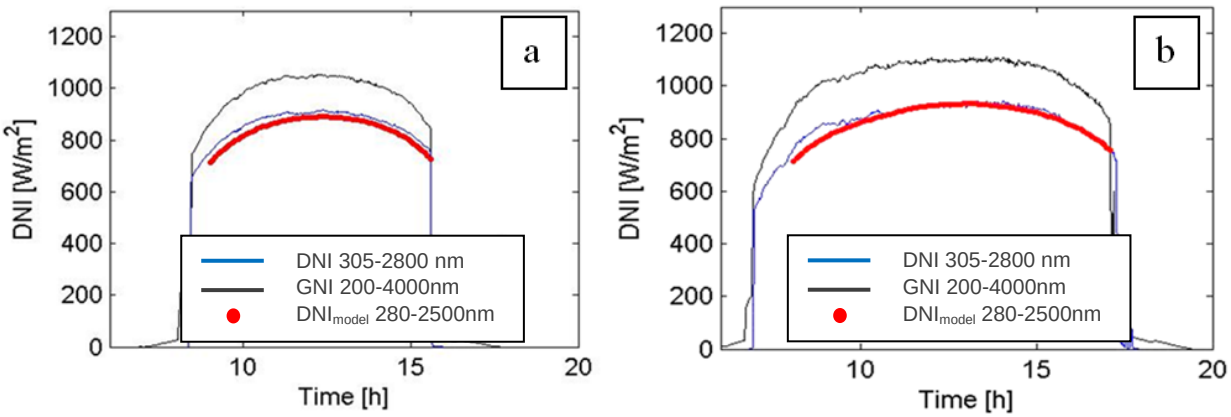

Figure 34 – Measured GNI (black) and DNI (blue) and the integral of modelled spectra (red) for the respective clear sky moments for the study cases of the: a) 12th of November of 2012 and b) 17th of April of 2013.

Fortunately, the direct beam only reaches the tracker when DNI, according to the pyrheliometer, is almost over 600W/m^2, which means that for clear sky days not many measured DNI is left out by the clear sky filter. Therefore, one may also consider, as first approximation, that the modelled DNI is correct if, at least, greater than this value.
In Figure 35, it can be verified that the measured and modelled DNI is inside an interval of ±100W/m^2 (with a slightly higher amount of underestimation) which is reasonable according to simulations and DNI validation done in [16]. Therefore, the simulations are validated, regardless of some source of inaccuracy on the spectral content, due to the absence of on-site sampling of several essential parameters, as already discussed in 2.1.1.

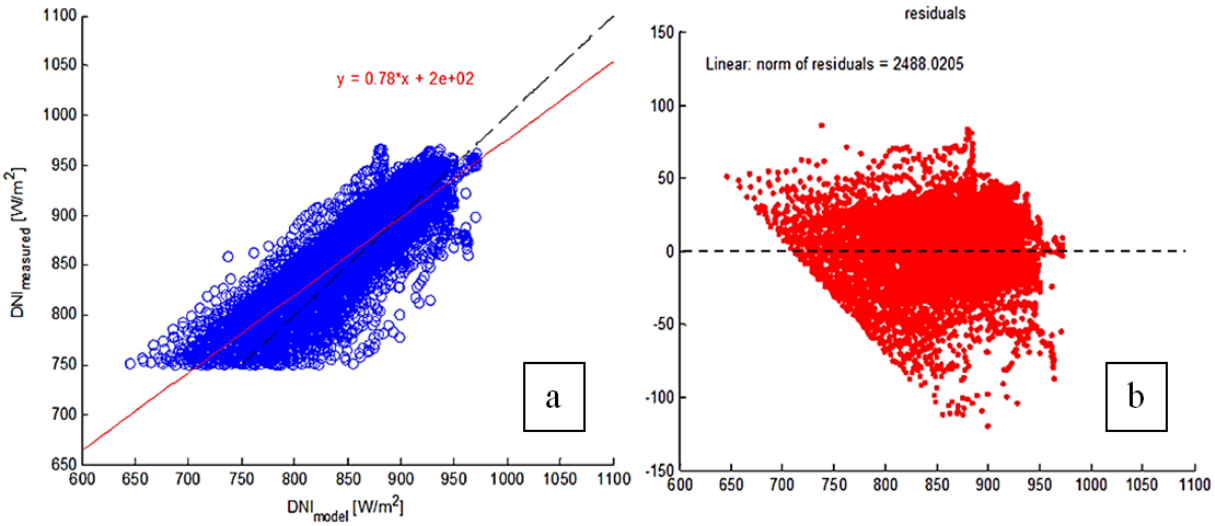

Figure 35 – Plots of: a) measured DNI vs modelled DNI (blue rings) after clear sky filtering, 1:1 relationship (black dashed line), linear fit (red solid line) and b) residuals of the linear fit (red dots).

Having validated the integral of the spectral simulations, it becomes possible to evaluate the measured spectra. However, the spectrometer reveals several operating problems, besides the lack of accurate optical transmission data, as mentioned previously, which may make difficult the validation of the spectral simulations. The first one relates to the software that occasionally crashed and caused the loss of a few spectra over the day. The second problem is that the ultraviolet and infra-red ends of the spectrum had very high counts which saturated the detector most of the time. For this purpose, the spectra measured by the spectrometer will only be referred to in the wavelength range from 400 to 900nm. An example of the measured spectra sampled over two of the study cases is presented below.

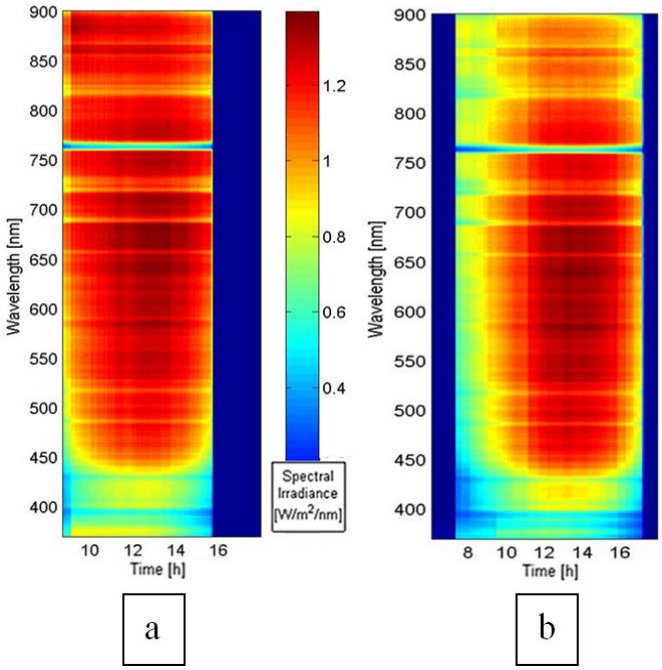

Figure 36 – Daily measured spectral irradiance for the study cases of the: a) 12th of November of 2012 and b) 17th of April of 2013.

The greatest issue relates to the shape of the spectral irradiance which does not agree with the modelled. This effect is clearly seen in Figure 37. This kind of discrepancy has been seen in all spectral data measured on-site throughout the evaluated period, being worse in the first months of the sampling (perhaps a systematic error due to defective positioning caused by strong winds) and in the

afternoons (for instance, Figure 36,a) has higher intensities in the near IR range than Figure 36,b). In Figure 37, morning and afternoon near AM 1.5 spectra for the study case of the 17th of April was accessed, modelled and then plotted with the AM1.5D standard reference [35] for direct comparison.

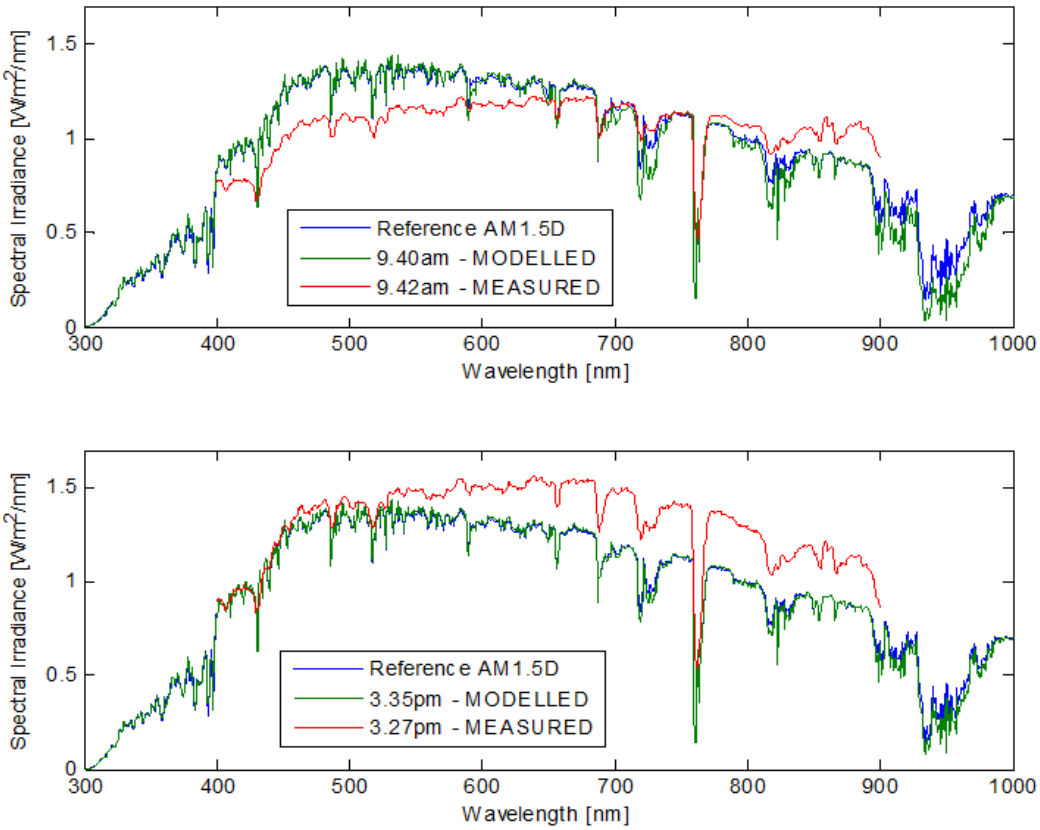

Figure 37 – Both measured and modelled morning (top graph) and afternoon (bottom graph) AM 1.5 spectra for the study case of the 17th of April, with the AM1.5D reference spectrum in background.

Before the spectrum is written into the text a file, the correction of the spectrum for the calibration of the spectrometer is internally applied, as well as a normalization of the integrated irradiance to DNI, which means that the correction for the filter and quartz window have to be applied at a later stage. Hence, the calibration procedure ought to take into consideration the effect of the quartz window and the filter. Therefore, their transmittance measured indoors was analysed. The experimental results are shown in Figure 38.

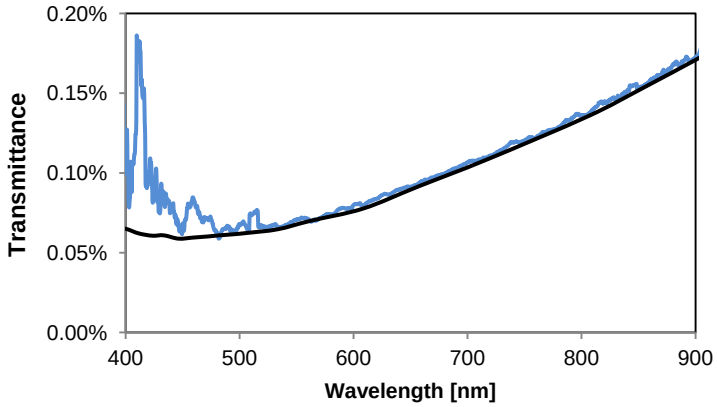

Figure 38 – Optical transmission curve for the quartz window and filter measured indoors (blue) and smoothed curve (black).

This curve contained a significant amount of noise around the 400nm which had to be smoothed, but is not expected to represent a significant of error, since the great disagreement is mainly the excessive intensities of the measured spectra after 550nm. In Figure 39, both measured and original transference curves are compared.

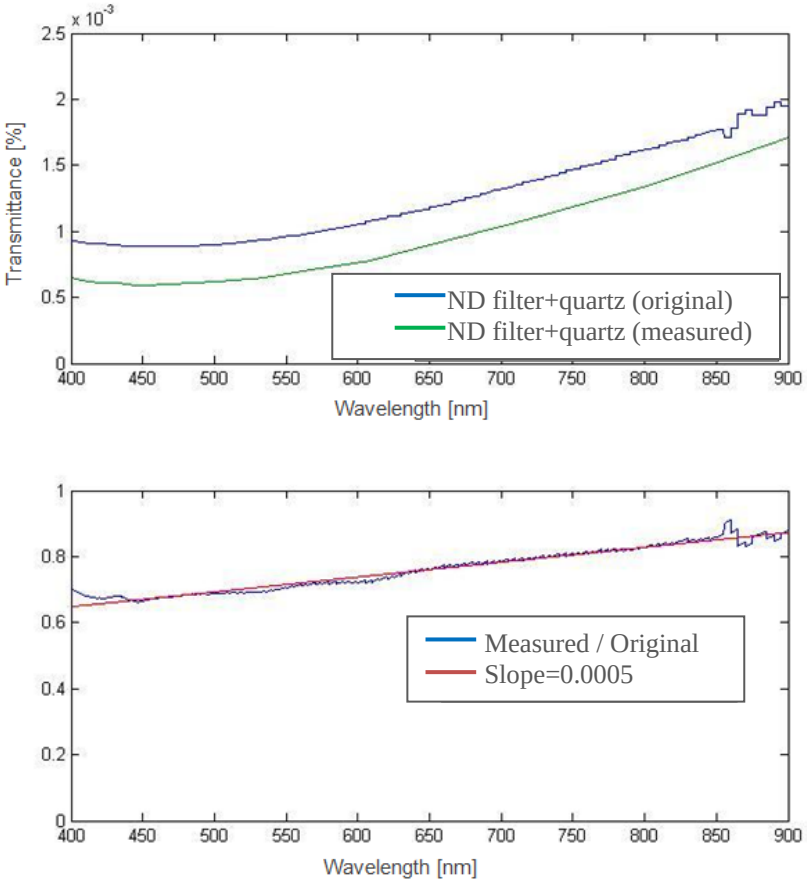

Figure 39 – Transmittance curves for the quartz window and filter: top) original (blue) and measured transference curve (green), bottom) ratio between both curves (blue) and slope of a linear fit (red)

Two main features are apparent. The first is that the filter and quartz window are currently not letting as much light as thought to reach the fibre, since the measured values are below the original transference curve. The second relates to a variation of nearly 20% in the ratio between both curves in the range of 550 to 900nm, which means that currently not just less light is reaching the fibre, but also the near IR region is less affected than the visible (blue) region. This may be due to several reasons, such as some soiling accumulated between the quartz window and the filter, as well as eventual scratching of the quartz surface, which may have more impact on visible irradiance than in the infrared. However, besides the material wear, these do not seem to be very plausible explanations since the device has not been exposed long enough and, for instance, hail episodes are rare; possibly, the filter suffered considerable degradation due to earlier exposure to UV radiation.
The comparison between spectral irradiance corrected using both curves is shown in Figure 40 for the two days, close to solar noon: graphs A and B are relative to the original transference curve, C and D are obtained using the measured curve.

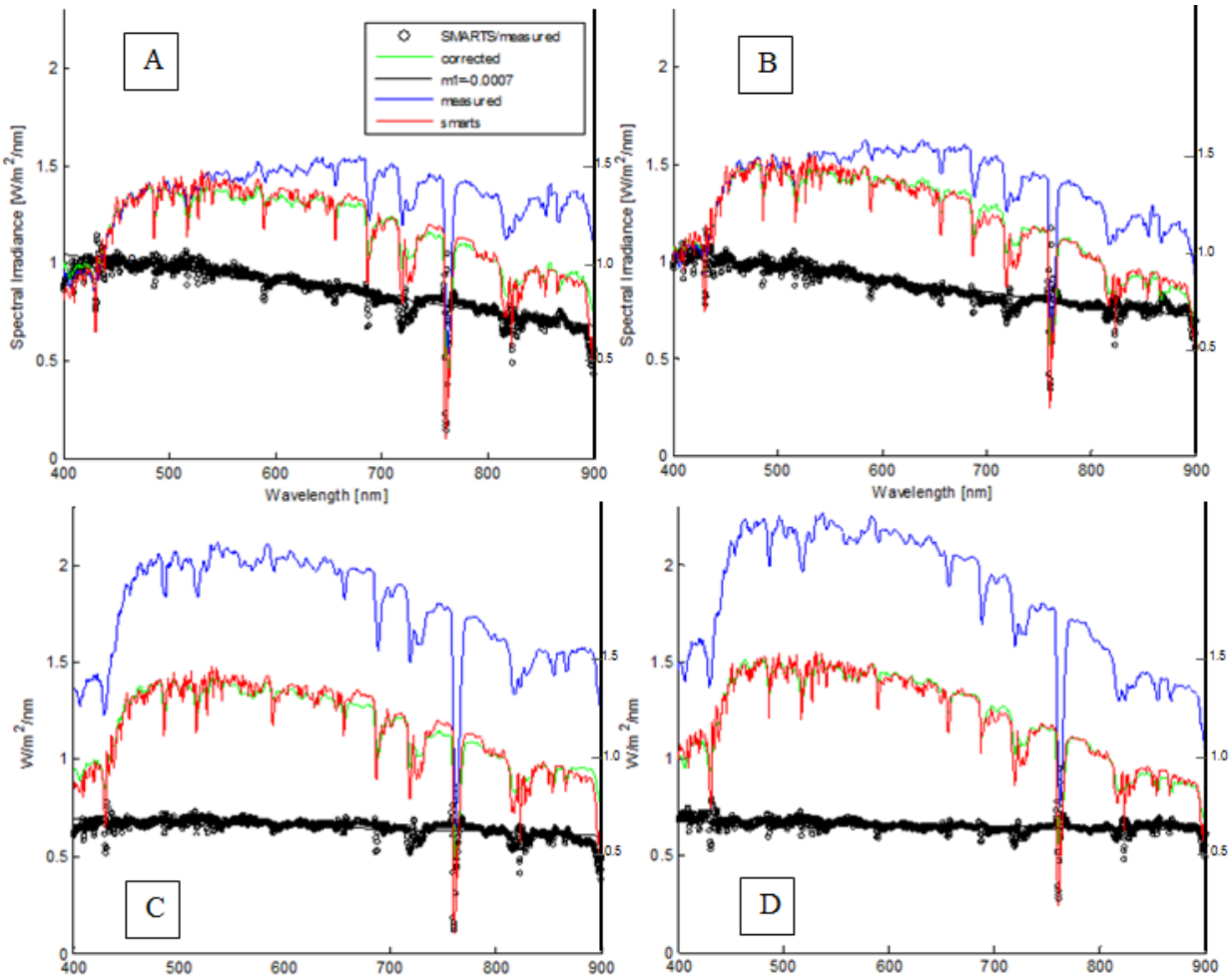

Figure 40 – Measured spectral irradiance (blue), modelled spectral irradiance (red), ratio between the blue and red curves (black dots, secondary axis) and linear fit (black lines, secondary axis), measured spectral irradiance corrected for the right absolute value (green). Plot A and C are for 12th of November of 2012, plots B and D are for 17th of April of 2013. All plots are relative to time close to solar noon. Plots A and B use original transference curve and plots C and D using the measured data.

The measured irradiances (blue) that consider the original transmittance (Figure 40, A and B) reveal a certain tendency to be shifted up and down of the modelled irradiance (red) at 500-550nm. Thus, a linear fit of the ratio between both curves was calculated (not considering the ranges where the main absorption bands are, so that the fit could be more accurate). The fit allows a reasonable correction of the absolute value of the measured irradiance (green). The slopes are similar in A and B (m=0.0007 nm^{-1}) as well as in C and D (m=0.001 nm^{-1}).

Figure 40 shows that with the measured optical transmittance (Figure 40, C and D), the shape of the spectral irradiance gets closer to the expected, with no need for the correction applying the linear fit. However, there is still some source of systematic error, since the absolute values are now too high. The inner DNI normalization may not be to blame because the DNI from the model is closer to the DNI from the pyrheliometer.

Notice that in spite of the fact that the spectrometer assembly to the tracker is not very robust, and therefore it can be sensitive to strong winds, no considerations regarding misalignment were made, since this would cause a down shift of the spectral irradiance, contrarily to what is seen in Figure 40, C and D, instead of changes in its shape. To reach a definitive conclusion, a more precise transmittance measurement would be required, as well as the recalibration of the spectral instrument, including, if that is the case, a more exact DNI normalization. Of course, an alternative would be the use of a spectroradiometer for absolute measurement of the spectral irradiance.

Hence, as the measured spectral irradiance revealed itself unreliable, from now on, the modelled spectral irradiance is used instead. Considering the comparison with the Pyrheliometer data, shown in Fig. 34, we expect that these spectra will be underestimating the total irradiation on the solar cells.

3.2. Short-circuit Current Validation

To model the short-circuit current of the three cells, Eq. (3) is used with the assumptions described in 2.1 and 2.2. As previously explained, the results here presented are only for clear sky instants. In Figure 41, the simulated I_{sc} is plotted against the I_{sc} sampled by the I-V curve tracer, for two of the study cases.

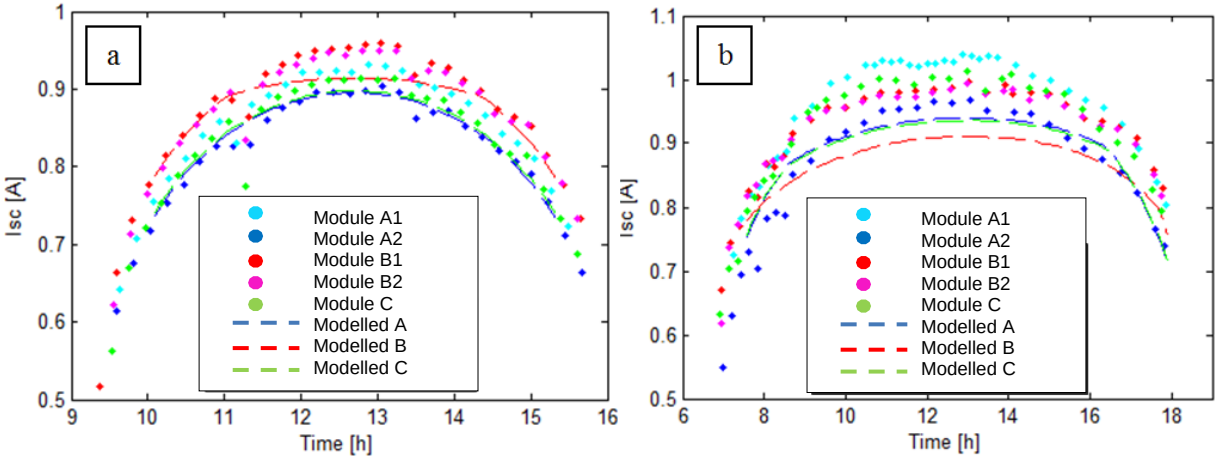

Figure 41 – Measured and modelled I_{sc} for evaluated modules for the: a) 4th of January of 2013 and b) 15th of June of 2013.

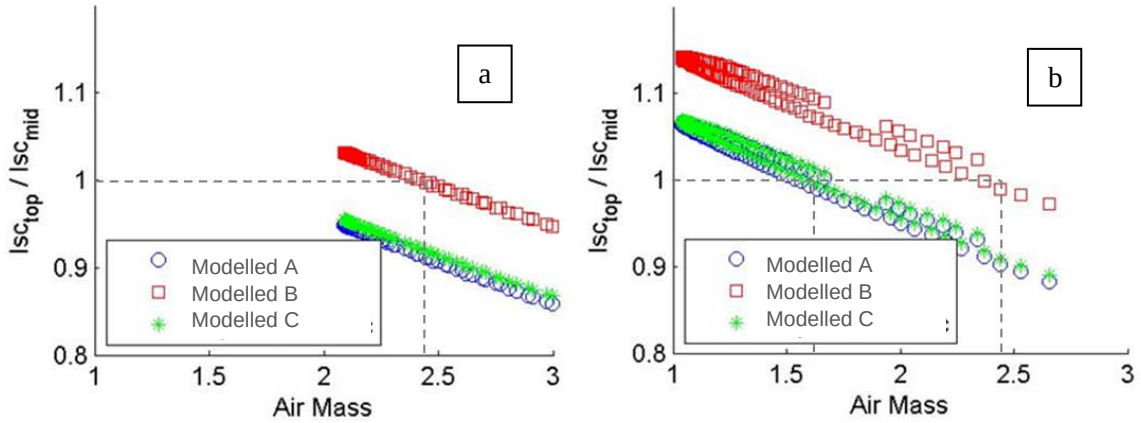

Figure 42 – Ratio between calculated I_{sc} for top junction and middle junction against AM for the: a) 4th of January of 2013 and b) 15th of June of 2013. Grey dashed line marks the current-match.

Observing Figure 41, in January cells B have the highest I_{sc} throughout the whole day. Contrarily, in June, this is found only during the earlier and later hours with DNI. This may be understood taking the spectral response of each cell into account and considering the results presented in Figure 42. Under the various daily spectra, the highest current output for the three-junction cells is obtained at current match, i.e. when I_{top}/I_{middle} equals one [39]. As shown in Figure 42 (plotting the ratio between the I_{sc} calculated for both top and middle junctions against AM), air masses do not go below 2 in winter and cells B are expected to reach current match under such conditions. As these cells are limited by the middle junction for lower AM, cells B perform better with high AM values. On the other hand, cells A and C seem to be optimized for AM close to 1.5.

These results show that, for those days, the simulations have an error of ±10%, which is comparable to, for example, the 6% systematic difference reported in [55], where I_{sc} was determined through spectral irradiance measured by spectroradiometers. Likewise, the examination of all clear sky days during the period of evaluation revealed errors within the ±10% range as well. Therefore, the I-V curve samplings are considered validated.

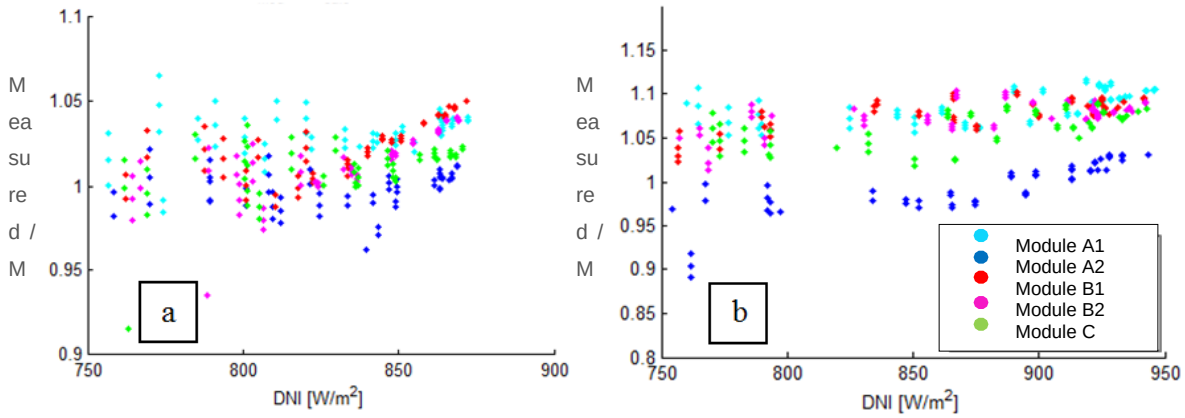

Figure 43 - Ratio between the measured and the modelled I_{sc} is presented against measured DNI: a) for the 4th of January of 2013 and b) for the 15th of June of 2013.

Figure 43 (plots A and B) show the variation of the relative error between modelled and measured I_{sc} as a function of DNI. It shows that for most cells, the model is underestimating the I_{sc}, and that the error seems to increase slightly with the DNI. As the error in modelled DNI is about ±100W/m^2, with a slight tendency to underestimation, it is apparent that some spectral content is missing, which could somewhat explain the underestimation in the I_{sc} simulation. Such limitations in the spectral distribution simulations are perhaps also related to AOD, since this parameter has effect at a great extent of the solar spectrum (from 300 to 1200 nm as shown in Figure 6) and on-site data are unavailable. AOD was extrapolated from the average of two distant locations, regardless of short-term variations that may impact the spectra differently throughout the day. The importance of AOD in CPV simulations is highlighted in [18].

The impact of the DNI on the accuracy of the simulations could also be partly explained by thermal effects. If for a mono-junction solar cell, the current increases (slightly) with temperature, in a MJ solar cell the effect of temperature variations may be the mismatch between the current from the middle and top cells, leading to lower output current, discarding this hypothesis since underestimation is verified. Further second order thermal effects may be related to the temperature dependence of the transmittance of the optical system, which is not taken into consideration by the simulations.

On the other hand, it should be emphasized that the spectral responses of the solar cells are specified for uniform irradiation (and temperature) distributions. This is naturally not verified in the experimental setup and lateral currents (hence current loss) are expected from regions with higher illumination to regions with lower illumination. This effect, which may reach a 10% decrease in efficiency for TJ solar cells [60], would explain the decrease of measured current with respect to the model current, but unfortunately the contrary is shown, excluding this option too.

A systematic error is also observed to high DNI. As it is unrelated to non-uniformity of irradiance, perhaps the temperature coefficients of the cells (1.6mA/ºC for cells A and 3.2mA/ºC for cells B) could explain such dissimilarities until a certain extent. Although, if the passive cooling is efficient, the slight increase in I_{sc} will not be relevant.

One final note on the differences in the short-circuit current for identical modules. For a given module, with cells from a given manufacturer, the simulation results are obviously the same, calculated including one optical transference curve and one solar cell spectral response (measured for a reference temperature and concentration). The experimental results however show more variability among each other than with regard the simulation results. Hence, we may be lead to consider that the inaccuracy of the simulations may also be attributed to variability of the spectral response of the particular solar cells or other assembly factors, such as alignment, electrical connections, etc, which have not been explored. Further analysis regarding the consistency among the same manufacturer may be done using electroluminescence (EL) measurements performed in Cyprus (Appendix, Figure 61), at voltage of 2.7V and at current of 10mA. There is agreement in B type cell modules' consistency and efficiency of its QD technology in the middle sub-cell, whereas for A and C type the results are inconclusive, in spite of some variability reported for cells C.

3.3. Spectral Characterization

The results of the calculation of the spectral indexes described in 2.4 are presented below. As some of the pre-requisites could not be met, some variables were simulated and the same clear sky filter described in 2.3 was employed.

3.3.1. Average Photon Energy

Considering the validation of the spectral simulations, APE variation was computed for the ranges 350-1050nm and 350-1700nm (see Figure 44).

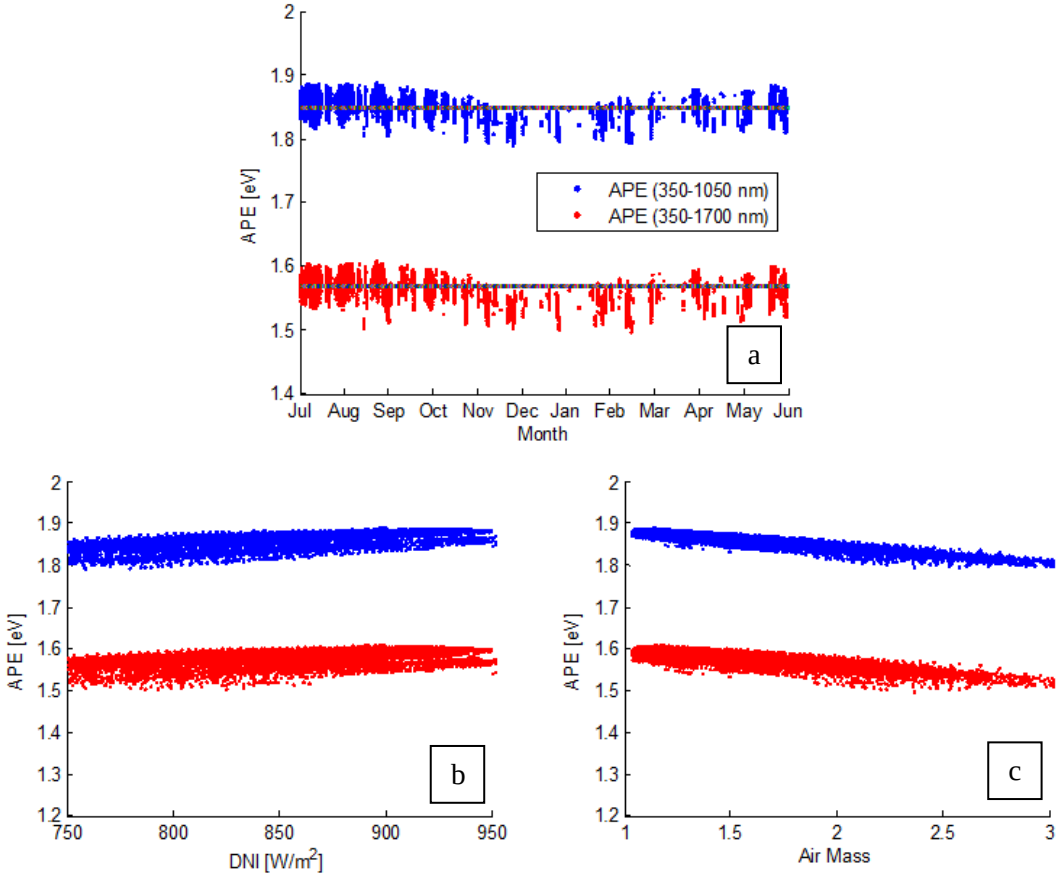

Figure 44 – APE calculated for clear sky moments in the period of evaluation: a) yearly variation of APE, b) APE vs AM and c) APE vs DNI. Grey dashed line marks the ASTM G173 reference spectrum.

The air mass effect on the spectral variation can clearly be observed, as winter spectra appears more rich in the high wavelengths, lower values of APE (Figure 44). Besides, and as expected, low air masses and/or high DNI values are associated to bluer spectra.

It is interesting to notice that the AM1.5d reference spectrum is seldom met during the winter, revealing a redder spectrum, mainly because AM is never less than 2. In spite of the worldwide direct spectra are statistically more red-rich than the reference spectrum ASTM G173 [15], during the summer the site spectra are much more energetic than the reference. In fact, AOD is often smaller than the value used in the reference (0.084), as can be seen in the example of Figure 12 and in Figure 13 there is less scattering in low AOD values.

Still it is important to remind that, as the spectral simulation is not perfect, these APE values may be slightly different from the real ones. Still, the spectral effect, due to mismatch between the device structure and the incident spectrum can be observed in Figure 45: a maximum efficiency is reached for a certain APE and drops off as light is red or blue shifted, allowing the finding of the APE that maximizes the performance of each cell.

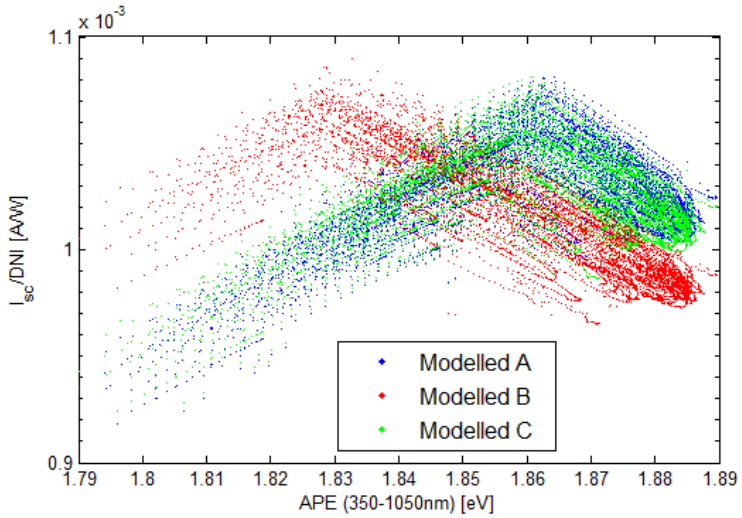

Figure 45 – Modelled I_{sc}/DNI vs APE in the 350-1050nm range throughout the period of evaluation.

Cells A and C reach a maximum around APE=1.86 eV, close to the reference AM1.5d, whereas cells B show higher current generation at APE=1.83 eV, redder spectra than the reference.

3.3.2. Spectral Mismatch Ratio

Figure 46 presents the spectral mismatch ratio as determined using the method described in section 2.4.

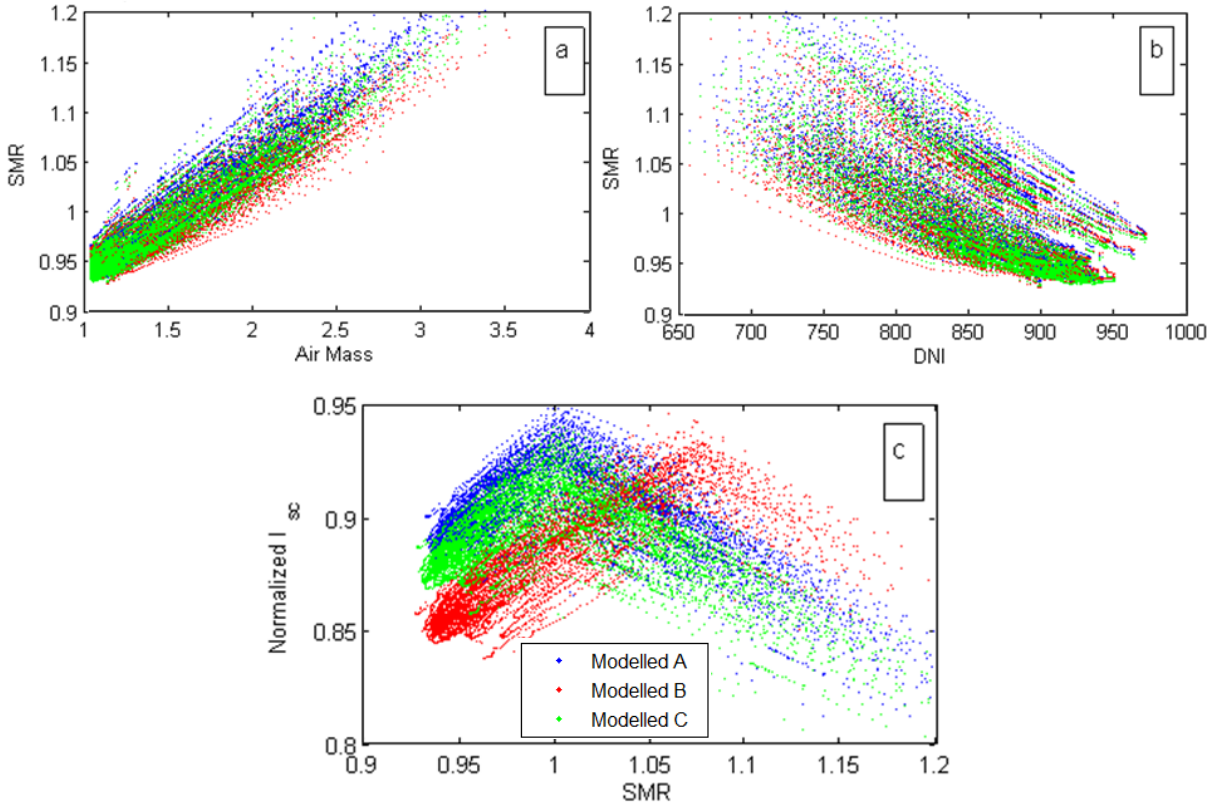

Figure 46 – SMR calculated for clear sky moments in the period of evaluation: a) SMR vs AM, b) SMR vs DNI and c) normalized I_{sc} (1000 W/m^2) vs SMR.

One can observe that the normalized I_{sc} is less than 1, because the normalization to 1000W/m^2, and the DNI outdoors never reaches such value. The SMR at the peak of normalized I_{sc} is 1.005 for cells A and C and 1.075 for cells B. This is coherent with the previous findings, B type cells being matched for a red rich spectrum compared with the reference spectrum and the other two cells matched close to the reference spectrum. Those two cells are current-matched at similar SMR, which corresponds to the similarity of spectral responses; however, A type cell has higher I_{sc} intensity. Moreover, except in winter, cells B seldom met current-matching conditions in comparison to the other two cells, as can be confirmed in Figure 47.

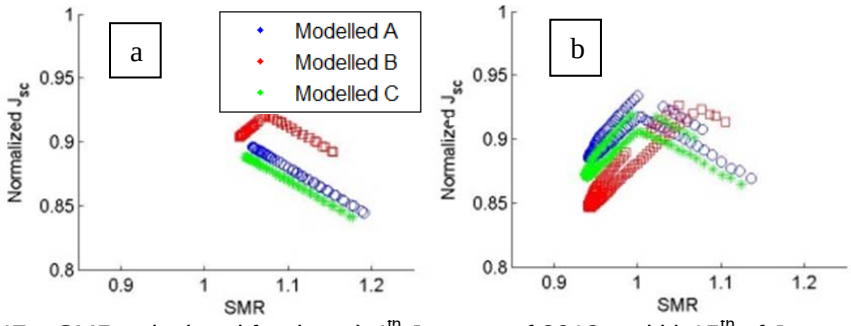

Figure 47 – SMR calculated for the: a) 4th January of 2013 and b) 15th of June of 2013.

For the winter case study, one can see that SMR is always greater than 1 and the only cell operating at optimum spectra (with a local maximum of normalized I_{sc}) is B type. Contrarily, in the study case of summer, cells B are always farther from the spectral conditions that favour current-matching, as the spectra are mostly bluer than the reference.

3.3.3. Z

Computing this parameter in the present assessment comprised some limitations, as no monitor cells were accessible. Thus, to simulate the outcome of the application of the previous method, as modelled spectral irradiance and the spectral response of each cell were available, the I_{sc} of each top and middle sub-cell were calculated to simulate the mentioned monitor cells. Then, in order to avoid incoherence by using simulated monitor cells' I_{sc} to obtain Z and plotting it against the real modules' I_{sc}, the simulated I_{sc} for each cell type (also normalized to 850W/m^2) were plotted instead (Figure 48).
However, contrarily to [14], optical transference functions for the optics were considered in the simulation of Z, therefore avoiding, to a certain extent, the effects of the optics. Still, no temperature effects could be considered.

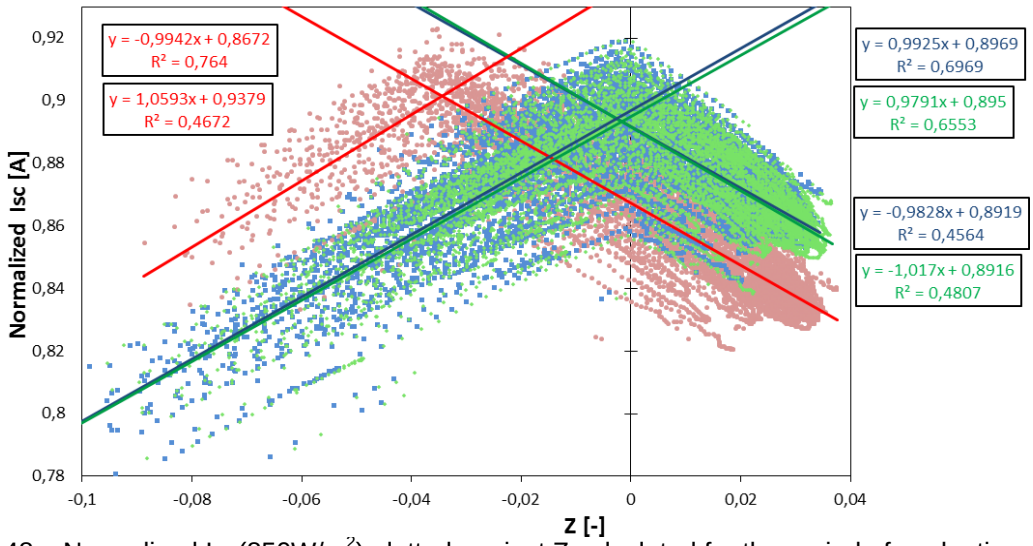

Figure 48 – Normalized I_{sc} (850W/m^2) plotted against Z calculated for the period of evaluation. Linear fits to the left and right of each peak for cells A (blue), B (red) and C (green).

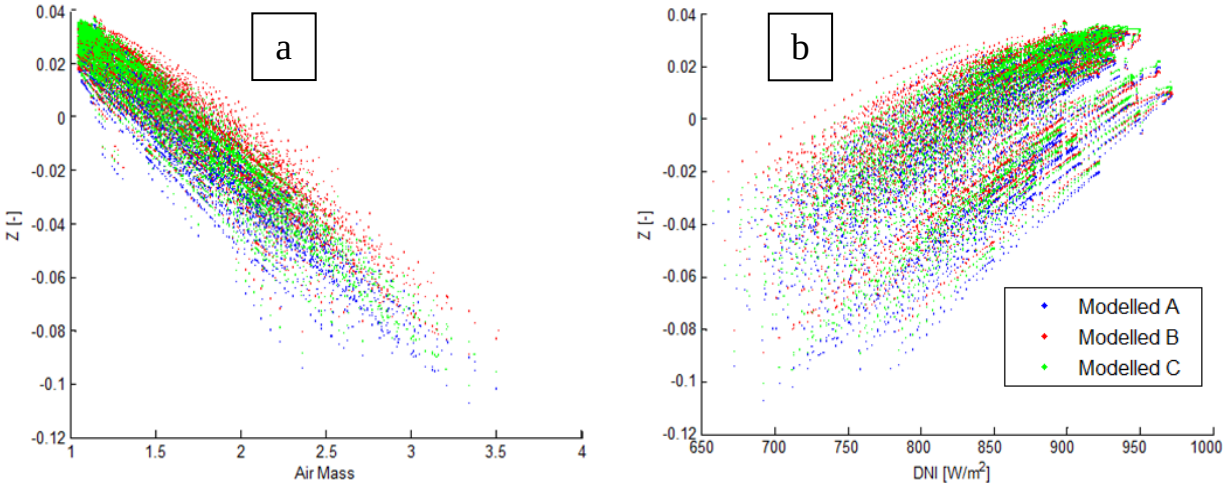

Figure 49 – Z calculated for the evaluated period against: left) AM and right) DNI.

Figure 48 shows a normalized I_{sc} reaching a maximum at Z close to -0.038 for cells B and close to 0 for A and C. It is concluded that under spectral conditions which correspond to such values of Z the respective TJ solar cells operate in the current-matched mode. This seems reasonable, according to the results of the previous indexes and to Figure 49. Therefore, cells A and C are optimized for the AM1.5d reference spectrum and cells B for higher AM or high aerosol content. For Z values higher than the previous, the middle cells are expected to become the limiting sub-cells in the module and for Z values lower than those, the top cells limit the current.

3.3.4. I_{sc}/DNI

Spectral sensitivity in CPV modules is examined by analysing short circuit current, I_{sc}, divided by direct normal irradiance, as spectral parameters change [8]. Fortunately, this parameter can be accessed with measured data, rather than using modelled DNI, providing a more reliable estimate.

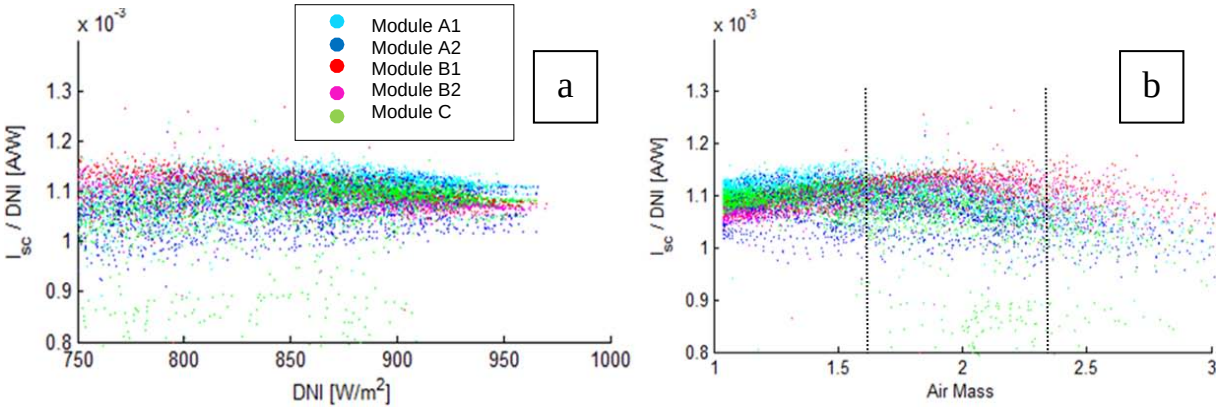

Figure 50 – I_{sc}/DNI calculated throughout the period of evaluation: a) I_{sc}/DNI vs DNI and b) I_{sc}/DNI vs AM, where the dashed line represents AM zone at which I_{sc}/DNI peaks.

This parameter enables the validation of the previous ones. Contrarily to the other cells, as seen before, cells B are more suited to operate under less energetic spectra and higher air masses, since I_{sc}/DNI is greater for these cells at lower DNI and higher AM values than for the other cells. In Figure 50, it can be seen that module with cells C features a drop on its short-circuit current, at certain times, even after the clear sky filter was applied. This issue is addressed in section 3.4.1.

All indexes are quite clear pointing out the spectral conditions that maximize the performance of each of the considered solar cells. Although, depending on the means available, some indexes may be more difficult to access then others. For instance, if detailed knowledge on the spectral irradiance distribution is available, since APE is simple to calculate, statistical analysis of APE may be useful when selecting a TJ cell to use in a certain module technology and location. Values of APE in the same wavelength range as each junction's spectral response may indicate the most adequate set of band-gaps that a multi-junction cell should cover, in order to efficiently use the solar spectrum. On the other hand, I_{sc}/DNI is also an index that can easily provide good insight on the performance of cells, if reliable simulations or long term field data are accessible.
However, and although more demanding since requiring reference indoor calibration, SMR and Z are the indexes that allow direct comparison with a reference spectrum (usually the standard AM1.5d), to which CPV solar cells are often optimized. For a certain location, these indexes provide not only an overview of the spectral irradiance distribution, in terms of how close it is to the reference spectrum, but also point out which cell technology would perform better under any spectrum.
Finally, Z is the most challenging parameter to compute, because monitor cells are seldom accessible, but is still a unique method to estimate I_{sc} values for any spectral distribution, without the need to rely on solar spectrum monitoring.

3.4. CPV Performance Analysis

In this section, only measured values are used to compare the energy yield of each cell, considering all the background discussed above. Following, the results of the power rating procedure will also be discussed.

3.4.1. I-V Curve

As mentioned in 2.5.4, for each module an I-V sweep is traced every 13 minutes. In Figure 51, I-V curves are presented for the study case of the 12th of November of 2012 and the 17th of April of 2013, both around solar noon.

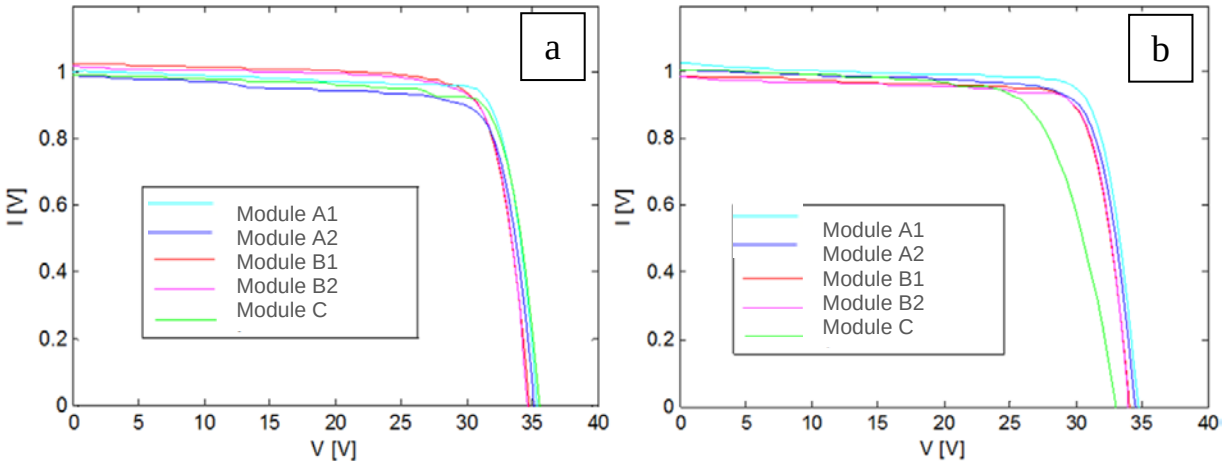

Figure 51 – I-V sweeps for the evaluated modules on the: a) 12th of November of 2012 and b) 17th of April of 2013.

For November, module C has the highest V_{oc} and modules B1 and B2 have the highest I_{sc}, as expected, while their V_{oc} is the lowest. Then, for April, the module A1 has the highest values for those parameters. It should be noticed that, for all modules, the V_{oc} in April is slightly lower than in November, due maybe to the higher ambient temperatures (20ºC for Figure 51,a) and almost 30ºC for Figure 51,b)).

In the April measurement, the module C features a low fill factor and a low V_{oc}. In fact, since the middle of October of 2012 this module reveals a drop in performance, with very low fill factors. If the abnormality was constant, it could be explained by a failure in the module; however, at some random days the parameters get back to normal, just to suffer a break the following day, even in consecutive days with similar weather. When comparing wind speed, ambient temperature and relative humidity for two consecutive clear sky days with differences on those parameters, and with differences on module C performance, no clues were found. Actually, when plotting annual V_{oc} against those parameters (see Figure 52) no conclusions can be taken, besides that V_{oc} decreases approximately 0.075V per 1ºC, ambient temperature.

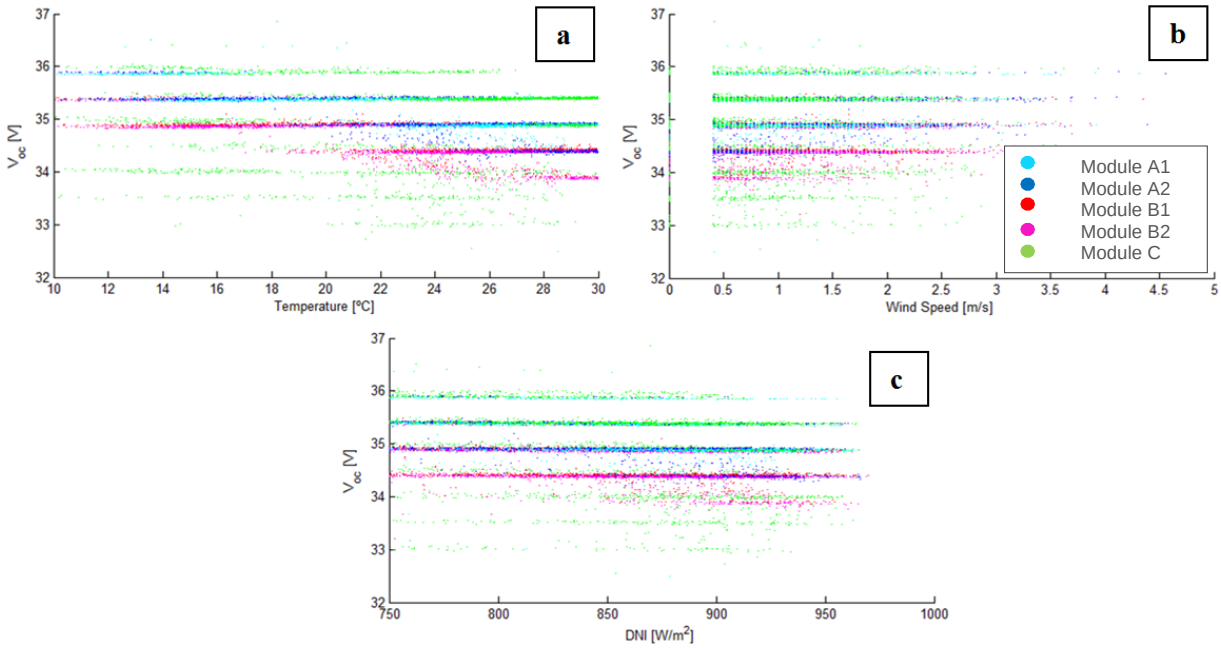

Figure 52 – Measured V_{oc} for the period of evaluation against: a) ambient temperature, b) wind speed and c) DNI.

These results suggest an issue with the thermal link with the heat sink, leading to an occasional abnormal temperature increase. This issue should be accessed in deeper evaluations, since TJ cells are very sensible to temperature, which changes quickly with irradiance, and thus V_{oc}, with temperature coefficients in the order of -4.5mV/ºC/cell [58].
Figure 53 shows the P_{mp}, efficiency and fill factor at MPP during the two representative days. Efficiency was determined using GNI, instead of DNI, and no corrections were applied.

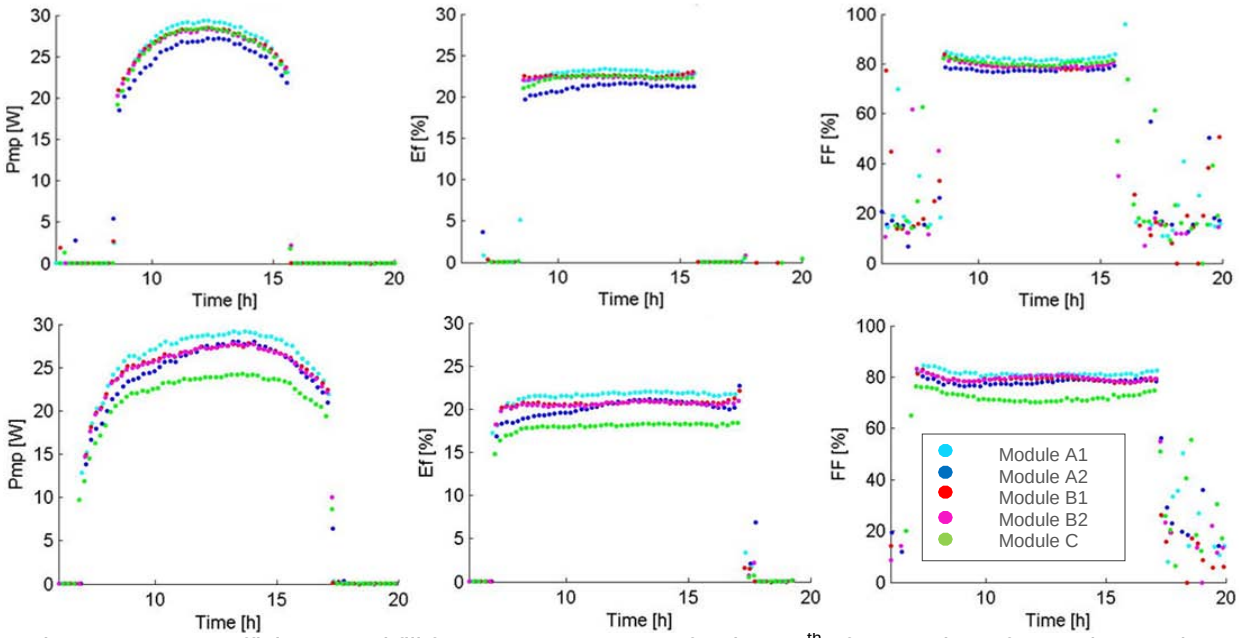

Figure 53 – P_{mp}, efficiency and fill factor measurements for the: 12th of November of 2012 (top row) and 17th April of 2013 (bottom row).

It is interesting to observe that in spite of having the highest I_{sc} in November, modules B1 and B2 do not deliver the highest power, because the A1 module has higher FF. Cells B may be optimized for higher AM and redder spectrum, but perhaps cells A have lower series resistance or their Ge junction is able to maintain greater fill factors or these cells are more resistant to temperature increase. In fact,

the temperature coefficient for these cells is -4.1mV/ºC, whereas for Cells B it is -4.4mV/ºC. Still, the discrepancy shown among modules with cells of the same manufacturer also triggers questions regarding the physical conditions of the module itself. Modules B1 and B2 seem to be very consistent.
On the other hand, in April, the same A1 module still has the highest values. All parameters are very low for the module C. This may be consistent with a loose solar cell, reaching higher temperatures (due to less effective thermal dissipation) and misalignment or soiling (e.g. oxides deposited from increased temperatures).
Overall, for the whole period, the FF is around 80% and module efficiencies around 20% (Figure 54), which is quite reasonable considering that the full potential of the cells is not being tapped. Still, it should be highlighted that when DNI is used efficiencies of about 25% are obtained. If the focused light was concentrated on the entire area of the cell, and not just a 4×4mm square, the I_{sc} would naturally be greater, and so P_{mp}, assuming a perfect tracking of the sun. However, the module performance would be possibly much more sensitive to misalignments and the current loss due to the non-uniform illumination would have a stronger impact; the effect of temperature and series resistance would naturally be also higher.

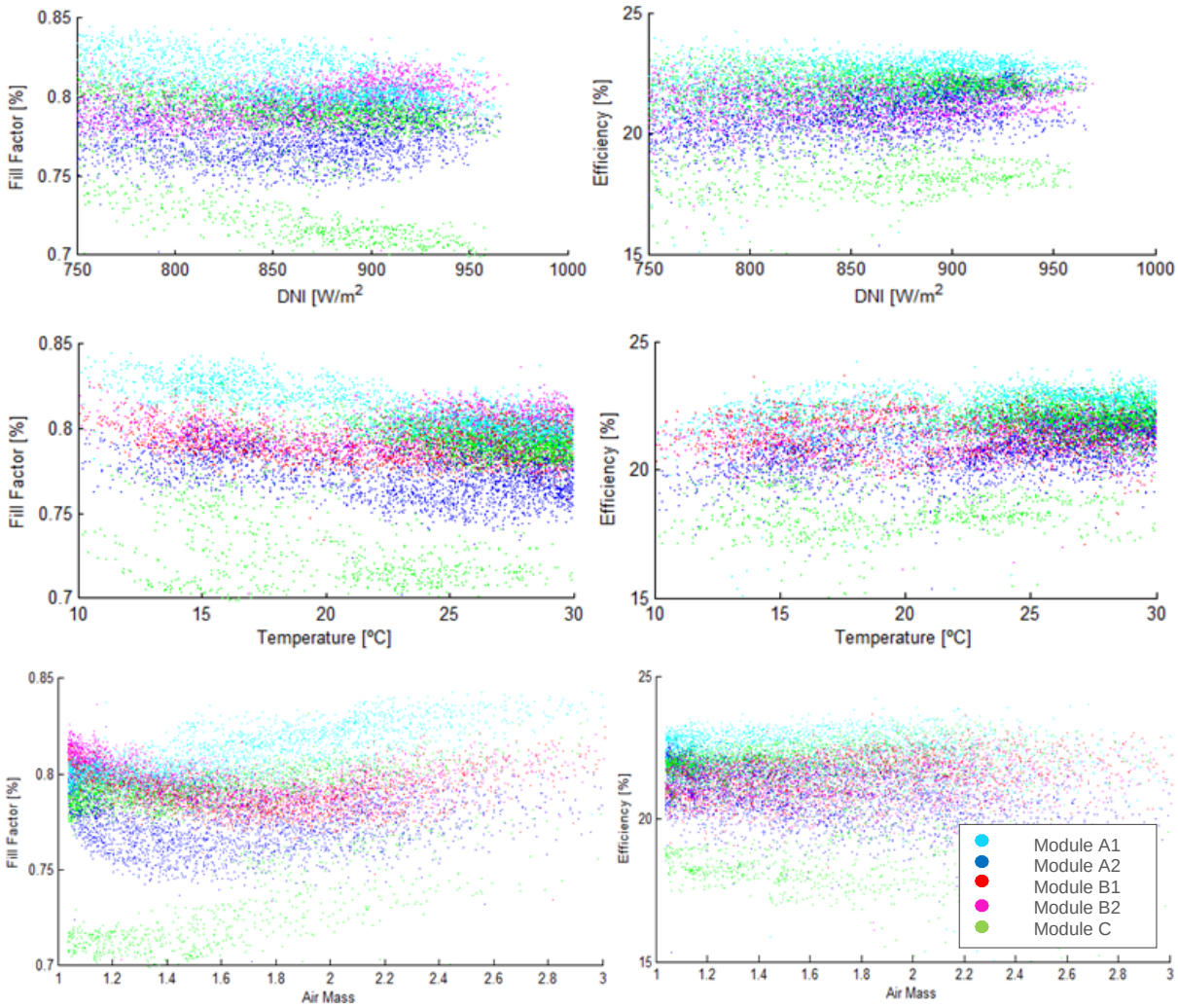

Figure 54 – Module fill factor and efficiencies against DNI, ambient temperature and AM, after clear sky filtering.

One can see that module efficiency is somewhat constant with DNI, air mass or temperature, but the same is not observed for the fill factor. FF reaches a minimum at values around which I_{sc}/DNI (Figure 50) peaks [8] because FF increases with current mismatch [4]. Likewise, it can be stressed that FF behaves inversely to I_{sc}, decreasing as operating conditions become closer to the optimized DNI and AM conditions found previously. However, apparently other factors influence the fill factor to a

similar extent as the spectrum, factors such as the module temperature, CSR, tracking errors or dust and dew on the modules [14].

3.4.2. Energy Yield

The energy yield of the modules can be determined simply through the integration of the power-time curve, from the maximum power delivered by the modules. Figure 55 and Figure 56 present the energy yield for November, January, April and June, as well as the yearly energy yield from July of 2012 to June of 2013, for all modules under study.

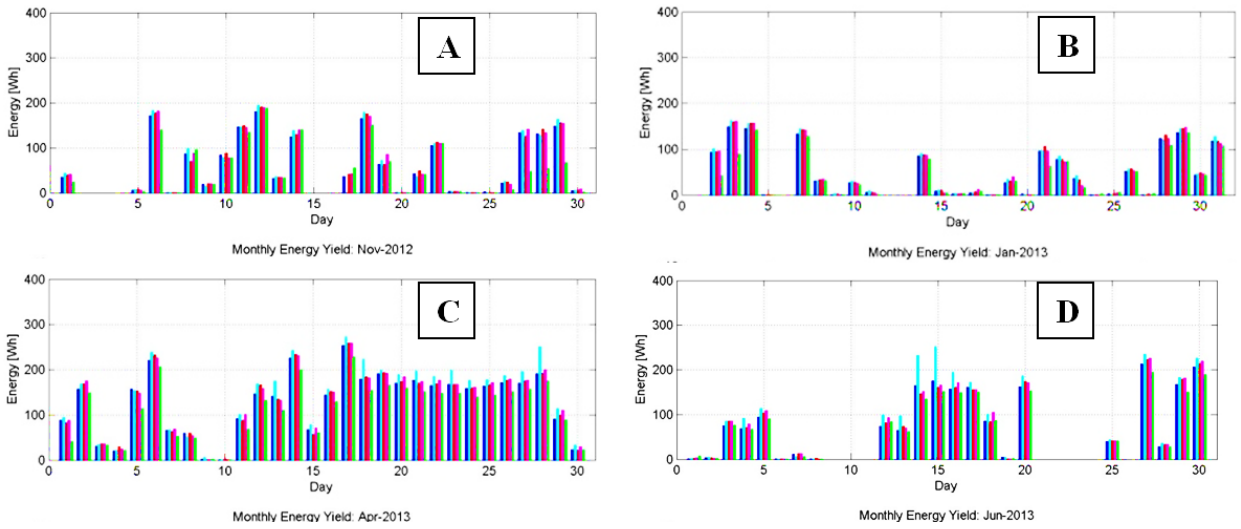

Figure 55 – Daily module energy yield: a) November of 2012, b) January of 2013, c) April of 2013 and d) June of 2013.

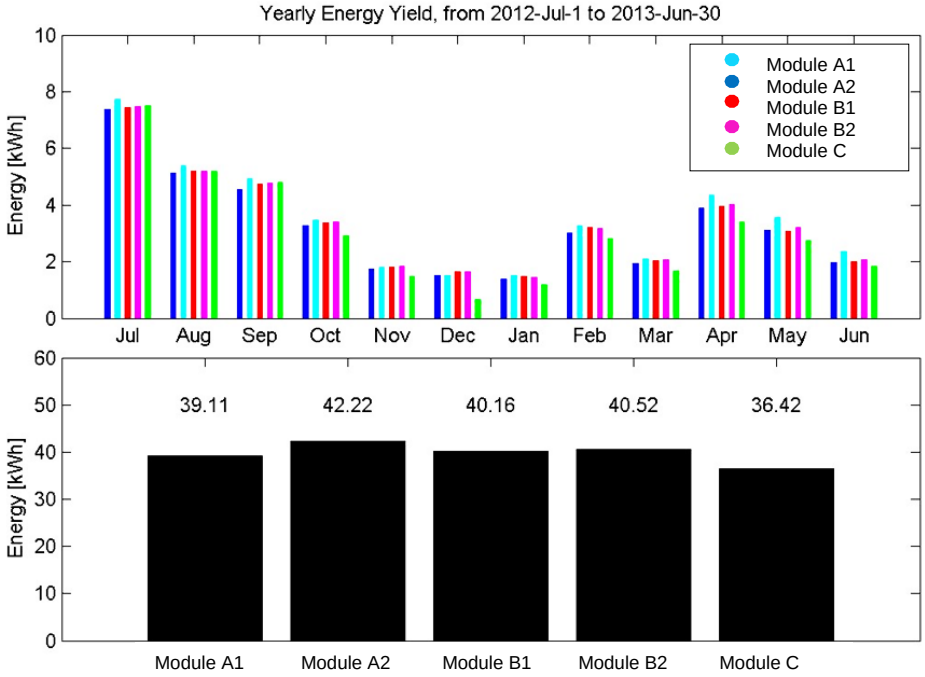

Figure 56 – Monthly (top) and yearly (bottom) module energy yield.

Figure 55 highlights the superior performance of the module A1, mainly during Spring/Summer. Conversely, the module C performance is overall quite low, with sporadic days of good performance. On the other hand, modules B1 and B2 show a performance in between, but very consistent among its different modules.

The total energy yield of each module is shown in Figure 56. The power was off to the site for several days in May and June, which can explain the lower energy yield. Still, relatively to the module which yielded the most, 42kWh by module A1, the energy delivered by module A2 is -7.4%, by module B1 is -4.9%, by module B2 05 is -4.0% and by module C -13.7%.
Therefore, A type cell reveals to be a cell technology well suited for the early stage Circadian Solar modules under evaluation and for the Solar Campus weather and solar spectra. Besides the early stage of the prototypes, great care with the module assembly and solar cells procurement must be taken in advanced stages, in order to avoid variability among modules. Cells B would also perform well and perhaps could overcome A type cells' energy yield if the first and last hours of direct sunlight were not lost in the Solar Campus.

3.4.3. ASTM Power Rating

Monthly power ratings were calculated by applying the clear sky filter mentioned in 2.3 and using Eq.(4), where Wind is $2ms^{-1}$, $T_{ambient}$ is 20ºC and DNI is $900Wm^{-2}$, in order to meet CSOC conditions. In an attempt to filter the abnormal performance of module C until a certain extent, P_{mp} was also selected to $\geq$ 15W (except for December, when P_{mp} of module C was never greater than 15W). An annual overview is presented in Figure 57.

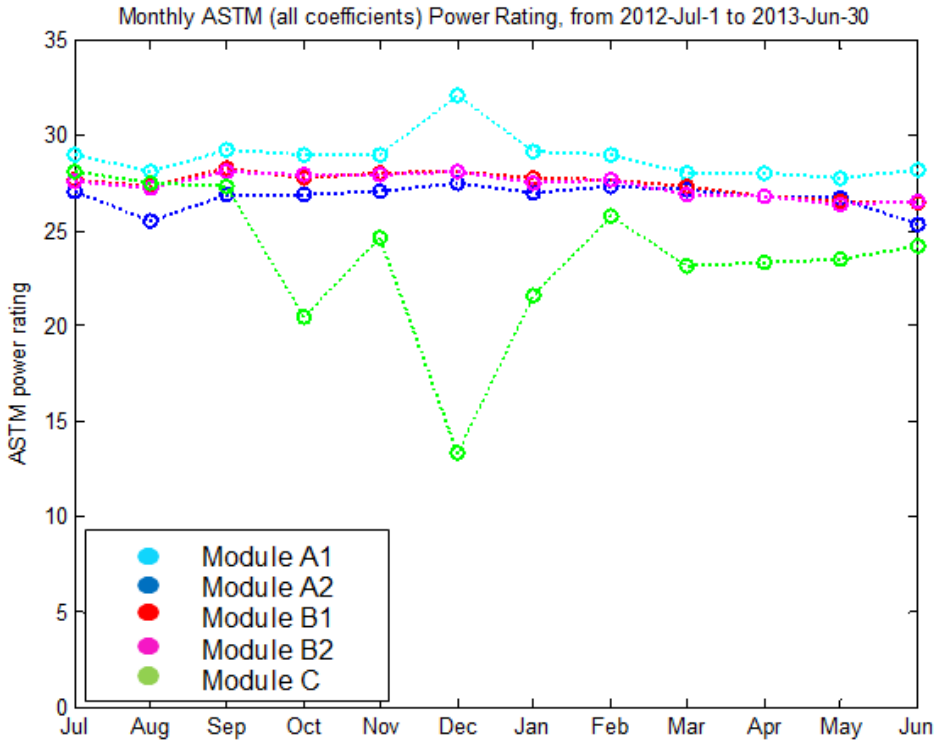

Figure 57 – Monthly ASTM E 2527-06 power rating.

The power rating model takes into consideration the effect of DNI (up to the second order), temperature and wind speed (first order only). Its limitations have been reported for PV flat panels in [61], thus for CPV it is expected that the inaccuracy increases since its power output determination has been shown in this particular case to be very sensitive to these and other parameters.
Furthermore, and considering that the effect of wind speed and ambient temperature do not linearly affect the Circadian modules' output (due to the modules casing and heat sinks for passive cooling) the ASTM power was recalculated using only two terms of DNI. The results are shown in Figure 58.

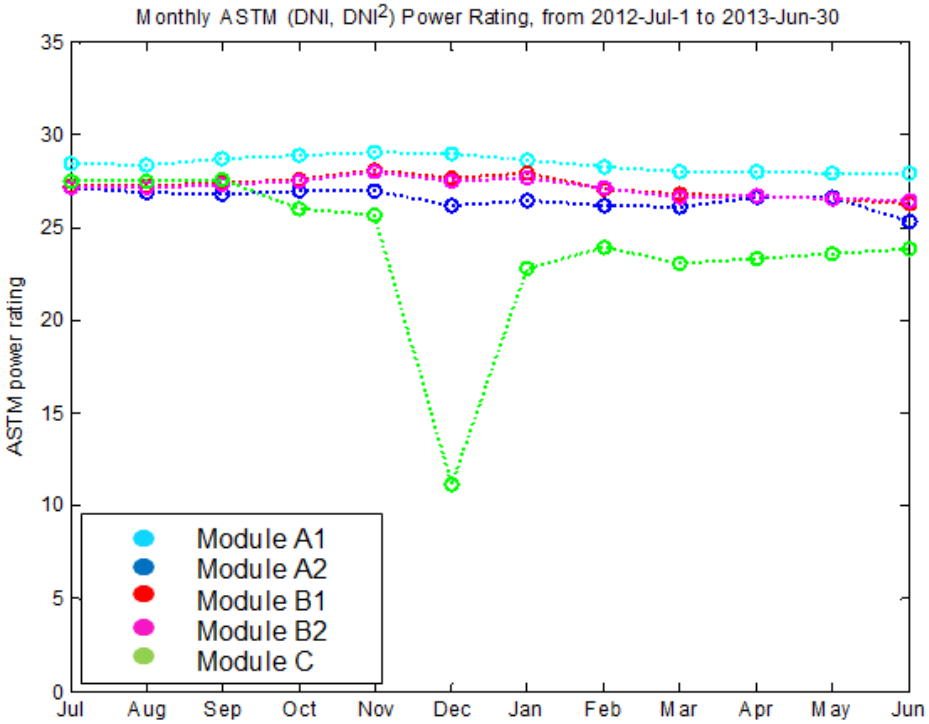

Figure 58 – Monthly power rating using only two terms of DNI.

These recalculated ASTM power rating results show a strong reduction in the variability of the power rating of the module A1. The module C features a slight decrease from October, its collapse in December and partial recovery and stabilization afterwards. The rating at CSOC shows values in accordance to the power often delivered by the modules at 900W/m^2, as can be seen in Figure 59, where the comparison between both methods and how well they are fitted to the P_{mp} measured in clear sky conditions is shown.

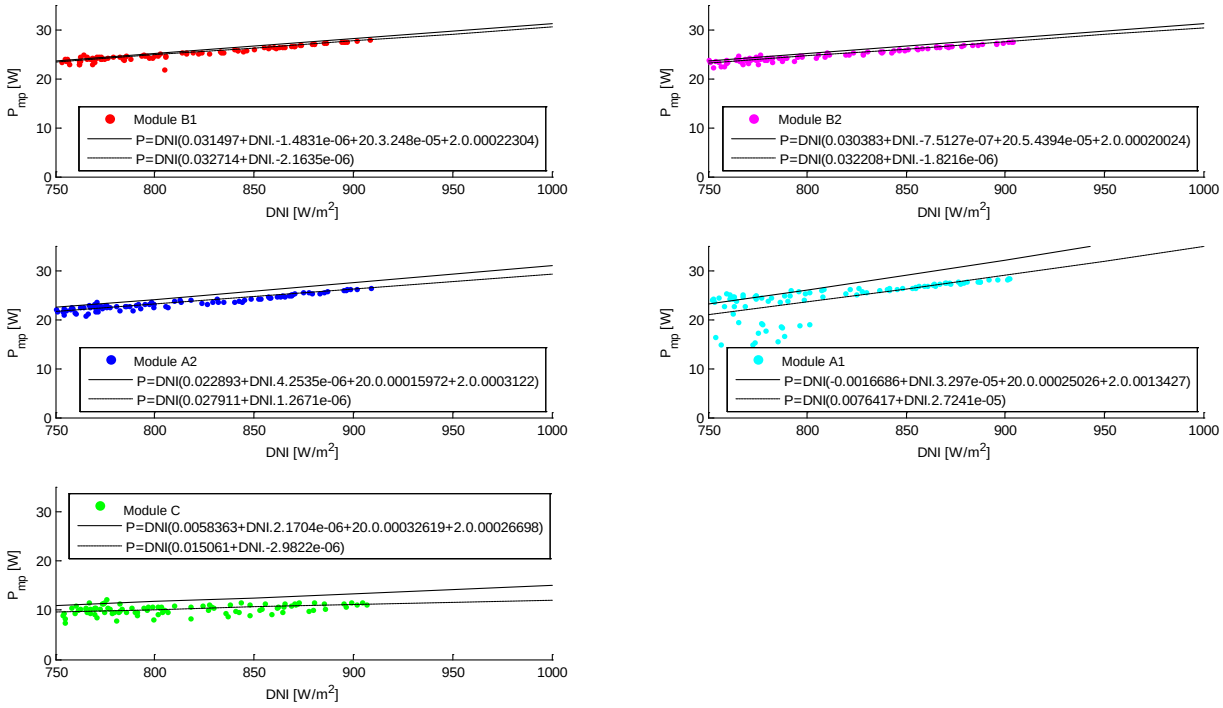

Figure 59 – ASTM power rating for the month of December of 2012 using: four terms of DNI (solid line) and a second-order DNI only regression (dashed line).

One can see that, excepting the noise added by the module C, a strong correlation of power with irradiance terms is obvious, especially for the two terms approach at high DNI values, existing a great deal of noise and virtually zero correlation between power and wind and temperature terms, except for the extremely cold days. Thus, it is confirmed that wind speed and temperature terms are not appropriate at all when there is great variability in module performance and outliers. In the case of the modules here studied, once they are compact and not opened to the exterior, it is not expected that they are exposed to such elements in a way that performance would drop much. Though, the power rating computed with only two terms of DNI is almost independent of the conditions dictated by the norm for $T_{ambient}$ and Wind speed, once either 20ºC or 2ms^{-1} are barely met under real operating conditions, as can be seen in previous graphs and has been target of debate around the IEC 62670 norm.
The average error resulting from both approaches is plotted in Figure 60.

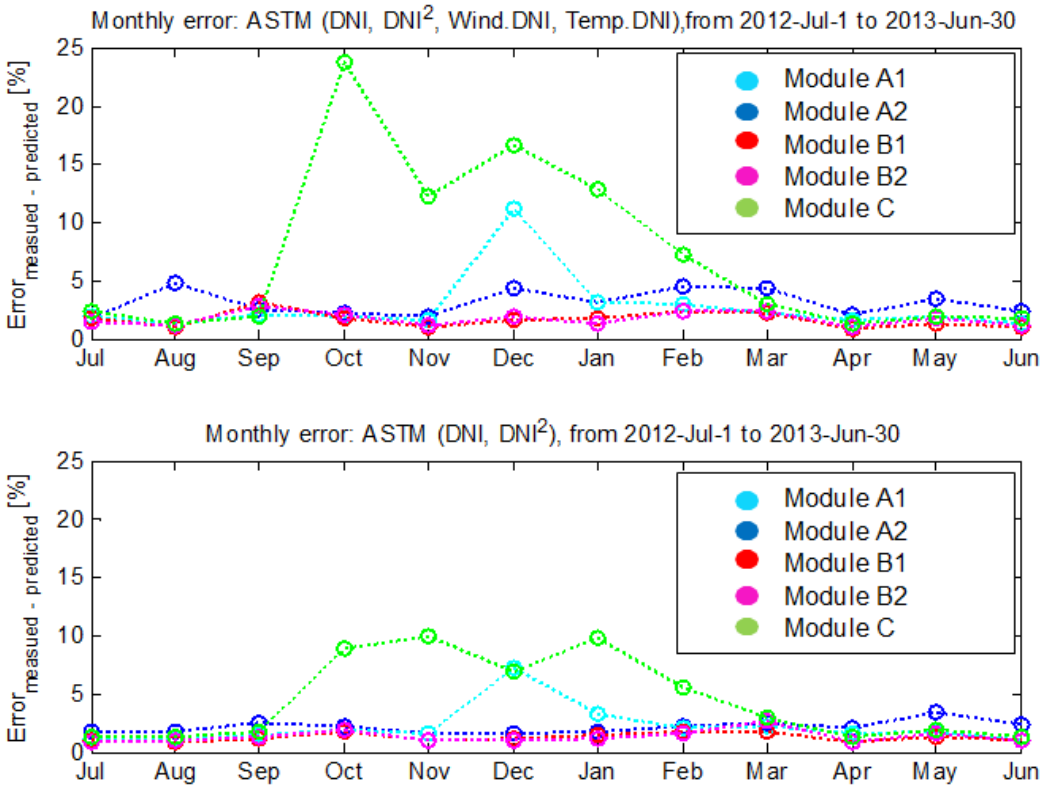

Figure 60 – Average error for every month from July of 2012 to June of 2013.

In spite of the abnormal performance of module C introducing more noise into the method, as expected, when the four terms are taken into account the error is greater and more variable throughout the year, except in summer, when module behaviour seems to be less variable. On the other hand, the small error calculated for the two DNI terms approach would be due to the fact that other terms beyond DNI are being ignored.
Using ASTM-2527 can result in power ratings that vary by 10% for CPV [43] and attempts to adapt the ASTM method by adding terms of AM, GNI, AOD or PW actually increased variation. However, additional filtering proved to slightly improve the results there and several key recommendations should also be added to the clear sky filter, such as either exclude AM >2 and PW <0.5, exclude months that AM 1.5 does not occur or do not ignore temperature effects on lenses. But, for instance, as cells B are more adapted to AM>2, if such recommendations were taken into account, the best of their performance would be excluded. Moreover, the method must also concern cell technology and which parameters have effect on it, in order to adjust a proper clear sky filter to each case.

4. Conclusions

The Circadian research tracker at the Solar Campus at the Faculty of Sciences of the University of Lisbon was used for a case study of comparative assessment of HCPV modules performance. The research platform includes a complete set of instruments for weather and irradiation characterization and a set of fully instrumented identical CPV prototype modules, in an early stage of development, with triple-junction solar cells from different manufacturers.

Experimental results of spectral irradiance were compared with simulated spectra produced by the SMARTS model using local atmospheric data and AOD collected from nearby observation stations. The results were shown to be consistent but feature an excess red component, which was attributed to the optical transference curve of the window and filter of the spectrometer.

Using the validated SMARTS spectral irradiance profiles, the solar cells spectral responses as provided by the manufacturers and the optics transference functions, the modules short circuit current were determined, and compared with measured data. The analysis showed a relevant variability between identical modules with identical solar cells provided by the same manufacturer, which is expected for early stage prototype modules. The modelled results fit the experimental I_{sc} measurements within 10%, a margin smaller than the difference between the measured current of identical modules with cells from the same manufacturer. Experimental results also showed a decrease in model accuracy for higher irradiance, highlighting the limitations of the modelling by not taking into account effects such as the effect of the non-uniformity of the illumination and temperature of the solar cell, eventual soiling or assembly misalignments. These deviations may also be associated to limitations in the SMARTS spectral irradiance due to incomplete description of aerosol concentration.

Power monitoring has shown consistent efficiencies of the order of 20%, depending on the particular solar spectra of the moment, with modules featuring high open circuit voltages and fill factors above 80%. During the period under analysis (from June 2012 to July 2013) Module A1 generated 42kWh, more than 4% than the other prototypes. Again, a relevant variability between modules from the same manufacturer was observed. Module C has underperformed due to a malfunction that became apparent after October 2012.

The analysis of the performance of the module prototypes according to different spectral parameters (APE,SMR, Z) has consistently shown that solar cells from manufacturer B (Modules B1 and B2) are optimized for situations with higher air masses, which occur mainly in winter and the earlier and later hours of summer days. The other solar cells are optimized for the reference AM1.5d spectrum, hence producing more electricity during the summer months.

Power rating according to the ASTM statistical regression method was also determined. Results showed that the effects of wind speed and ambient temperature introduce noise in the analysis and should be disregarded. This may be understood by noticing that the solar cells are encased and therefore less sensitive to wind speed and ambient temperature. Of course, the effect of the ambient temperature is already included indirectly via DNI, with which is strongly correlated to. Average deviations below 10% were determined suggesting that a second-order DNI only regression is the appropriate method for CPV systems power rating.

5. Appendix

Electroluminscence emission of cells B demonstrate the presence of quantum dots in the region of the middle junction, which is mentioned by the manufacturer, and increases radiative recombination on those cells [42]. This is coherent with the findings presented in section 3.3. Very low radiative recombination of the second peak (InGaAs) of cells A compared to other cells indicates the low shunt in middle junction, while the high radiative recombination of the InGaP top junction in A type series indicates the high material quality of the top layer. C type cells have some variability in their EL emission, perhaps due to a process not as well controlled as the other manufacturers or cells coming from different parts of the wafer. However, as far as CPV is concerned, it does not seem coherent to question cell quality, since the maximum quality is always required for such technology, (some of the cell types are even often named on champion cell efficiencies) and, as mentioned in 2.5.4, the I-V curves are checked, so such inconsistencies would be avoided. Possibly, the cells were not in perfect conditions before the EL measurements.

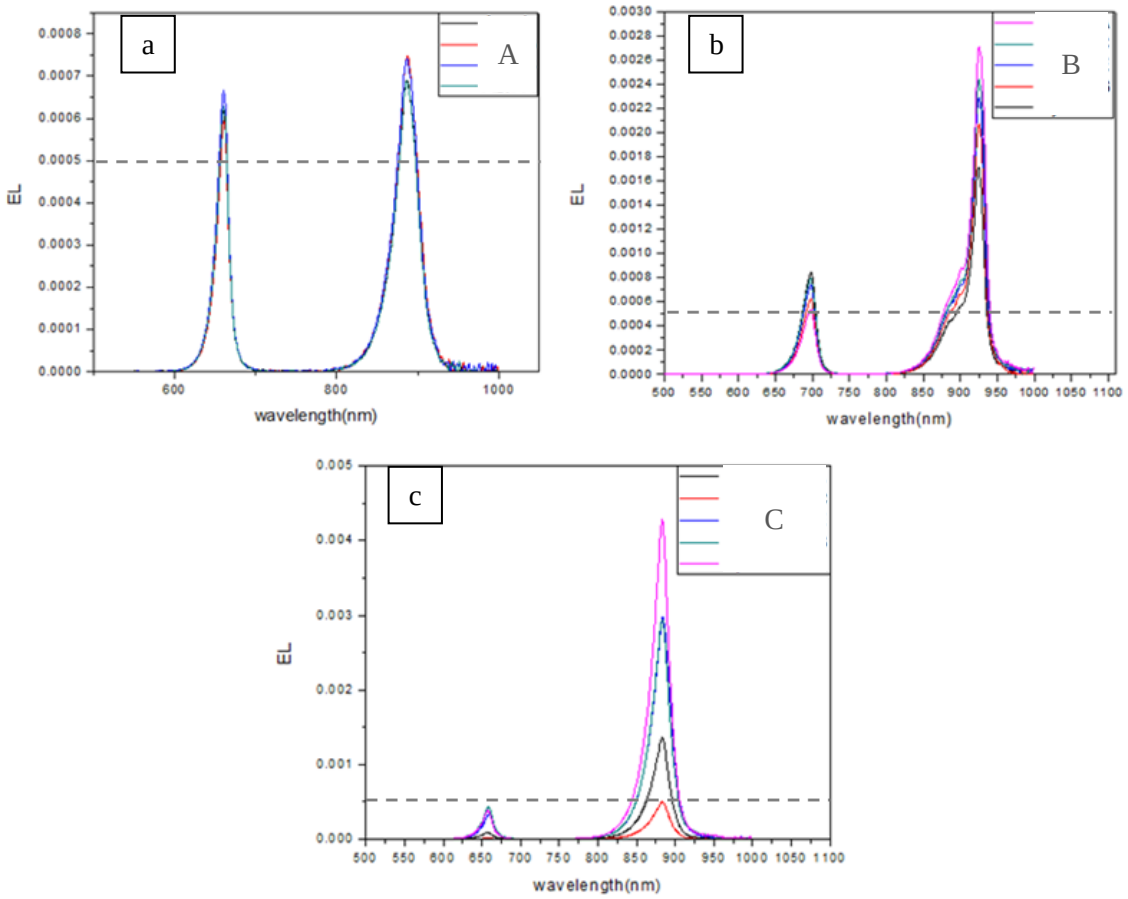

Figure 61 – Electroluminescence measurements for: a) cells A, b) cells B and c) cells C. Grey dashed line represents a scale reference.

On the other hand, these results are not entirely conclusive, unless they had been made under the same concentration factor of the modules, for TJ cell behaviour is no trivial knowledge [10]. Actually, it is clear that the greater the current injection, the more free carriers will be generated, whose lifetimes vary with the level of injection. Thus, the predominant process of recombination is different from low to high concentration and so will be the performance of the III-V solar cells, because they may be dimensioned to work under high levels of concentration and not to low currents.

6. References

[1] M. Wolf, "Limitations and Possibilities for Improvement of Photovoltaic Solar Energy Converters: Part I: Considerations for Earth's Surface Operation," *Proceedings of the IRE*, vol. 48, pp. 1246–1263, 1960.

[2] A. Luque and S. Hegedus, *Handbook of Photovoltaic Science and Engineering*, vol. 36. 2003, p. 1162.

[3] N. Yastrebova, "High-efficiency multi-junction solar cells: Current status and future potential," *Solar Energy*, no. April, 2007.

[4] H. Cotal, C. Fetzer, and J. Boisvert, "III–V multijunction solar cells for concentrating photovoltaics," *Energy Environmental Science*, vol. 2, no. 2, p. 174, 2009.

[5] J. Román, "State-of-the-art of III-V Solar Cell Fabrication Technologies, Device Designs and Applications," *Advanced Photovoltaic Cell Design*, no. Cvd, 2004.

[6] G. F. X. Strobl, T. Bergunde, W. Kostler, R. Kern, M. Meusel, G. Laroche, W. Zimmermann, A. W. Bett, F. Dimroth, W. Geens, S. Taylor, E. Fernandez, L. Gerlach, C. Signorini, and G. Hey, "European Roadmap of Multijunction Solar Cells and Qualification Status," *2006 IEEE 4th World Conference on Photovoltaic Energy Conference*, vol. 2, pp. 1793–1796, 2006.

[7] J. Olson, D. Friedman, and S. Kurtz, "High-efficiency III-V multijunction solar cells," *Handbook of Photovoltaic Science and Engineering*, 2003.

[8] M. Muller, B. Marion, S. Kurtz, and J. Rodriguez, "An investigation into spectral parameters as they impact CPV module performance," *AIP Conference Proceedings*, pp. 1–5, 2010.

[9] S. Kurtz, *CPV 101: Intro to CPV Technology, Opportunities and Challenges*. 2009.

[10] A. Braun and N. Szabó, "Current-limiting behavior in multijunction solar cells," *Applied Physics Letters*, vol. 98, no. 22, p. 223506, 2011.

[11] W. W. Martin A. Green, Keith Emery, Yoshihiro Hishikawa and E. D. D. Dunlop, "Solar cell efficiency tables (version 41)," *Progress in Photovoltaics Research and Applications*, no. version 41, pp. 1–11, 2012.

[12] K. Araki and M. Yamaguchi, "Influences of spectrum change to 3-junction concentrator cells," *Solar Energy Materials*, vol. 75, pp. 707–714, 2003.

[13] P. Faine, S. Kurtz, C. Riordan, and J. Olson, "The influence of spectral solar irradiance variations on the performance of selected single-junction and multijunction solar cells," *Solar cells*, 1991.

[14] G. Peharz, G. Siefer, and a. W. Bett, "A simple method for quantifying spectral impacts on multi-junction solar cells," *Solar Energy*, vol. 83, no. 9, pp. 1588–1598, Sep. 2009.

[15] J. Jaus and C. Gueymard, "Generalized spectral performance evaluation of multijunction solar cells using a multicore, parallelized version of SMARTS," *AIP Conference Proceedings*, vol. 126, pp. 122–126, 2012.

[16] N. Chan, "Impact of individual atmospheric parameters on CPV system power, energy yield and cost of energy," *Progress in Photovoltaics Research and Applications*, 2013.

[17] F. Nagamine, R. Shimokawa, M. Suzuki, and T. Abe, "New solar simulator for multi-junction solar cell measurements," *Conference Record of the Twenty Third IEEE Photovoltaic Specialists Conference 1993 Cat No93CH32839*, 1993.

[18] N. Chan and T. Young, "Validation of energy prediction method for a concentrator photovoltaic module in Toyohashi Japan," *Progress in Photovoltaics Research and Applications*, 2012.

[19] Z. D. Adeyewa and E. E. Balogun, "Wavelength dependence of aerosol optical depth and the fit of the angstrom law," *Theoretical and Applied Climatology*, vol. 74, no. 1–2, pp. 105–122, Jan. 2003.

[20] C. Gueymard, "Progress in direct irradiance modeling and validation," *Proc. ASES Annual Conf. Phoenix, AZ, American Solar Energy Soc.*, 2010.

[21] R. W. Bergstrom, K. S. Schmidt, O. Coddington, P. Pilewskie, H. Guan, J. M. Livingston, J. Redemann, and P. B. Russell, "Aerosol spectral absorption in the Mexico City area: results from airborne measurements during MILAGRO/INTEX B," *Atmospheric Chemistry and Physics*, vol. 10, no. 13, pp. 6333–6343, Jul. 2010.

[22] C. Gueymard, "Daily spectral effects on concentrating PV solar cells as affected by realistic aerosol optical depth and other atmospheric conditions," *SPIE Solar Energy+ Technology*, pp. 741007–741007–14, Aug. 2009.

[23] "Estudo de Incidências Ambientais da Central Fotovoltaica de Alta Concentração de Estoi. Resumo Não Técnico," 2012. [Online]. Available: http://www.ccdr-alg.pt/ccdr/index.php?name=News&file=article&sid=691#.Ui0hBcaIPNY.

[24] "SolarGIS, Maps: Direct Normal Irradiation (DNI)," 2010. [Online]. Available: http://solargis.info/doc/88.

[25] C. Gueymard, "Parameterized transmittance model for direct beam and circumsolar spectral irradiance," *Solar Energy*, vol. 71, no. 5, pp. 325–346, 2001.

[26] C. Gueymard, "SMARTS code, version 2.9. 5," 2005.

[27] N. Geuder, "IRRADIATION MEASUREMENTS ON GROUND: Pre-Feasibility Study for the Establishment of a Pre-Commercial Concentrated Solar Power Plant in Namibia," 2012, no. July.

[28] J. Leloux, D. Pachón, and G. Sala, "Spectral Solar Radiation Measurements and Models for CPV Module Production Estimation," *AIP Conference Proceedings*, pp. 225–228, 2010.

[29] C. A. Gueymard and D. . Myers, "Validation and ranking methodologies for solar radiation models," *Modeling Solar Radiation at the Earth's Surface*, pp. 479–510, 2008.

[30] I. Reda and A. A. Nrel, "Solar Position Algorithm for Solar Radiation Applications (Revised)," *NRELTP56034302*, pp. 1–56, 2003.

[31] B. N. Holben, T. F. Eck, I. Slutsker, D. Tanré, J. P. Buis, A. Setzer, E. Vermote, J. A. Reagan, Y. J. Kaufman, T. Nakajima, F. Lavenu, I. Jankowiak, and A. Smirnov, "AERONET—A Federated Instrument Network and Data Archive for Aerosol Characterization," *Remote Sensing of Environment*, vol. 66, pp. 1–16, 1998.

[32] "Aerosol Robotic Network (AERONET). Data Synergy Tool," 2013. [Online]. Available: http://aeronet.gsfc.nasa.gov/cgi-bin/bamgomas_interactive.

[33] C. Gueymard, "Analysis of monthly average atmospheric precipitable water and turbidity in Canada and Northern United States," *Solar Energy*, vol. 53, no. 1, pp. 57–71, Jul. 1994.

[34] "Agência Portuguesa do Ambiente (APA), QualAr – Base de Dados On-line sobre Qualidade do Ar. Estação de Entrecampos, Lisboa," 2013. [Online]. Available: http://www.qualar.org/INDEX.PHP?page=4&subpage=3&estacao=3072.

[35] C. Gueymard, D. Myers, and K. Emery, "Proposed reference irradiance spectra for solar energy systems testing," *Solar Energy*, vol. 73, no. 6, pp. 443–467, 2002.

[36] C. A. Gueymard, "Magnitude and Variability of Daily Spectral Effects on HCPV and LCPV Solar Cells Under Realistic Conditions," *CPV-8 Conf., Toledo, Spain*, 2012.

[37] J. Pó, "Assessment of the IEC 60891 norm conversion methods under outdoor test conditions," vol. 4, 2011.

[38] "Scripps Institution of Oceanography (SIO), Scripps CO2 Program," 2013. [Online]. Available: http://scrippsco2.ucsd.edu/.

[39] G. Kinsey and K. Edmondson, "Spectral response and energy output of concentrator multijunction solar cells," *Progress in Photovoltaics Research and Applications*, pp. 279–288, 2009.

[40] K. Araki, "What Is the Most Appropriate and Practical Index to Represent Spectrum Sensitivity of CPV?," *AIP Conference Proceedings*, pp. 225–228, 2010.

[41] J. Bowman, S. Jensen, and M. McDonald, "Analysis Of Soiling Rates At The Victor Valley Community College CPV Site," *AIP Conference Proceedings*, 2011.

[42] S. Kurtz, *Opportunities and challenges for development of a mature concentrating photovoltaic power industry*, vol. June, no. November. NREL/TP-520-43208, National Renewable Energy Laboratory (NREL), Golden, CO., 2009, pp. 8–11.

[43] M. Muller, B. Marion, J. Rodriguez, and S. Kurtz, "Minimizing variation in outdoor CPV power ratings," *AIP Conference Proceedings*, vol. 1407, pp. 336–340, 2011.

[44] S. Surendran, "IEC 62670 Update," pp. 1–13, 2012.

[45] J. Jaus, T. Mißbach, S. Philipps, G. Siefer, and A. Bett, "SPECTRAL MEASUREMENTS USING COMPONENT CELLS: EXAMINATIONS ON MEASUREMENT PRECISION," *black-photon.de*, pp. 1–6, 2011.

[46] T. Betts and C. Jardine, "Impact of spectral effects on the electrical parameters of multijunction amorphous silicon cells," *Proceedings of 3rd World Conference on Photovoltaic Energy Conversion 2003*, vol. 2, pp. 1756–1759, 2003.

[47] T. Minemoto, Y. Nakada, H. Takahashi, and H. Takakura, "Uniqueness verification of solar spectrum index of average photon energy for evaluating outdoor performance of photovoltaic modules," *Solar Energy*, vol. 83, no. 8, pp. 1294–1299, Aug. 2009.

[48] C. CORNARO and A. Andreotti, "Solar spectral irradiance measurements relevant to photovoltaic applications," *Proceedings of the Third International Conference on Applied Energy*, 2011.

[49] J. Hashimoto, S. Kurtz, and K. Sakurai, "Performance of CPV system using three types of III-V multi-junction solar cells," *AIP Conference Proceedings*, vol. 1477, pp. 372–375, 2012.

[50] M. Meusel, R. Adelhelm, F. Dimroth, A. W. Bett, and W. Warta, "Spectral mismatch correction and spectrometric characterization of monolithic III-V multi-junction solar cells," *Progress in Photovoltaics Research and Applications*, vol. 10, pp. 243–255, 2002.

[51] "Circadian Solar. CT 35 Tracker Specification," 2013. [Online]. Available: http://www.circadiansolar.com/files/Circadian_Solar_CT35_datasheet.pdf.

[52] D. Myers, "Comparison of Direct Normal Irradiance Derived from Silicon and Thermopile Global Hemispherical Radiation Detectors: Preprint," 2010.

[53] C. A. Gueymard, "Direct Normal Irradiance for CSP/CPV: Modeling Challenges."

[54] N. Geuder, F. Trieb, and C. Schillings, "Comparison of different methods for measuring solar irradiation data," *3rd International Conference on Experiences with Automatic Weather Stations*, 2003.

[55] R. Galleano and W. Zaaiman, "Intercomparison campaign of spectroradiometers for a correct estimation of solar spectral irradiance: results and potential impact on photovoltaic devices calibration," *Progress in Photovoltaics Research and Applications*, 2013.

[56] M. Muller, "Experience with CPV Module Failures at NREL," *nrel.gov*, 2012.

[57] R. Hoffman, D. Buie, D. King, and T. Glesne, "Performance of Emcore Third Generation CPV Modules in the Low Latitude Marine Environment of Hawaii," *AIP Conference Proceedings*, vol. 348, pp. 345–348, 2011.

[58] M. Muller, C. Deline, and B. Marion, "Determining Outdoor CPV Cell Temperature," *AIP Conference Proceedings*, vol. 1407, pp. 331–335, 2011.

[59] L. W. Armines and M. Schroedter-homscheidt, "Report on direct normal irradiance standards," 2013.

[60] T. Cooper, M. Pravettoni, M. Cadruvi, G. Ambrosetti, and A. Steinfeld, "The effect of irradiance mismatch on a semi-dense array of triple-junction concentrator cells," *Solar Energy Materials and Solar Cells*, vol. 116, pp. 238–251, Sep. 2013.

[61] D. Myers, "Evaluation of the Performance of the PVUSA Rating Methodology Applied to DUAL Junction PV Technology," 2009.